

# **Semiconducting Metal Oxide Architectures for Solar Energy Applications**

Thesis submitted to  
the University of Calicut for the award of

**DOCTOR OF PHILOSOPHY IN CHEMISTRY**

**SANJAY GOPAL U**



**DEPARTMENT OF CHEMISTRY  
UNIVERSITY OF CALICUT  
KERALA-673635  
DECEMBER 2016**

## **CERTIFICATE**

The adjudicators of the thesis entitled “**Semiconducting Metal Oxide Architectures for Solar Energy Applications**” submitted by Sanjay Gopal U have not suggested any major changes in the scientific content, results and interpretations. However some typographic errors and mild corrections suggested by one of the examiners are incorporated in the revised thesis.

Calicut University

**Dr. Pradeepan Periyat**

March 2017

## **CERTIFICATE**

This is to certify that the thesis entitled “**Semiconducting Metal Oxide Architectures for Solar Energy Applications**” submitted by Sanjay Gopal U to the University of Calicut for the award for the degree of Doctor of Philosophy in Chemistry, is a result of bonafide research work carried out at the Department of Chemistry, University of Calicut under my guidance and supervision. The contents of the thesis have been checked for plagiarism using the software ‘Urkund’ and similarity index falls under permissible limit. I further certify that the thesis or part has not previously formed the basis for the award of any degree, diploma or associateship of any other universities or institutes.

Calicut University

**Dr. Pradeepan Periyat**

December 2016

## **DECLARATION**

I hereby declare that the matter embodied in the thesis is the result of studies carried out by me at the Department of Chemistry, University of Calicut, under the supervision of Dr. Pradeepan Periyat, Assistant Professor, Department of Chemistry, University of Calicut and the same has not previously formed the basis for the award of any degree or diploma. Whenever the work described or cited is based on the findings of other researchers, due acknowledgement is made in keeping with the general practice of reporting scientific observations.

**Sanjay Gopal U**

## Acknowledgements

*I don't know where to start. For the past few years there have been several people those have been encouraging me for my research career. An acknowledgement in my PhD thesis is just a small gesture and it doesn't truly represent how much I appreciate the influence that many people have in my life.*

*First of all, I would like to acknowledge my deep sense of gratitude to my research supervisor, Dr. Pradeepan Periyat for his valuable guidance, which led to the successful completion of the present thesis. I express my heartfelt thanks to him for his valuable advices, constant encouragement and timely corrections. He is a constant source of ideas, knowledge and encouragement and without him, I could not have achieved as much. I will always remember his efforts.*

*I am thankful to UGC, for the UGC-BSR fellowship and I am happy to acknowledge my research group colleagues Jithesh, Binu, Shahnas and Dinesh.*

*I wish to express my sincere thanks to Dr. Baiju Vijayan (Assistant Professor, Kannur University) and Dr. U. S. Hareesh (Principal Scientist, NIIST) whose expertise I called upon many occasions during this work and for allowing me to use their laboratory facility for my research work. Furthermore, their help in carrying out the DSSC fabrication is greatly remembering here. I would like to thank Mr. Sriman Narayanan Tadka for helping me for the DSSC fabrication I have been carried out in C-MET lab.*

*I would like to thank all my teachers, Prof. K. Muraleedharan (Head, Department of Chemistry), Prof. V. M. Abdul Mujeeb (former Head, Department of Chemistry), Professor Aravindakshan, Professor Purushothaman, Prof. Abraham Joseph, Prof. Raveendran, Dr. yahya Ismail, Dr. Renuka, Dr. Ramesan and all the non-teaching staff of the Department of Chemistry.*

*I am thankful to Prof. Suresh Pillai (Institute of Technology, Sligo, Ireland) for his valuable help for characterizations. I also thank Dr. Brijesh, Dr. Damodaran Santhanagopalan and Mr. Sarath (AIMS, Kochi) for the XPS facility. It is my great pleasure to thank Dr. Sindhu, Department of Nanotechnology for PL spectral analysis and Dr. Manoj Lazar for the SEM and DSSC characterization during his research tenure at Monash University.*

*I owe my sincere thanks to Dr. Shaijumon (Assistant Professor, IISER, Thiruvananthapuram) and his research student Binson for the collaborative studies on battery applications have been carried out, although not the complete version the work is presented in the thesis.*

*To my friends and companions in the lab and university; you were all with me in my ups and downs of my PhD career and you've made the whole experience far more enjoyable. I'll miss our tea breaks and chats. My PhD work is over but I'm sure that our friendship will continue for many years. I also extend my gratitude to my lab mates for the thought provoking discussions and funs. I am very much thankful to Divya and Shijina (Department of Physics) for spending their valuable time for recording the XRD of my samples.*

*To my family members, especially to my younger brother Sunay and younger sister Sruthi, It's great to have a PhD but it's better to have you two with me.*

*To my wife Aiswarya, you are a major part of my life. I couldn't write this acknowledgement without mentioning you.*

*To my achan (father) and amma (mother), without you I would have never completed my PhD. You truly are wonderful parents and I will forever be grateful for everything you've done for me throughout my life. This thesis is for both of you!*

*I acknowledge the almighty of god for the good things happened to me during my PhD life.*

**Sanjay Gopal U**

*To*

*My Achan & Amma*

*Science helps us to prove facts,  
but intuition guides us to  
discoveries.*

*-Paulo Coelho*

# CONTENTS

Chapter	Title	Page No.
	Abstract	I-III
1	Introduction	1-45
2	Materials and Methods	46-60
3	Microwave Approach towards Oxygen Rich and Oxygen Deficient Black TiO <sub>2</sub> Nanomaterials for Solar Photocatalysis	61-79
4	One Pot Gel Combustion Synthesis of Black TiO <sub>2-x</sub> and its Application in Solar Photocatalysis	80-94
5	Solution Processed, Oxygen Deficient ZnO Microrods for Solar Photocatalysis	95-117
6	Microwave Power Induced TiO <sub>2</sub> Nanostructures for Efficient Dye Sensitized Solar Cells	118-132
7	Sol-gel Derived ZnO Nanoribbons as Photoanode Material in Dye Sensitized Solar Cell	133-150
8	Overall Conclusions and Future Outlook	151-155
	Publications by the Author	i-iv

# Abstract

---

Semiconducting micro/nano metal oxides of TiO<sub>2</sub> and ZnO have been synthesized by various strategies such as microwave, gel combustion, solution processing and sol-gel method. These materials have been investigated in the area of photocatalysis and/or dye sensitized solar cells (DSSC).

In the first approach, a green and rapid sol-microwave strategy was designed for the syntheses of ‘yellow oxygen rich’ (YAT-150) and ‘black oxygen vacancy rich’ (BAT-150) anatase TiO<sub>2</sub> nanoparticles. YAT-150 was synthesized using only titanium (IV) butoxide and water as only precursors. The *in situ* precursor modification by Mn (II) acetate switched anatase TiO<sub>2</sub> from YAT-150 to BAT-150. The entry of Mn<sup>2+</sup> into the crystal lattice of anatase TiO<sub>2</sub> paved the way for peak texturing in the existing peak orientations along with the origin of new anatase TiO<sub>2</sub> peaks. Furthermore, the ultra-small (~5 nm) yellow and black anatase TiO<sub>2</sub> nanoparticles were found two fold and four fold more photoactive than the commercially available photocatalyst Degussa-P25 under sunlight illumination (Ref: S. G. Ullattil and P. Periyat, *Nanoscale*, 2015, **7**, 19184).

In the second approach a novel and facile one pot gel combustion strategy has been carried out for the synthesis of black TiO<sub>2</sub> with enormous defect states. Limited variety of reactants such as titanium butoxide, diethylene glycol and water were used for the synthesis. This

swiftly formed nanoplateform was occupied with a high concentration of surface defect sites, especially  $\text{Ti}^{3+}$  and oxygen vacancy sites in excess. The in (lattice) and out (surface) defect states were confirmed by Raman, XPS and TEM analysis. These defect-enriched features enabled 33% more photocatalytic activity for BAT than the commercially available photocatalyst Degussa-P25 under solar illumination (Ref: S. G. Ullattil and P. Periyat, *J. Mater. Chem. A*, 2016, **4**, 5854).

The next motive was the synthesis of ZnO nanocrystals with rod morphology and investigating its photocatalytic activity. A series of ZnO photocatalysts with oxygen vacancy richness have been achieved by solution processing method followed by calcination at various temperatures 300, 500, 700, 800, and 900 °C. All the ZnO nanocrystals possessed defective structures with copious surface oxygen vacancies directed toward notable visible light absorption around  $\lambda = 480$  nm (band gap = 3.05–3.09 eV). The photocatalytic efficiencies of all ZnO samples were systematically examined under sunlight and UV illumination using methylene blue (MB) as a model system. ZnO calcined at 500 and 700 °C demonstrated microrod morphology with band gap energies of 3.08 and 3.09 eV respectively have shown the highest solar photocatalytic activity revealed the synergistic effect between oxygen vacancy and the rod morphology. ZnO calcined at 500 °C, having maximum surface oxygen vacancy sites degraded MB within 10 min whereas the commercial photocatalyst Degussa-P25 has taken 20 min under solar illumination (Ref: S. G. Ullattil, P. Periyat, B. Naufal and M. A. Lazar, *Ind. Eng. Chem. Res.*, 2016, **55**, 6413).

The fourth strategy was designed to synthesize randomly oriented TiO<sub>2</sub> for DSSC as a photoanode material which can more efficiently carry current to improve the efficiency of DSSC by minimizing the vacant spacing in between the particles. TiO<sub>2</sub> nanostructures have been synthesized using 300 and 600 W and those were appeared as spherical aggregates with average particle size of 10 nm. These anatase TiO<sub>2</sub> nanoparticles were successfully employed as the working electrode for DSSC and a systematic investigation of the performance of DSSC constructed with standard N719 dye with conventional iodide/triiodide (I<sup>-</sup>/I<sub>3</sub><sup>-</sup>) has demonstrated a higher efficiency of 6.6 % (S. G. Ullattil and P. Periyat, *Sol. Energy*, 2017, **147**, 99).

In the fifth approach, by using a facile sol-gel method, ZnO nanoribbons with an average particle size of 25 nm has been synthesized and were implemented as photoanode material in DSSC. The film thickness and dyeing time have been kept as variables to analyze the performance of DSSC constructed with standard N719 dye with conventional iodide/triiodide (I<sup>-</sup>/I<sub>3</sub><sup>-</sup>) electrolyte. It has been found that the optimum film thickness and dyeing time were 16 μm and 2 h respectively for obtaining an efficiency of 2.2 % with a very high fill factor ~73 % (Ref: P. Periyat and S. G. Ullattil, *Mater. Sci. Semicond. Process.*, 2015, **31**, 139).

# 1 Chapter

## Introduction

### Contents

1. 1. The Solar Energy
  1. 2. Semiconducting Metal Oxides as Solar Energy Harvesters
  1. 3. Synthetic Methods for Semiconducting Metal Oxides
  1. 4. Environmental Hazards
  1. 5. Solar Cells
  1. 6. Objectives of the Thesis
  1. 7. Overview of the Experimental Work
- References

### 1. 1. The Solar Energy

It is rapidly decreasing the supply of conventional oil and other fossil fuels, yet most of our energy demand continues to be met by fossil fuels. The world cannot forever continue to depend on these non-renewable fuels, so that there is an urgency to find an alternative reliable energy source. Thus the present scenario demands maximum utilization of the renewable energy sources such as sunlight, wind, biomass, rain, tides and waves. Among these renewable sources, sunlight is the most important one because it is available plenty without any cost and holds the position, the universal energy source. The importance of solar energy has already been stated in 1911 by the Russian-German chemist Wilhem Ostwald that “mankind should cover a maximum part of its energy demand from solar energy.”<sup>1</sup> In the

contemporary society it has been found that semiconducting metal oxides with tunable band gap are the most efficient materials for harvesting solar energy.

## **1. 2. Semiconducting Metal Oxides as Solar Energy Harvesters**

The mean global energy consumption rate was 13 TW in the year 2000 due to increasing population and energy consumption more than usual.<sup>2</sup> It is expected reasonably that global energy demand will be 28 TW in 2050.<sup>2</sup> Scientists all over the world are indulged in the discovery of new pathways that could easily harvest sunlight to meet the present and future energy demands. One such method to utilize solar energy is the use of semiconducting nanoarchitectures, in environmental and energy systems.<sup>3</sup> In this manner, photocatalysis, in an environmental perspective and solar cell, in an energy perspective are very crucial for the future, since they could eliminate all the energy and environmental problems to facilitate an environmentally benign society. Photovoltaic technologies or solar cells have been identified as being capable of overcoming the over reliance on fossil fuels for energy demand.

Different metal oxides such as titanium dioxide ( $\text{TiO}_2$ ), zinc oxide ( $\text{ZnO}$ ), cerium dioxide ( $\text{CeO}_2$ ), niobium oxide ( $\text{Nb}_2\text{O}_5$ ), manganese dioxide ( $\text{MnO}_2$ ) and bismuth oxide ( $\text{Bi}_2\text{O}_3$ ) have been employed in photocatalytic and photovoltaic technologies. Among these  $\text{TiO}_2$  and  $\text{ZnO}$  are the most efficient materials due to their similarities with an ideal light harvester.

### 1. 2. 1. Titanium Dioxide (TiO<sub>2</sub>)

TiO<sub>2</sub> is the most investigated light harvesting materials around the world owing to its high chemical stability, wide band gap energy, high surface area, easy and economically feasible production *etc.*<sup>4</sup> TiO<sub>2</sub> has mainly three different polymorphs such as anatase, rutile and brookite. In all the three forms, titanium (Ti<sup>4+</sup>) atoms are coordinated to six oxygen (O<sup>2-</sup>) atoms, forming TiO<sub>6</sub> octahedra. The three crystal structures differ by the distortion of each octahedra and by the assembly patterns of the octahedral chains. Anatase can be regarded to be built-up from octahedra, those are connected by their vertices (corners), in rutile, the edges are connected, and in brookite, both vertices (corners) and edges are connected. The structure of all the three forms are shown in **Figure 1. 1**. Among the three forms, rutile is thermodynamically most stable whereas anatase is the kinetically most stable form of TiO<sub>2</sub>.<sup>5</sup> Other general attractive properties of TiO<sub>2</sub> include 1) Low cost synthesis and easy tailoring of TiO<sub>2</sub> 2) Easier modification of the surface structure. Rutile TiO<sub>2</sub> has a band gap of 3.02 eV whereas anatase TiO<sub>2</sub> has a value of 3.20 eV. Hence the tailored TiO<sub>2</sub> in general used as a light harvesting material for different application such as photocatalysis and photovoltaics. For *e.g.* mesoporous nanocrystalline TiO<sub>2</sub> semiconductor films are the most widely studied photoanode material in a special type of solar cell known as dye sensitized solar cell (DSSC)<sup>6,7,8,9</sup> due to that its conduction band energy level lies just below the excited state level of the photosensitizer dye so that an efficient electron transfer process between the excited dye and conduction band (CB) of TiO<sub>2</sub> can take

place.<sup>10</sup> Hence  $\text{TiO}_2$  is very close to being an ideal light harvester, although the drawback is that it does not absorb visible light.

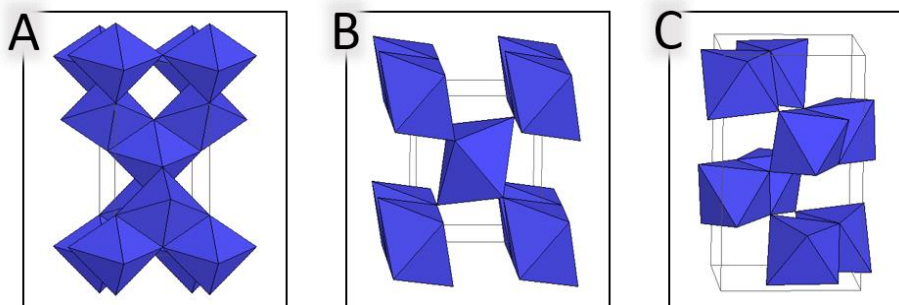


**Figure 1. 1. Anatase (A), rutile (B) and brookite (C) polymorphs of  $\text{TiO}_2$ .**

### **1. 2. 2. Molding $\text{TiO}_2$ as a Complete Solar Harvester**

The sunlight normally contains 5% UV (200-400 nm), 43% visible light (400-700 nm) and 52% of IR (700-2500 nm) energy.<sup>11</sup> The band gap energy of pure  $\text{TiO}_2$  lies in between 3.0 - 3.2 eV, hence the absorption of pure  $\text{TiO}_2$  in its crystalline form is limited in the UV region. Therefore researchers have adopted doping on  $\text{TiO}_2$  for the improvement of its wavelength absorption from UV to visible region. Metal doping was implemented in the early times but due to the formation of secondary impurities (e.g.  $\text{Al}_2\text{TiO}_5$ ,  $\text{CeTi}_4\text{O}_{24}$  and  $\text{Ce}_2\text{Ti}_2\text{O}_7$ ) its crystallinity has been diminished, which subsequently reduced the catalytic efficiency of the material, in particular the photocatalytic activity.<sup>12</sup> After the step back of metal doping, non-metal doping was came into act for better light absorption and it was found that the longer wavelength absorbing light harvesting materials have been successfully synthesized without forming any impurity phases. However, the absorption coverage of non-metal doped  $\text{TiO}_2$

structures was not capable of absorbing IR energy which is 52% of the solar spectrum.<sup>13</sup> To harvest sunlight more effectively, blue,<sup>14,15</sup> yellow,<sup>16,17</sup> brown,<sup>18,19</sup> red<sup>20,21</sup> and grey<sup>22,23,24</sup> TiO<sub>2</sub> have also been reported. However they all persisted limited or even zero absorption in the IR region.

### **1. 2. 3. Origin of ‘Black TiO<sub>2</sub>’**

Since a black material only can effectively absorb energy from the infrared region of the solar spectrum, Chen *et al.* implemented a high pressure hydrogenation strategy on the most investigated material, TiO<sub>2</sub> for achieving wide area absorption, *viz.* for the utilization of IR energy from the sun.<sup>25</sup> After the entry of black TiO<sub>2</sub> nanoparticles into the world of material science, it has been found impetus for energy applications and is found a hot area particularly in the current environmental science.<sup>26</sup> TiO<sub>2</sub> nanomaterials are highly attractive as photocatalysts due to its good chemical stability, non-toxicity, ecofriendly nature and high unambiguous energy conversion efficiencies. Whilst it has been widely applied as photocatalyst, there is a little work on ‘black TiO<sub>2</sub> used as photocatalyst’. To date, several methods such as H<sub>2</sub>-Ar treatment,<sup>27</sup> H<sub>2</sub>-N<sub>2</sub> treatment,<sup>28</sup> electrochemical anodization,<sup>29</sup> Al reduction<sup>30</sup> and NaBH<sub>4</sub> reduction<sup>31</sup> have been implemented for the manipulation of black TiO<sub>2</sub>.

### **1. 2. 4. Zinc Oxide (ZnO)**

Although TiO<sub>2</sub> is universally considered as the most important photocatalyst, ZnO is also a suitable alternative due to their similar band gap energy (3.37 eV), a much higher electron mobility than

exhibited by TiO<sub>2</sub> and its lower cost.<sup>32</sup> Moreover, in certain case, larger quantum efficiency and higher photocatalytic activity than TiO<sub>2</sub> have been reported.<sup>33</sup> ZnO has three crystal structures namely wurtzite, zinc blende and rocksalt. Under normal conditions, wurtzite structure is the most stable. The rocksalt structures may be fabricated at high pressure and the zinc blende structure can only be synthesized on cubic substrates. In addition to these, the crystal structure of ZnO possess numerous point defects generally present, mainly from oxygen vacancies and higher production of hydroxyl ions. The photocatalytic activity of ZnO can be further enhanced by calcinations at high temperatures. ZnO can be prepared by a variety of synthetic strategies include sol-gel,<sup>34</sup> hydrothermal,<sup>35</sup> solvothermal,<sup>36</sup> chemical vapor deposition,<sup>37</sup> physical vapor deposition<sup>38</sup> and microwave methods.<sup>39</sup> These ZnO nanoparticles that have been synthesized provided the impetus for majority of scientific and technological applications such as in nanosensors,<sup>40</sup> nanogenerators<sup>41</sup> and piezoelectronics.<sup>42</sup> Zinc oxide (ZnO) has recently been identified as a promising material as photoanode in DSSCs.<sup>43</sup> The attractive properties of ZnO include 1) bandgap similar that of TiO<sub>2</sub> at 3.2 eV 2) a much higher electron mobility than exhibited by TiO<sub>2</sub> 3) simpler tailoring of the ZnO nanostructure as compared to TiO<sub>2</sub> and 4) easier modification of the surface structure.<sup>44,45</sup>

### **1. 3. Synthetic Methods for Semiconducting Metal Oxides**

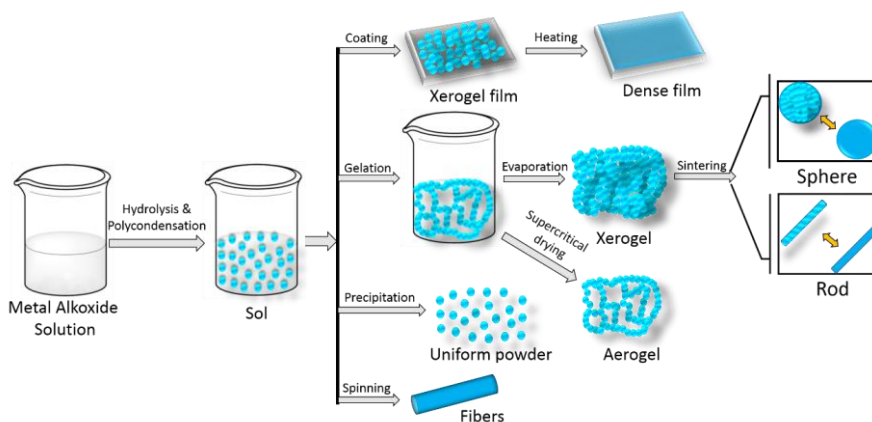
For the synthesis of semiconductors, especially metal oxides, several strategies like sol-gel,<sup>46</sup> gel-combustion,<sup>47</sup> microwave,<sup>48</sup> solution processing,<sup>49</sup> hydrothermal,<sup>50</sup> solvothermal,<sup>51</sup> electrospinning,<sup>52</sup>

chemical vapor deposition,<sup>53</sup> physical vapor deposition<sup>54</sup> *etc.* have been used till date. In the present research scenario three methods *viz.* sol-gel, microwave and gel-combustion strategies have been employed.

### **1. 3. 1. Sol-Gel Method**

Sol-gel process is a versatile solution method for making ceramic glass materials.<sup>55</sup> In general, the sol-gel process involves the transition of a system from a liquid ‘sol’ which is mostly in colloidal form converted into solid ‘gel’ phase. By using this process, it is possible to fabricate wide variety of ceramic or glass materials in the form of ultra-fine powders, thin film coating, ceramic fibres, microporous inorganic membranes, monolithic ceramics and glasses or extremely porous aerogel materials.<sup>56</sup>

The starting materials used in the preparation of the ‘sol’ are usually metal organic compounds such as metal alkoxide/inorganic metal salts. In a series of hydrolysis and polymerization reaction form a colloidal suspension or a sol. Further processing of the sols enables one to make ceramic materials in different forms. When the sol is cast into a mold, a wet ‘gel’ will form. With further drying and heat treatment, the gel is converted into dense ceramic materials. If the liquid in a wet gel is removed under a supercritical condition, a highly porous and extremely low-density material called aerogel is obtained.<sup>57</sup> As the viscosity of a sol is adjusted into a proper viscosity range, ceramic fibres can be drawn from the sol.<sup>58</sup> Ultrafine and uniform ceramic powders are formed by precipitation,<sup>59</sup> spray hydrolysis,<sup>60</sup> or emulsion techniques.<sup>61</sup> The details of the sol-gel processing are shown in **Scheme 1. 1.**



**Scheme 1. 1. Schematic representation of sol-gel processing.**

### 1. 3. 2. Microwave Technique

Microwave method is considered to be an important technique for the synthesis of nanomaterials because 1) the reaction can be done at low temperature 2) no further heat treatment is required for sample production 3) rapid processing 4) improved physical and mechanical properties and 5) negligible environmental hazards.<sup>48</sup> Structural and morphological properties of  $\text{TiO}_2$  can also be tuned by the same strategy by varying microwave irradiation time,<sup>62</sup> power<sup>62</sup> and temperature.<sup>62</sup> By using this technique different structures have been designed by researchers and those have been employed in different areas, especially in photocatalysis and in dye sensitized solar cells.

### 1. 3. 3. Gel-Combustion Method

Gel combustion is a widely used method coming under a broad synthetic area, the combustion synthesis. In combustion synthesis, the exothermic nature of the redox reaction is used to produce desired

materials. Depending upon the nature of reactants: elements or compounds (solid, liquid or gas) and the exothermic nature, the combustion synthesis can be described as self-propagating high temperature synthesis, low-temperature combustion synthesis, solution combustion synthesis, gel-combustion, sol-gel combustion, emulsion combustion, volume combustion (thermal explosion) *etc.* The main advantage of combustion synthesis are<sup>63</sup> the use of relatively simple equipment, formation of high-purity products, stabilization of metastable phases and formation of virtually any size and shape products. In addition to these, the gel combustion synthesis result in highly reactive, compositionally homogeneous and less agglomerated powders of the desired material.<sup>63,64</sup>

#### **1. 4. Environmental Hazards**

Day by day increase of contaminants such as dyes and other organic chemicals produced by industries are highly harmful to the environment. These contaminants present in water can cause considerable problems to microorganisms, aquatic environment, sand, air and thereby health hazards to human being. Therefore decontamination of dyes present in industrial waste water has found impetus in assuring the eco health and for the conservation of the same, several remediation techniques have been proposed. Adsorption or coagulation, involving transfer of pollutants from one phase to another is one of the early employed method.<sup>65</sup> The conventional treatments such as sedimentation, filtration, chemical and membrane technologies were also used but involved high costs and could introduce more contaminates into the environment.<sup>66</sup> Chlorination is

one of the most widely used method, but it generates mutagenic or carcinogenic species that could adversely affect the human body.<sup>67</sup> To minimize these limitations, advanced oxidation processes (AOP) have got supreme importance towards effective decontamination.<sup>68</sup>

#### **1. 4. 1. Advanced Oxidation Process (AOP)**

AOP includes the in-situ generation of highly reactive transient species for mineralization of dye contaminants from wastewater, water pathogens and disinfection of by-products.<sup>68</sup> Because of the ability to completely decompose the target pollutants, heterogeneous photocatalysis is the favorite among environmental chemists to eliminate contamination.<sup>69</sup> The application of illuminated semiconductors for the remediation of contaminants has been used successfully for a wide variety of compound such as alkanes, aliphatic alcohols, aliphatic carboxylic acids, aromatic carboxylic acids, alkenes, phenols, dyes, simple aromatics, halogenated alkanes and alkenes, surfactants, and pesticides.<sup>70</sup>

The photochemistry of semiconductor surfaces has received cracking importance to address the problem of chemical utilization of solar energy. In 1972, after the photocatalytic water splitting reported by Fujishima and Honda, the idea had spurred researchers to take on the challenge.<sup>71</sup> The homogeneous and heterogeneous photocatalytic research are concerned with the splitting of water into hydrogen and oxygen, the “holy grail” of photochemistry. In 1874, this process has been already predicted by Jules Verne in his book “The Mysterious Island”: “Yes, my friends, I believe that water will one day be

employed as fuel, that hydrogen and oxygen which constitute it will furnish an inexhaustible source of heat and light. Water will be the coal of the future.’<sup>72</sup>

#### **1. 4. 1. 1. Photocatalysis**

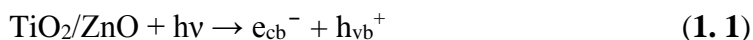
Photocatalysis is generally referred to as ‘the process in which the acceleration of a reaction occurs when a material, usually a semiconductor, interacts with light of sufficient energy (or of a certain wavelength) to produce reactive oxidizing species (ROS) which can lead to the photocatalytic transformation of pollutants.’<sup>73</sup> At least, two events must occur simultaneously during photocatalysis in order to produce the reactive oxidizing species. Typically, the first involves the oxidation of dissociatively adsorbed H<sub>2</sub>O by photogenerated holes and the second involves the reduction of an electron acceptor (generally the dissolved oxygen or oxygen vacancies) by photo-excited electrons. These reactions lead to the production of a hydroxyl and superoxide radical (OH<sup>•</sup> and O<sub>2</sub><sup>-•</sup>) respectively.<sup>73</sup>

#### **1. 4. 1. 2. Semiconductor Photocatalytic Mechanism**

An ideal photocatalytic process leads to the complete mineralization of organic pollutants into carbon dioxide (CO<sub>2</sub>), water (H<sub>2</sub>O) and mineral acids in presence of a semiconductor photocatalyst (usually TiO<sub>2</sub> or ZnO) and reactive oxygen species such as oxygen and/or air.<sup>74</sup>

The photocatalytic reactions are initiated when a photocatalyst (TiO<sub>2</sub> or ZnO) absorbs photons with energy greater than that of its band gap energy during light illumination. Consequently, an electron is

photoexcited from valence band (VB) to the conduction band (CB) of the photocatalyst. This reaction leads to the formation of hole ( $h_{vb}^+$ ) at the VB and an excess electron ( $e_{cb}^-$ ) at the CB as shown in **equation 1. 1**, facilitating an electron-hole separation which is necessary for efficient photocatalysis.



To prevent electron-hole recombination, the CB electron ( $e_{cb}^-$ ) reduces oxygen present in the form of dissolved oxygen or air to form super oxide radical (**equation 1. 2**).



Additional reaction of super oxide radical anion ( $\text{O}_2^{\cdot -}$ ) with holes at the valence band ( $h_{vb}^+$ ) produces singlet oxygen ( $^1\text{O}_2$ ) as shown in **equation 1.3**.<sup>75</sup>



The VB holes reacts with hydroxyl ion ( $\text{OH}^-$ ) to form hydroxyl radical ( $\text{OH}^\cdot$ ) and the hydroxyl radical is a non-selective, extremely strong oxidizing agent which leads to the decomposition of organic, inorganic and biological pollutants (**equation 1. 4** and **1. 5**). Since the valence band holes are strong oxidizing agents, the direct oxidation of organic matter to reactive intermediates are also permitted as shown in **equation 1. 6**.





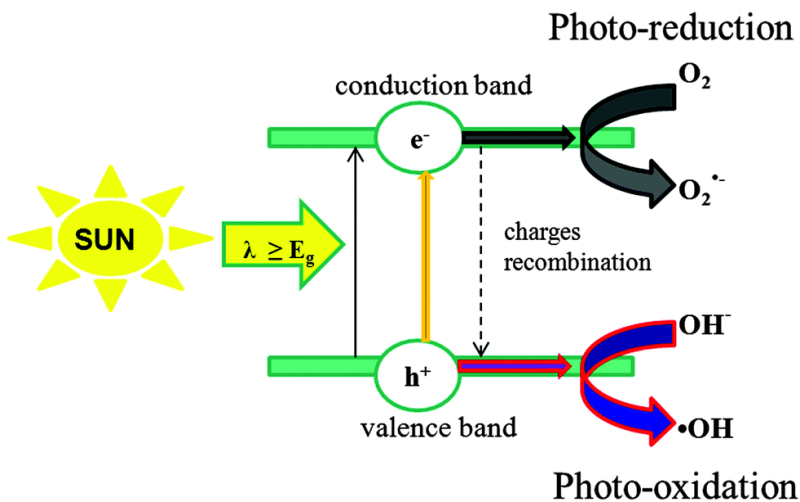
Another reactive oxidizing species, the super oxide radical anion also react with the pollutant to form protonated superoxide radicals ( $\text{HOO}^\cdot$ ) as shown in **equation 1.7**.



The formation of  $\text{H}_2\text{O}_2$  as a result of the coupling of two  $\text{HOO}^\cdot$  has also been reported.<sup>76</sup> Further reaction of  $\text{H}_2\text{O}_2$  with  $\text{OH}^\cdot$  results in the formation of protonated superoxide radicals ( $\text{HOO}^\cdot$ ) again (**equation 1.8** and **1.9**). This  $\text{HOO}^\cdot$  can also function as electron scavenger to trap the conduction band electrons that can delay the electron-hole recombination.<sup>74</sup>



A schematic representation of photocatalysis is shown in **Scheme 1.2**.



**Scheme 1.2. Schematic representation of photocatalysis.**<sup>77</sup>

### 1. 4. 2. Photocatalytic Materials

A wide variety of photocatalysts such as  $\text{TiO}_2$ ,<sup>78</sup>  $\text{ZnO}$ ,<sup>79</sup>  $\text{CeO}_2$ ,<sup>80</sup>  $\text{SnO}_2$ ,<sup>81</sup>  $\text{Nb}_2\text{O}_5$ ,<sup>82</sup>  $\text{BaTiO}_3$ <sup>83</sup> and  $\text{SrTiO}_3$ <sup>84</sup> have been employed for the photooxidation, photoreduction and photodegradation of organic and inorganic compounds. An ideal semiconductor photocatalyst should be<sup>85</sup>

1. Chemically and biologically inert
2. Photocatalytically stable
3. Easy to produce and to use
4. Efficiently activated by sunlight
5. Able to efficiently catalyze reactions
6. Inexpensive
7. Implemented without risks for the environment or humans.

In order to proceed a photocatalytic reaction faster, it is necessary to avoid electron accumulation on the particles. Such accumulation would increase the recombination rate and lower the quantum yield. Thus, the electrons must be removed rapidly by an electron scavenger in the solution. Since, molecular oxygen is available at little or no cost as dissolved in solution or in air, it is the usual electron acceptor.<sup>86</sup> Molecular oxygen plays an important role in photocatalysis, particularly in photodegradation. It can either impede or support the reaction depending on the photocatalytic mechanism. The primary role for oxygen in the photodegradation process is to act as an electron sink for photogenerated carriers. However, it reacts only slowly with the electrons of most of the semiconductors. Because of the relatively low

solubility of oxygen and its weak adsorption at the semiconductor surfaces in contact with aqueous electrolytes, it is almost not possible for an electron to avoid recombination. It has been shown that in semiconductors, oxygen vacancies act as electron traps.<sup>87</sup> The formation of oxygen vacancies or other electron-trapping structural defects is much easier at the surface than in the bulk. Furthermore, when these traps are close enough to the surface, the trapped electrons can react with oxygen.<sup>87</sup>

### **1. 5. Solar Cells**

Solar cell or photovoltaic cell is an electrical device that converts light energy directly into electrical energy by photovoltaic effect.<sup>88</sup> The first photovoltaic effect was noticed by a French physicist Edmond Becquerel. In 1839, at age of 19, he built the world's first photovoltaic cell in his father's laboratory.<sup>89</sup> He found that the electrodes coated with AgBr, AgCl, Ag or Pt with UV had given the best results.<sup>89</sup> 50 years later, the first true solar cell was fabricated by Fritts, using selenium coated transparent layer of gold, which had 1% efficiency.<sup>90</sup> In 1927 copper and copper oxide solar cells were discovered with less than 1% efficiency and later Ohl improved the solar cell efficiency up to 6% in 1941.<sup>91</sup> In the late 1980's efficiency greater than 20% had been achieved using GaAs.<sup>92,93</sup> However the use of expensive materials and fabrication procedures had driven it away from an easily achievable energy system in terms of cost effectiveness and human efforts.

### **1. 5. 1. Three Generations of Solar Cells<sup>94</sup>**

Solar cells are usually divided into three main generations. The first generation solar cells are based on silicon, those are relatively expensive to produce due to the dependence on the availability of crystalline Si with large price. The second generation solar cells are based on thin film technologies, where amorphous and polycrystalline silicon materials are included. Although the production cost of the thin film solar cells was minimized, the efficiency was low as compared to first generation solar cells.<sup>94</sup> Both the first and second generation solar cells are based on single junction devices. The calculated thermodynamic efficiency limits is called Shockley-Queisser limit which can be overcome by the use of third generation solar cell devices. The third generation devices are based on nanocomposites and the goal of the third generation is to produce cheap solar cell with very high efficiency. Thus dye sensitized solar cells (DSSCs) can be considered as a third generation solar cells. Therefore the use of these free standing and flexible solar cells such as DSSCs could help to reduce power supply costs especially to remote areas and that can lead towards the development of countries like India.

### **1. 5. 2. Dye Sensitized Solar Cell (DSSC)**

Dye-sensitized solar cell (DSSC) is a semiconductor photovoltaic device that directly converts solar radiation into electric current.<sup>95</sup> The heart of the system is a wide band gap oxide semiconductor which is placed in contact with a redox electrolyte. TiO<sub>2</sub> (anatase) is the most widely used, although ZnO is a suitable alternative due to its wide

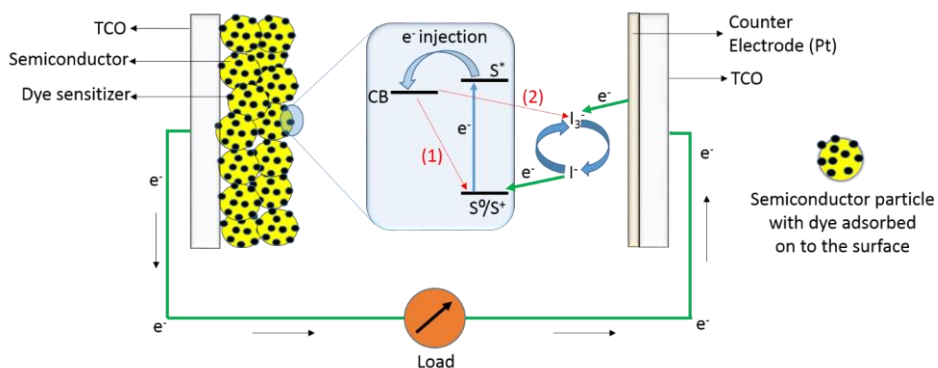
band gap energy. To the surface of any of these nanocrystalline films, a monolayer of the charge transfer dye is attached. When exposed to sunlight the photoexcitation of the dye sensitizer leading to the injection of electrons to the conduction band of the metal oxide film. The electrons thus generated gets diffuse to the anode and are utilized at the external load before being collected by the electrolyte at the cathodic surface (Pt counter electrode) to complete the cycle.<sup>96</sup>

### **1. 5. 3. Components of a Dye Sensitized Solar Cell (DSSC)<sup>97</sup>**

A Dye Sensitized Solar Cell (DSSC) normally contains five components, *viz.*

1. A mechanical support coated with Transparent Conductive Oxides, TCO [generally indium tin oxide (ITO) or fluorinated tin oxide (FTO)].
2. The semiconductor film, usually TiO<sub>2</sub> or ZnO to activate electronic conduction.
3. A dye sensitizer (normally a Ru complex) covalently bound to the surface of the semiconductor to enhance light absorption.
4. An electrolyte containing a redox mediator to carry out regeneration of the dye sensitizer.
5. A counter electrode (typically a glass sheet coated with platinum) capable of electron collection and thereby regenerating the redox mediator.

A schematic representation of the dye-sensitized solar cell is shown in **Scheme 1. 3.**



**Scheme 1. 3. Schematic illustration of a DSSC. Unfavorable recombination reactions (1) semiconductor/dye recombination and (2) semiconductor/electrolytic recombination are also shown in red line.**

#### **1. 5. 4. Reactions involved in a DSSC<sup>94,98,99,100</sup>**

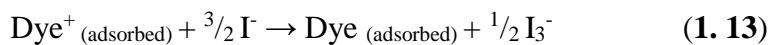
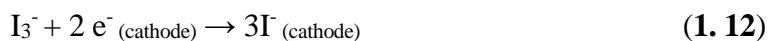
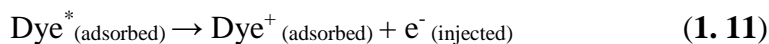
1. Photo-excitation of the dye molecule results in the injection of an electron into the conduction band of the semiconducting metal oxide. The ultrafast injection from the excited Ru-complex into the conduction band of semiconducting metal oxide is one of the most baffling findings in DSSC research. It is generally accepted that a fast femtosecond component is observed for the sensitizer directly attached to a metal oxide surface.
2. The subsequent restoration of the original state of the dye is achieved by the electron donor,  $I^-$  from the electrolyte, where an organic solvent containing redox system, such as the iodide/triiodide ( $I^-/I_3^-$ ) couple is present. The regeneration of

the dye sensitizer by iodide, intercepts the recapture of the conduction band electron by the oxidized dye.

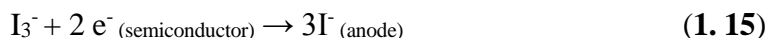
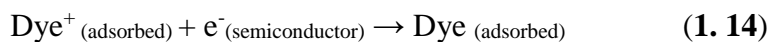
3. Through the nanocrystalline film of metal oxide the electron transport occurs. These films are viewed as an ensemble of individual particles through which the electrons percolation occurs by hopping of electrons from a single particle to another.
4. Depending on the electron density in the semiconductor metal oxide, the back electron transfer from the conduction band of the semiconductor to the oxidized sensitizer occurs on a microsecond to millisecond time scale.
5. The recombination may occur by the hopping of electron from the semiconductor to the acceptor present in the electrolytic system. This process is normally referred to as electron life time and which is very long (1-20 ms) under one sunlight intensity which is far greater than other electrolyte systems that have been used.
6. The iodide is regenerated in turn by the reduction of triiodide at the counter-electrode (usually, platinum electrode) the circuit being completed *via* electron migration through the external load.

The voltage generated under solar illumination corresponds to the difference between the Fermi level of the electron in the solid and the redox potential of the electrolyte. Overall the device generates electric power from light without suffering any permanent chemical transformation.

Reactions involved in a DSSC are shown in **equations 1. 10 - 1. 13**.



Some undesirable reactions occurring in DSSC that leads to the decrease in cell efficiency are depicted in **equations 1.14** and **1.15**.



### 1.5.5. Photoanode Materials

The photoanode material is the key component of DSSCs which plays important roles in dye loading, electron injection, transportation and collection, and therefore exhibits significant influence on the photocurrent, photovoltage and the power conversion efficiency. The size, structure and morphology of photoanode materials have been found significant influence on the photovoltaic performance of DSSCs. Tremendous efforts have been devoted to the design of the chemical composition, structure and morphology of the semiconductor photoanode.<sup>101</sup> Different material structures, including zero dimensional (0D), one dimensional (1D), two dimensional (2D), three dimensional (3D) nanoparticles and hierarchical nanoarchitectures have been developed for the improved solar to electrical energy conversion. Among the different photoanodes those have been used till

date, TiO<sub>2</sub> and ZnO are the unequivocally established candidate for dye sensitized solar cells (DSSC).

### **1. 5. 6. The Dye Sensitizer**<sup>94,102,103</sup>

Generally, metal complex photosensitizers consist of a central metal ion with ancillary ligands having at least one anchoring group like -COOH, -H<sub>2</sub>PO<sub>3</sub>, -SO<sub>3</sub>H *etc* to bind at the semiconducting metal surface and to facilitate the injection of the excited electron into the conduction band (CB) of the semiconductor. Light absorption in the visible region of the solar spectrum is due to a metal to ligand charge transfer (MLCT) process. Therefore the central metal ion is crucial in the overall properties of the metal complex dye. Ancillary ligands can be changed to vary the photophysical and electrochemical properties and thereby improving the photovoltaic performance. In this manner the energy levels of the MLCT states can be tuned for optimizing the electron injection and dye regeneration kinetics. The dye sensitizer (photosensitizer) should accomplish some essential characteristics that a photosensitizer should

1. Be photostable.
2. Be electrochemically and thermally stable.
3. Absorb the whole visible region and the near IR (NIR) region.
4. Carry anchoring groups like -COOH, -H<sub>2</sub>PO<sub>3</sub>, SO<sub>3</sub>H *etc* to strongly bind the dye on the surface of semiconductor oxide.
5. LUMO of the sensitizer must match to the edge of the conduction band of the semiconducting metal oxide to minimize the energetic potential losses during the electron transfer reaction.

6. HOMO must be sufficiently low to accept electron donation from an electrolyte or a hole conductive material.

Ruthenium complexes are the widely used dye sensitizer in DSSCs due to their broad absorption spectrum, suitable excited and ground state energy levels, relatively long excited-state lifetime, and good (electro) chemical stability.<sup>104</sup> So far, high conversion efficiencies and durability of photovoltaic devices have been achieved with polypyridyl complexes of ruthenium in which two ligands L = 4, 4'-dicarboxy-2, 2'-bipyridine and thiocyanate ligands have been used. Thus, the ruthenium complex cis-RuL<sub>2</sub>(NCS)<sub>2</sub> known as N3 dye, has become the paradigm of heterogeneous charge transfer sensitizer for dye-sensitized solar cells. The four anchoring groups -COOH present can facilitate the immobilization of sensitizer to the film surface *via* the formation of bidentate coordination and ester linkage with the metal present in the semiconductor photoanode, whilst the -NCS groups enhance the visible light absorption.<sup>104</sup>

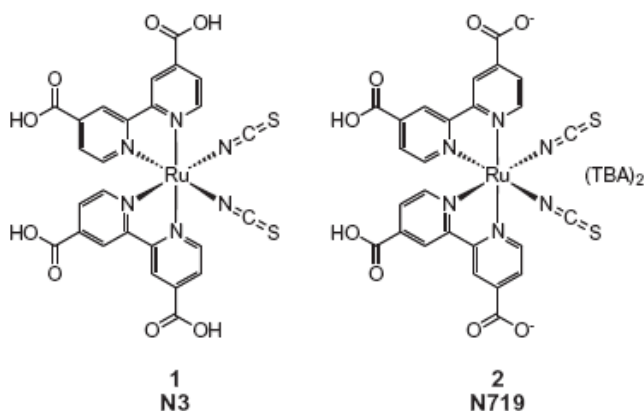


**Figure 1. 2. Chemical structure of N3 and N719 dye.**<sup>105</sup>

Later in 1999, Nazeeruddin *et al.* reported that the N719 dye (dye with two protons and two carboxyl anions) sensitized solar cell exhibited  $17.73 \pm 0.5$  mA current ( $J_{SC}$ ) and a potential ( $V_{OC}$ ) 0.85 V yielded an overall conversion efficiency of 11.18% which was superior to the efficiency that has been achieved by N3 sensitization.<sup>105</sup> Therefore the doubly protonated form, the N719 Ruthenium complex has been the preferred sensitizer in DSSC for many years.<sup>105</sup> The chemical structure of N3 and N719 are shown in **Figure 1. 2**.

### **1. 5. 6. 1. Alternative Dye Systems**

Sensitizers have been synthesized with other metals such as Os,<sup>106</sup> Re,<sup>107</sup> Fe,<sup>108</sup> Ir<sup>109</sup> and Cu.<sup>110</sup> porphyrins<sup>111</sup> and phthalocyanines<sup>112</sup> have also been used as efficient alternative with more than 10% efficiency. Organic dyes (generally with greater molar extinction coefficient) based on coumarin,<sup>113</sup> indoline,<sup>114</sup> Tetrahydroquinoline,<sup>115</sup> Triarylamine,<sup>116</sup> Heteroanthracene,<sup>117</sup> carbazole,<sup>118</sup> N, N-Dialkylaniline,<sup>119</sup> Merocyanine,<sup>120</sup> squaraine<sup>121</sup> and perylene<sup>122</sup> have also been reported at a later stage to assure facility and cost-effectiveness in synthesizing the photosensitizer.

### **1. 5. 7. The Electrolyte<sup>94,123,124</sup>**

An electrolyte containing a redox couple fills the gap between the electrodes in a dye sensitized solar cell. The redox couple is one of the key component in DSSC since the reduced part of the redox couple regenerates the photo-oxidized dye. The oxidized species that has been formed diffuses in to the counter electrode, where it is reduced. The redox couple sets the electrochemical potential at the counter electrode

and therefore the photovoltage of the device depends on the redox couple. It also affects the electrochemical potential of the semiconductor electrode through the recombination kinetics between electrons in  $\text{TiO}_2$  and oxidized redox species. An electrolytic system should

1. Be able to transport the charge carriers between photoanode and counter electrode. After the dye injection in to the CB of the semiconducting metal oxide, the oxidized dye must be rapidly reduced to its ground state. Thus, the choice of the electrolyte should take into account redox potential and regeneration of dye and itself.
2. Ensure fast diffusion of charge carriers, *i.e.* high conductivity and produce good interfacial contact with the mesoporous semiconductor layer and the counter electrode. For liquid electrolytes, the solvent should have smaller leakage and/or evaporation to prevent loss of the liquid electrolyte.
3. Have long-term chemical, thermal, optical, electrochemical, and interfacial stabilities. It must prevent desorption and degradation of the sensitized dye.
4. Not possess significant absorption in the visible light range.

$\text{I}^-/\text{I}_3^-$  system is the widely preferred redox couple in the electrolytic system, since the beginning of DSSC development and still it is the widely used electrolytic system in DSSCs. Advantages of  $\text{I}^-/\text{I}_3^-$  electrolyte are its good solubility, prevention of large absorption of light, suitable redox potential (0.35 V), rapid dye regeneration and very slow recombination kinetics between electrons in semiconductors and

the oxidized part of the redox couple, triiodide ( $I_3^-$ ) respectively. Liquid redox electrolytes, gels, polymers and ionic liquids are the solvents used till date. After the implementation of 4-*tert*-Butylpyridine (TBP) as additive in electrolyte to increase the  $V_{OC}$ , researchers have been widely used the same as an efficient additive in electrolytic system to improve the performance of DSSC.

In DSSCs, the reaction between oxidized dye and iodide ion ( $I^-$ ) in the redox couple leads to the formation of diiodide radicals ( $I_2^{\bullet-}$ ).<sup>125,126</sup> This radical was observed using nanosecond-laser spectroscopy and pseudo-steady-state photoinduced absorption spectroscopy.<sup>125,126</sup> The pathway for the reduction of the oxidized dye ( $D^+$ ) by iodide is given by **equations 1. 16 - 1. 19**.<sup>127,128,129</sup>



### 1. 5. 7. 1. Alternative Electrolytic Systems

$\text{LiBr}/\text{Br}_2$ ,<sup>130</sup>  $\text{Br}^-/\text{Br}_3^-$ ,<sup>131</sup>  $\text{SCN}^-/(\text{SCN})_3^-$ ,<sup>132</sup>  $\text{SeCN}^-/(\text{SeCN})_3^-$ <sup>133</sup> and sulfur containing redox couple<sup>134</sup> have been used as alternative redox couples in DSSCs. As opposed to redox electrolytes where charge transport is due to movement of redox molecules, organic hole conductors were arised, where positive charge moves by a hopping mechanism between neighboring molecules or moieties.<sup>135</sup> In this manner conducting

polymers and molecular hole conductors have been used. Inorganic hole conductors such as CuI,<sup>136</sup> CuSCN,<sup>137</sup> CuBr<sup>138</sup> based sulfur compound, NiO,<sup>139</sup> and ferrocene<sup>140</sup> have also been employed as suitable alternative to the redox electrolytic system.

### **1. 5. 8. Counter Electrode<sup>94,141,142</sup>**

Counter electrode (CE) is the vital part of a DSSC that collect electrons from the external circuit and catalyzes I<sub>3</sub><sup>-</sup> reduction in the electrolyte. For an increased performance a CE should have

1. 80% optical transparency at a wavelength of 550 nm.
2. Compatible charge transfer resistance (R<sub>ct</sub>)
3. High chemical stability
4. High specific surface area

Pt can be deposited at TCO using a range of methods such as electrodeposition,<sup>143</sup> spray pyrolysis,<sup>144</sup> sputtering<sup>145</sup> and pulsed laser deposition.<sup>146</sup> Best performance and durable DSSC has been achieved with nanoscale Pt clusters prepared by thermal decomposition of platinum chloride compounds.<sup>147</sup> Due to very low Pt-loadings (5 μgcm<sup>-2</sup>) the CE remains transparent. Charge transfer resistances of less than 1 Ω cm<sup>2</sup> was achieved.

#### **1. 5. 8. 1. Alternative Counter Electrodes**

Carbon materials (such as Carbon nanotube,<sup>148</sup> carbon nanotube-graphene,<sup>149</sup> MoS<sub>2</sub>-carbon nanotubes<sup>150</sup> and graphene<sup>151</sup>), conducting polymers (such as Poly (3, 4- ethylenedioxythiophene) or PEDOT,<sup>152</sup> polyaniline<sup>153</sup> and polypyrrole<sup>154</sup>), cobalt sulphide,<sup>155</sup> Mo<sub>2</sub>C,<sup>156</sup> WC<sup>157</sup> *etc.* have been experimented as CE in DSSCs.

### 1. 5. 9. Energy Parameters and their Calculations

The sun emits light with a range of wavelengths from UV, visible and infrared (IR). When the skies are clear, maximum radiation from the sun strikes at the surface of earth. When the sun is directly overhead, the path to earth surface will be the shortest. The path length is called the air mass (AM) and can be approximately calculated as<sup>94</sup>

$$AM = 1/\cos \varphi \quad (1. 20)$$

$\varphi$  is the angle of elevation of the sun and which is  $42^\circ$  in the standard solar spectrum used for solar cell efficiency measurements, AM 1.5 G (Global). The spectrum is normalized so that the amount of radiant energy received from sun per unit area per unit time (Integrated irradiance) is  $1000 \text{ Wm}^{-2}$ . Depending on the position of sun, earth orientation and sun's condition, the irradiance varies. When the cell voltage outputs increase solar cell efficiency also increase.

The AM 1.5 G solar radiation spectrum can be found from different sources. The maximum current for a solar cell device converting all incident photons below the absorption onset wavelength into electric current can also indicate from this diagram. The efficiency,  $\eta$ , for a solar cell is given by,<sup>98</sup>

$$\eta = J_{SC} V_{OC} FF/ P_{in} \quad (1. 21)$$

Where  $J_{SC}$  is the short circuit current,  $V_{OC}$  – open circuit photo voltage,  $FF$  – fill factor of the cell,  $P_{in}$  - intensity of the incident light.

$FF$  may have the value between 0 and less than one. The fill factor is the ratio of the maximum power ( $P_{\max}$ ) of the solar cell per unit area divided by the  $V_{OC}$  and  $J_{SC}$ ,<sup>99</sup>

$$FF = P_{\max} / (J_{SC} V_{OC}) \quad (1. 22)$$

The incident monochromatic photon to current conversion efficiency (IPCE) or the “external quantum efficiency” (EQE), is an important characteristic of a device which is useful in comparing the light-harvesting performance of sensitizers, where the devices are with same architecture. The IPCE may be defined as the number of electrons generated by light in the external circuit divided by the number of incident photons as a function of excitation wavelength, **Equation 1. 23**.<sup>94</sup>

$$\begin{aligned} \text{IPCE} &= \text{photocurrent density}/(\text{wavelength} \times \text{photon flux}) \\ &= \text{LHE}(\lambda) \times \phi_{\text{inj}} \times \eta_{\text{coll}} \end{aligned} \quad (1. 23)$$

where LHE ( $\lambda$ ) is the light-harvesting efficiency at wavelength  $\lambda$ ,  $\phi_{\text{inj}}$  is the quantum yield for electron injection from the excited sensitizer in the conduction band of the  $\text{TiO}_2$ , and  $\eta_{\text{coll}}$  is the efficiency for the collection of electrons.

As a whole, the present research work focuses mainly on the synthesis and characterization of semiconducting  $\text{TiO}_2$  and  $\text{ZnO}$ ; the most promising materials for harvesting sunlight and their applications in the area of photocatalysis and dye sensitized solar cells.

## **1. 6. Objectives of the Thesis**

The main objectives of the present research programme are

1. Synthesis of nano/micro semiconducting metal oxides of  $\text{TiO}_2$  and  $\text{ZnO}$  architectures having different morphology using various strategies such as sol-gel, microwave, gel combustion and solution processing.
2. Tuning of the band gap of the aforementioned semiconducting oxides for appropriate light harvesting applications.
3. To increase/decrease the textural properties and/or surface defects such as oxygen richness and oxygen deficiency by modifying the synthesis procedure.
4. Characterization of the above nano/micro semiconducting metal oxide architectures.
5. Investigation of the nano/micro architectures using methylene blue (MB) dye as model system for photocatalytic applications.
6. Fabrication of dye sensitized solar cells (DSSC) using nano/micro architectures.

## **1. 7. Overview of the Experimental Work**

The experimental methods, characterization techniques used and results and discussion obtained were included under chapters from 2 to 7. In chapter 2, all the experimental procedures adopted were described. In Chapter 3, a green and rapid microwave syntheses of

‘yellow oxygen rich’ (YAT-150) and ‘black oxygen vacancy rich’ (BAT-150) anatase TiO<sub>2</sub> nanoparticles have been discussed. Its photocatalytic activity was investigated and compared with standard Degussa-P25 under sunlight illumination. In Chapter 4, a one pot gel combustion synthetic strategy has been discussed for the formation of self-doped black anatase TiO<sub>2-x</sub> (BAT) using titanium butoxide, diethylene glycol (DEG) and water as the only precursors and its photocatalytic activity was investigated and compared with standard Degussa-P25 under sunlight illumination. In Chapter 5, dopant free, solar active ZnO photocatalysts with oxygen vacancy richness were achieved by a solution processing strategy followed by calcination at various temperatures 300, 500, 700, 800 and 900 °C. Methylene blue (MB) dye was used as model system for photocatalytic experiments and their photoactivities were also compared the activity of the commercially available photocatalyst Degussa- P25 under solar illumination. In Chapter 6, a facile and rapid synthesis of mesoporous anatase TiO<sub>2</sub> nanoparticles and their application as photoanode material for DSSCs are discussed. In Chapter 7, synthesis of nanoribbon ZnO with 25 nm average particle size has been synthesized by a facile sol-gel synthesis and application of this material as photoanode material in DSSC is discussed.

## References

1. W. Ostwald, *Die M\_hle des Lebens*, T. Thomas, Leipzig, 1911.
2. J. Potocnik, *Science*, 2007, **315**, 810.

3. A. Kubacka, M. Fernandez-Garcia and G. Colon, *Chem. Rev.*, 2011, **112**, 1555.
4. O. Carp, C. L. Huisman and A. Reller, *Prog. Solid State Chem.*, 2004, **32**, 33.
5. V. Etacheri, C. Di Valentin, J. Schneider, D. W. Bahnemann and S. C. Pillai, *J. Photochem. Photobiol. C: Photochem. Rev.*, 2015, **25**, 1.
6. U. Bach, D. Lupo, P. Comte, J. E. Moser, F. Weissörtel, J. Salbeck and M. Grätzel, *Nature*, 1998, **395**, 583.
7. G. K. Mor, K. Shankar, M. Paulose, O. K. Varghese and C. A. Grimes, *Nano Lett.*, 2006, **6**, 215.
8. D. Chen, F. Huang, Y. B. Cheng and R. A. Caruso, *Adv. Mater.*, 2009, **21**, 2206.
9. K. Keis, E. Magnusson, H. Lindstrom, S. E. Lindquist and A. Hagfeldt, *Sol. Energ. Mater. Sol. Cells*, 2002, **73**, 51.
10. M. Grätzel, *Nature*, 2001, **414**, 338.
11. R. Levinson, P. Berdahl and H. Akbari, *Sol. Energy Mater. Sol. Cells*, 2005, **89**, 319.
12. P. Periyat, K. V. Baiju, P. Mukundan, P. K. Pillai and K. G. K. Warriar, *J. Sol-Gel Sci. Technol.*, 2007, **43**, 299.
13. X. Chen and C. Burda, *J. Am. Chem. Soc.*, 2008, **130**, 5018.

14. J. Qiu, S. Li, E. Gray, H. Liu, Q. F. Gu, C. Sun and S. Zhang, *J. Phys. Chem. C*, 2014, **118**, 8824.
15. J. Zheng, Y. Liu, G. Ji, P. Zhang, X. Cao, B. Wang, C. Zhang, X. Zhou, Y. Zhu and D. Shi, *ACS Appl. Mater. Interfaces*, 2015, **7**, 23431.
16. L. Kong, C. Wang, H. Zheng, X. Zhang and Y. Liu, *J. Phys. Chem. C*, 2015, **119**, 16623.
17. S. Sakthivel, M. Janczarek and H. Kisch, *J. Phys. Chem. B*, 2004, **108**, 19384.
18. M. Wang, B. Nie, K. K. Yee, H. Bian, C. Lee, H. K. Lee, B. Zheng, J. Lu, L. Luo and Y. Y. Li, *Chem. Commun.* 2016, **52**, 2988.
19. M. Xing, J. Zhang, B. Qiu, B. Tian, M. Anpo and M. Che, *Small*, 2015, **11**, 1920.
20. J. Zhao, L. Zhang, W. Xing and K. Lu, *J. Phys. Chem. C*, 2015, **119**, 7732.
21. G. Liu, L. C. Yin, J. Wang, P. Niu, C. Zhen, Y. Xie and H. M. Cheng, *Energy Environ. Sci.*, 2012, **5**, 9603.
22. X. Yu, B. Kim and Y. K. Kim, *ACS Catal.*, 2013, **3**, 2479.
23. G. Li, Z. Zhang, H. Peng and K. Chen, *RSC Adv.*, 2013, **3**, 11507.

24. X. Zou, J. Liu, J. Su, F. Zuo, J. Chen and P. Feng, *Chem. Eur. J.*, 2013, **19**, 2866.
25. X. Chen, L. Liu, Y. Y. Peter and S. S. Mao, *Science*, 2011, **331**, 746.
26. X. Chen, L. Liu and F. Huang, *Chem. Soc. Rev.*, 2015, **44**, 1861.
27. A. Sinhamahapatra, J. P. Jeon and J. S. Yu, *Energy Environ. Sci.*, 2015, **8**, 3539.
28. Y. Zhu, D. Liu and M. Meng, *Chem. Commun.*, 2014, **50**, 6049.
29. L. Zheng, H. Cheng, F. Liang, S. Shu, C. K. Tsang, H. Li and Y. Y. Li, *J. Phys. Chem. C*, 2012, **116**, 5509.
30. Z. Wang, C. Yang, T. Lin, H. Yin, P. Chen, D. Wan, F. Xu, F. Huang, J. Lin, X. Xie and M. Jiang, *Energy Environ. Sci.*, 2013, **6**, 3007.
31. H. Tan, Z. Zhao, M. Niu, C. Mao, D. Cao, D. Cheng, P. Feng and Z. Sun, *Nanoscale*, 2014, **6**, 10216.
32. T. P. Chou, Q. Zhang and G. Cao, *J. Phys. Chem. C*, 2007, **111**, 18804.
33. J. L. Yang, S. J. An, W. I. Park, G. C. Yi and W. Choi, *Adv. Mater.*, 2004, **16**, 1661.
34. L. Zhang, L. Yin, C. Wang, N. Lun and Y. Qi, *ACS Appl. Mater. Interfaces*, 2010, **2**, 1769.

35. B. Liu and H. C. Zeng, *J. Am. Chem. Soc.*, 2003, **125**, 4430.
36. P. Rai, W. K. Kwak and Y. T. Yu, *ACS Appl. Mater. Interfaces*, 2013, **5**, 3026.
37. X. H. Wang, L. Q. Huang, L. J. Niu, R. B. Li, D. H. Fan, F. B. Zhang and Q. X. Guo, *J. Alloys Compd.*, 2015, **622**, 440.
38. S. C. Lyu, Y. Zhang, C. J. Lee, H. Ruh and H. J. Lee, *Chem. Mater.*, 2003, **15**, 3294.
39. S. C. Padmanabhan, D. Ledwith, S. C. Pillai, D. E. McCormack and J. M. Kelly, *J. Mater. Chem.*, 2009, **19**, 9250.
40. J. Xu, Q. Pan and Z. Tian, *Sensors Actuators B: Chem.*, 2000, **66**, 277.
41. Z. L. Wang and J. Song, *Science*, 2006, **312**, 242.
42. Z. L. Wang, *Nano Today*, 2010, **5**, 540.
43. Q. Zhang, C. S. Dandeneau, X. Zhou and G. Cao, *Adv. Mater.*, 2009, **21**, 4087.
44. T. P. Chou, Q. Zhang, G. E. Fryxell and G. Cao, *Adv. Mater.*, 2007, **19**, 2588.
45. E. M. Kaidashev, M. Lorenz, H. von Wenckstern, A. Rahm, H. C. Semmelhack, K. H. Han, G. Benndorf, C. Bundesmann, H. Hochmuth and M. Grundmann, *Appl. Phys. Lett.*, 2003, **82**, 3901.

46. C. J. Brinker and G. W. Scherer, *Sol-gel science: The Physics and Chemistry of Sol-gel Processing*. Academic Press, 2013
47. K. C. Patil, S. T. Aruna and T. Mimani, *Curr. Opin. Solid State Mater. Sci.*, 2002, **6**, 507.
48. M. Oghbaei and O. Mirzaee, *J. Alloys Compd.*, 2010, **494**, 175.
49. Z. Yin, Z. Wang, Y. Du, X. Qi, Y. Huang, C. Xue and H. Zhang, *Adv. Mater.*, 2012, **24**, 5374.
50. Z. Xu and J. Lin, *Rev. Nanosci. Nanotechnol.*, 2013, **2**, 225.
51. R. I. Walton, *Chem. Soc. Rev.*, 2002, **31**, 230.
52. W. E. Teo and S. Ramakrishna, *Nanotechnol.*, 2006, **17**, R89.
53. H. O. Pierson, *Handbook of Chemical Vapor Deposition: Principles, Technology and Applications*. William Andrew., 1999.
54. U. Helmersson, M. Lattemann, J. Bohlmark, A. P. Ehiasarian and J. T. Gudmundsson, *Thin Solid Films*, 2006, **513**, 1.
55. Q. Xu and M. A. Anderson, *J. Am. Ceram. Soc.*, 1994, **77**, 1939.
56. A. Feinle, M. S. Elsaesser and N. Hüsing, *Chem. Soc. Rev.*, 2016, **45**, 3377.
57. I. Hong, *J. Ind. Eng. Chem.*, 2006, **12**, 918.

58. Y. Zhang, Y. Ding, J. Gao and J. Yang, *J. Eur. Ceram. Soc.*, 2009, **29**, 1101.
59. J. F. Chen, Y. H. Wang, F. Guo, X. M. Wang and C. Zheng, *Ind. Eng. Chem. Res.*, 2000, **39**, 948.
60. M. Zhou, J. Yu, S. Liu, P. Zhai and B. Huang, *Appl. Catal. B: Environ.*, 2009, **89**, 160.
61. A. Imhof and D. J. Pine, *Adv. Mater.*, 1998, **10**, 697.
62. A. Pimentel, D. Nunes, P. Duarte, J. Rodrigues, F. M. Costa, T. Monteiro, R. Martins and E. Fortunato, *J. Phys. Chem. C*, 2014, **118**, 14629.
63. K. C. Patil, S. T. Aruna and T. Mimani, *Curr. Opin. Solid State Mater. Sci.*, 2002, **6**, 507.
64. D. G. Lamas, R. E. Juárez, A. Caneiro and N. W. de Reça, *Nanostruct. Mater.*, 1998, **10**, 1199.
65. P. V. A. Padmanabhan, K. P. Sreekumar, T. K. Thiyagarajan, R. U. Satpute, K. Bhanumurthy, P. Sengupta, G. K. Dey and K. G. K. Warriar, *Vacuum*, 2006, **80**, 11.
66. U. I. Gaya and A. H. Abdullah, *J. Photochem. Photobiol. C: Photochem. Rev.*, 2008, **9**, 1.
67. H. Yang and H. Cheng, *Sep. Purif. Technol.*, 2007, **56**, 392.

68. M. Pera-Titus, V. Garcia-Molina, M. A. Baños, J. Giménez and S. Esplugas, *Appl. Catal. B: Environ.*, 2004, **47**, 219.
69. J. A. Byrne, P. S. M. Dunlop, J. W. J. Hamilton, P. Fernández-Ibáñez, I. Polo-López, P. K. Sharma and A. S. M. Vennard, *Molecules*, 2015, **20**, 5574.
70. M. R. Hoffmann, S. T. Martin, W. Choi and D. W. Bahnemann, *Chem. Rev.*, 1995, **95**, 69.
71. A. Fujishima and K. Honda, *Nature*, 1972, **238**, 37.
72. J. Verne, *The Mysterious Island*, 1874, chapter 11, 187.
73. A. L. Linsebigler, G. Lu and J. T. Yates Jr, *Chem. Rev.*, 1995, **95**, 735.
74. K. M. Lee, C. W. Lai, K. S. Ngai and J. C. Juan, *Water Res.*, 2016, **88**, 428.
75. T. Daimon, T. Hiraoka, M. Kitazawa, J. Suetake and Y. Nosaka, *Appl. Catal. A*, 2008, **340**, 169.
76. K. T. Ranjit, I. Willner, S. H. Bossmann and A. M. Braun, *Environ. Sci. Technol.*, 2001, **35**, 1544.
77. J. C. Colmenares and R. Luque, *Chem. Soc. Rev.*, 2014, **43**, 765.
78. P. Periyat, K. V. Baiju, P. Mukundan, P. K. Pillai and K. G. K. Warriar, *Appl. Catal. A: Gen.*, 2008, **349**, 13.

79. M. K. Kavitha, S. C. Pillai, P. Gopinath and H. John, *J. Environ. Chem. Eng.*, 2015, **3**, 1194.
80. W. Lei, T. Zhang, L. Gu, P. Liu, J. A. Rodriguez, G. Liu and M. Liu, *ACS Catal.*, 2015, **5**, 4385.
81. Y. C. Zhang, Z. N. Du, K. W. Li, M. Zhang and D. D. Dionysiou, *ACS Appl. Mater. Interfaces*, 2011, **3**, 1528.
82. W. Zhao, W. Zhao, G. Zhu, T. Lin, F. Xu and F. Huang, *Dalton Trans.*, 2016, **45**, 3888.
83. S. Nishioka and K. Maeda, *RSC Adv.*, 2015, **5**, 100123.
84. L. Mu, Y. Zhao, A. Li, S. Wang, Z. Wang, J. Yang, Y. Wang, T. Liu, R. Chen, J. Zhu and F. Fan, *Energy Environ. Sci.*, 2016, **9**, 2463.
85. H. Tong, S. Ouyang, Y. Bi, N. Umezawa, M. Oshikiri and J. Ye, *Adv. Mater.*, 2012, **24**, 229.
86. A. O. Kondrakov, A. N. Ignatev, V. V. Lunin, F. H. Frimmel, S. Bräse and H. Horn, *Appl. Catal. B: Environ.*, 2016, **182**, 424.
87. X. Pan, M. Q. Yang, X. Fu, N. Zhang and Y. J. Xu, *Nanoscale*, 2013, **5**, 3601.
88. B. Parida, S. Iniyan and R. Goic, *Renewable Sustainable Energy Rev.*, 2011, **15**, 1625.
89. E. Bequerel, *C.R. Acad. Sci.*, 1839, **9**, 145.

90. C. E. Fritts, *Am. J. Sci.*, 1883, **26**, 465.
91. J. Chandrasekaran, D. Nithyaprakash, K. B. Ajjan, S. Maruthamuthu, D. Manoharan and S. Kumar, *Renewable Sustainable Energy Rev.*, 2011, **15**, 1228.
92. A. Rohatgi and J. W. Jeong, *Appl. Phys. Lett.*, 2003, **82**, 224.
93. S. Narasimha, G. Crotty, T. Krygowski, A. Rohatgi and D. L. Meier, In Proceedings of the 26th IEEE Photovoltaic Specialists Conference, IEEE: Piscataway, 1997, 235.
94. A. Hagfeldt, G. Boschloo, L. Sun, L. Kloo and H. Pettersson, *Chem. Rev.*, 2010, **110**, 6595.
95. A. Hagfeldt and M. Grätzel, *Acc. Chem. Res.*, 2000, **33**, 269.
96. M. Grätzel, *Inorg. Chem.*, 2005, **44**, 6841.
97. M. Grätzel, *J. Photochem. Photobiol. C: Photochem. Rev.*, 2003, **4**, 145.
98. M. K. Nazeeruddin, E. Baranoff and M. Grätzel, *Sol. Energy*, 2011, **85**, 1172.
99. M. Grätzel, *J. Photochem. Photobiol. A: Chem.*, 2004, **164**, 3.
100. J. Gong, J. Liang and K. Sumathy, *Renewable Sustainable Energy Rev.*, 2012, **16**, 5848.
101. Q. F. Zhang and G. Z. Cao, *Nano Today*, 2011, **6**, 91.

102. A. S. Polo, M. K. Itokazu and N. Y. M. Iha, *Coord. Chem. Rev.*, 2004, **248**, 1343.
103. M. R. Narayan, *Renewable Sustainable Energy Rev.*, 2012, **16**, 208.
104. D. G. Brown, P. A. Schauer, J. Borau-Garcia, B. R. Fancy and C. P. Berlinguette, *J. Am. Chem. Soc.*, 2013, **135**, 1692.
105. M. K. Nazeeruddin, S. M. Zakeeruddin, R. Humphry-Baker, M. Jirousek, P. Liska, N. Vlachopoulos, V. Shklover, C. H. Fischer and M. Grätzel, *Inorg. Chem.*, 1999, **38**, 6298.
106. T. Swetha, K. R. Reddy and S. P. Singh, *Chem. Rec.*, 2015, **15**, 457.
107. L. Veronese, E. Q. Procopio, F. De Rossi, T. M. Brown, P. Mercandelli, P. Mussini, G. D'Alfonso and M. Panigati, *New J. Chem.*, 2016, **40**, 2910.
108. S. Çakar, N. Güy, M. Özacar and F. Findik, *Electrochim. Acta*, 2016, **209**, 407.
109. A. Sinopoli, C. J. Wood, E. A. Gibson and P. I. Elliott, *Eur. J. Inorg. Chem.*, 2016, **18**, 2887.
110. S. Y. Brauchli, E. C. Constable and C. E. Housecroft, *Dyes Pigm.*, 2015, **113**, 447.
111. W. M. Campbell, K. W. Jolley, P. Wagner, K. Wagner, P. J. Walsh, K. C. Gordon, L. Schmidt-Mende, M. K. Nazeeruddin, Q.

- Wang, M. Grätzel and D. L. Officer, *J. Phys. Chem. C*, 2007, **111**, 11760.
112. S. Mori, M. Nagata, Y. Nakahata, K. Yasuta, R. Goto, M. Kimura and M. Taya, *J. Am. Chem. Soc.*, 2010, **132**, 4054.
113. L. Han, R. Kang, X. Zu, Y. Cui and J. Gao, *Photochem. Photobiol. Sci.*, 2015, **14**, 2046.
114. T. Horiuchi, H. Miura, K. Sumioka and S. Uchida, *J. Am. Chem. Soc.*, 2004, **126**, 12218.
115. K. Rakstys, J. Solovjova, T. Malinauskas, I. Bruder, R. Send, A. Sackus, R. Sens and V. A. Getautis, *Dyes Pigm.*, 2014, **104**, 211.
116. S. Cai, X. Hu, Z. Zhang, J. Su, X. Li, A. Islam, L. Han and H. Tian, *J. Mater. Chem. A*, 2013, **1**, 4763.
117. H. Tian, I. Bora, X. Jiang, E. Gabrielsson, K. M. Karlsson, A. Hagfeldt and L. Sun, *J. Mater. Chem.*, 2011, **21**, 12462.
118. K. Hara, Z. S. Wang, Y. Cui, A. Furube and N. Koumura, *Energy Environ. Sci.*, 2009, **2**, 1109.
119. S. Shalini, R. Balasundaraprabhu, T. S. Kumar, N. Prabavathy, S. Senthilarasu and S. Prasanna, *Int. J. Energy Res.*, 2016, **40**, 1303.
120. T. Meyer, D. Ogermann, A. Pankrath, K. Kleinermanns and T. J. Müller, *J. Organic Chem.*, 2012, **77**, 3704.

121. G. H. Rao, A. Venkateswararao, L. Giribabu and S. P. Singh, *Photochem. Photobiol. Sci.*, 2016, **15**, 287.
122. J. Luo, M. Xu, R. Li, K. W. Huang, C. Jiang, Q. Qi, W. Zeng, J. Zhang, C. Chi, P. Wang and J. Wu, *J. Am. Chem. Soc.*, 2013, **136**, 265.
123. G. Boschloo and A. Hagfeldt, *Acc. Chem. Res.*, 2009, **42**, 1819.
124. H. J. Snaith and L. Schmidt-Mende, *Adv. Mater.*, 2007, **19**, 3187.
125. I. Montanari, J. Nelson and J. R. Durrant, *J. Phys. Chem. B*, 2002, **106**, 12203.
126. C. Bauer, G. Boschloo, E. Mukhtar and A. Hagfeldt, *J. Phys. Chem. B*, 2002, **106**, 12693.
127. S. Pelet, J. E. Moser and M. Grätzel, *J. Phys. Chem. B*, 2000, **104**, 1791.
128. J. N. Clifford, E. Palomares, M. K. Nazeeruddin, M. Grätzel and J. R. Durrant, *J. Phys. Chem. C*, 2007, **111**, 6561.
129. M. Alebbi, C. A. Bignozzi, T. A. Heimer, G. M. Hasselmann and G. J. Meyer, *J. Phys. Chem. B*, 1998, **102**, 7577.
130. K. Hara, T. Horiguchi, T. Kinoshita, K. Sayama and H. Arakawa, *Sol. Energy Mater. Sol. Cells*, 2001, **70**, 151.
131. Z. S. Wang, K. Sayama and H. Sugihara, *J. Phys. Chem. B*, 2005, **109**, 22449.

132. B. V. Bergeron, A. Marton, G. Oskam and G. J. Meyer, *J. Phys. Chem. B*, 2005, **109**, 937.
133. P. Wang, S. M. Zakeeruddin, J. E. Moser, R. Humphry-Baker and M. Grätzel, *J. Am. Chem. Soc.*, 2004, **126**, 7164.
134. D. Li, H. Li, Y. Luo, K. Li, Q. Meng, M. Armand and L. Chen, *Adv. Funct. Mater.*, 2010, **20**, 3358.
135. J. E. Kroeze, N. Hirata, L. Schmidt-Mende, C. Orizu, S. D. Ogier, K. Carr, M. Grätzel and J. R. Durrant, *Adv. Funct. Mater.*, 2006, **16**, 1832.
136. K. Tennakone, G. R. R. A. Kumara, A. R. Kumarasinghe, K. G. U. Wijayantha and P. M. Sirimanne, *Semicond. Sci. Technol.*, 1995, **10**, 1689.
137. B. O'Regan and D. T. Schwartz, *J. Appl. Phys.*, 1996, **80**, 4749.
138. K. Tennakone, G. K. R. Senadeera, D. B. R. A. De Silva and I. R. M. Kottegoda, *Appl. Phys. Lett.*, 2000, **77**, 2367.
139. J. Bandara and H. Weerasinghe, *Sol. Energy Mater. Sol. Cells*, 2005, **85**, 385.
140. M. Congiu, O. Nunes-Neto, M. L. De Marco, D. Dini and C. F. O. Graeff, *Thin Solid Films*, 2016, **612**, 22.
141. S. Yun, A. Hagfeldt and T. Ma, *Adv. Mater.*, 2014, **26**, 6210.

142. S. Thomas, T. G. Deepak, G. S. Anjusree, T. A. Arun, S. V. Nair and A. S. Nair, *J. Mater. Chem. A*, 2014, **2**, 4474.
143. N. Fu, X. Xiao, X. Zhou, J. Zhang and Y. Lin., *J. Phys. Chem. C*, 2012, **116**, 2850.
144. V. Senthilnathan and S. Ganesan, *J. Renewable Sustainable Energy*, 2010, **2**, 063102.
145. G. Calogero, P. Calandra, A. Irrera, A. Sinopoli, I. Citro and G. Di Marco, *Energy Environ. Sci.*, 2011, **4**, 1838.
146. R. Bajpai, S. Roy, P. Kumar, P. Bajpai, N. Kulshrestha, J. Rafiee, N. Koratkar and D. S. Misra, *ACS Appl. Mater. Interfaces*, 2011, **3**, 3884.
147. J. L. Lan, C. C. Wan, T. C. Wei, W. C. Hsu and Y. H. Chang, *Prog. Photovoltaics: Res. Appl.*, 2012, **20**, 44.
148. H. Anwar, A. E. George and I. G. Hill, *Sol. Energy*, 2013, **88**, 129.
149. M. Y. Yen, M. C. Hsiao, S. H. Liao, P. I. Liu, H. M. Tsai, C. C. M. Ma, N. W. Pu and M. D. Ger, *Carbon*, 2011, **49**, 3597.
150. S. Y. Tai, C. J. Liu, S. W. Chou, F. S. S. Chien, J. Y. Lin and T. W. Lin, *J. Mater. Chem.*, 2012, **22**, 24753.
151. D. W. Zhang, X. D. Li, H. B. Li, S. Chen, Z. Sun, X. J. Yin and S. M. Huang, *Carbon*, 2011, **49**, 5382.

152. J. M. Pringle, V. Armel and D. R. MacFarlane, *Chem. Commun.*, 2010, **46**, 5367.
153. W. Hou, Y. Xiao, G. Han, D. Fu and R. Wu, *J. Power Sources*, 2016, **322**, 155.
154. C. Bu, Q. Tai, Y. Liu, S. Guo and X. Zhao, *J. Power Sources*, 2013, **221**, 78.
155. S. S. Rao, C. V. Gopi, S. K. Kim, M. K. Son, M. S. Jeong, A. D. Savariraj, K. Prabakar and H. J. Kim, *Electrochim. Acta*, 2014, **133**, 174.
156. M. Wu, X. Lin, A. Hagfeldt and T. Ma, *Angew. Chem. Int. Ed.*, 2011, **50**, 3520.
157. J. S. Jang, D. J. Ham, E. Ramasamy, J. Lee and J. S. Lee, *Chem. Commun.*, 2010, **46**, 8600.

# 2 Chapter

## Materials and Methods

### Contents

- 2. 1. Experimental Procedures
  - 2. 2. Synthesis of TiO<sub>2</sub> and ZnO Architectures
  - 2. 3. Photocatalysis
  - 2. 4. Dye Sensitized Solar Cell (DSSC)
  - 2. 5. Characterization Techniques Used
- References

### 2. 1. Experimental Procedures

This chapter describes the procedures used for the synthesis of TiO<sub>2</sub> and ZnO nano/microarchitectures studied and various techniques used to characterize the materials those have been synthesized. The first part of the section (section 2. 2) explains the procedure for the preparation of TiO<sub>2</sub> and ZnO nano/micro architectures using microwave, gel combustion, solution processing and sol-gel strategies. The second (section 2. 3) and third sections (section 2. 4), the procedures used to employ the materials in applications such as photocatalysis and dye sensitized solar cells have been discussed. The final part of this section *viz.* the section 2. 5 explains the various technique used for materials characterization. The spectroscopic, optical and surface characterization techniques used for examining the properties of the as prepared TiO<sub>2</sub> and ZnO materials have been summarized. The chemicals used for the sample preparation are tabulated in Table 2.1.

**Table 2. 1. List of Chemicals used for the Synthesis and application studies of TiO<sub>2</sub> and ZnO**

Sl. No.	Name of Chemicals	Name of manufacturer
1	Titanium Butoxide	Sigma Aldrich, 97%
2	Manganese Acetate Tetrahydrate	Sisco Research Lab, India
3	Zinc Nitrate Hexahydrate	Sigma Aldrich, 98%
4	Zinc Acetate Dihydrate	Sigma Aldrich, ACS Reagent
5	Oxalic Acid Dihydrate	Sigma Aldrich, ACS Reagent
6	Isopropanol	Merck, extrapure
7	Diethylene Glycol	Ranbaxy, India
8	Ethanol	Merck
9	Ether	Sisco Research Lab, India
10	Ammonium Hydroxide	Merck, NH <sub>3</sub> Content 30%
11	Sulfuric Acid	Merck, 95-97%
12	Nitric Acid	Merck, 72%
13	Methylene Blue	AR Grade, Qualigens
14	Ethyl Cellulose	Sigma Aldrich
15	Terpineol	Sigma Aldrich
16	N719	Sigma Aldrich
17	Platinic Acid	Sigma Aldrich
18	1,2-Dimethyl-3-Propyl imidazolium iodide	TCI Chemicals, India
19	Lithium Iodide	Lancaster
20	Iodine	Lancaster
21	4- <i>tert.</i> Butyl pyridine	Sigma Aldrich
22	Acetonitrile	Sigma Aldrich

## **2. 2. Synthesis of TiO<sub>2</sub> and ZnO Architectures**

### **2. 2. 1. Synthesis of Yellow and Black Anatase TiO<sub>2</sub>**

For the synthesis of black anatase TiO<sub>2</sub> (BAT-150), titanium butoxide, 0.2 M (6.8 g) was dissolved in 100 mL of isopropanol at room temperature. The above solution was stirred at 1200 rpm for 10 minutes and 0.02 M manganese acetate solution (0.2451 g in 50 mL of water) was added in small quantities (5 mL) for hydrolysis and doping simultaneously. Stirring was continued for a further 30 minutes under the same conditions. The reaction mixture obtained was subjected to microwave irradiation for 5 minutes at 150 °C with 1200 rpm using an Anton- Paar monowave-300 microwave synthesis reactor. The reaction mixture was then cooled to 55 °C. For yellow anatase TiO<sub>2</sub> (YAT-150) synthesis, 50 mL of water was added alone, replacing the 10% manganese acetate solution. Both samples were dried at 80 °C.

### **2. 2. 2. Synthesis of Self-Doped Black Anatase TiO<sub>2-x</sub>**

0.2 M Titanium (IV) butoxide (6.8 g) was mixed with 50 mL diethylene glycol (DEG) followed by 30 minutes stirring at 1200 rpm leading to the formation of yellow titanium glycolate gel.<sup>1</sup> 14.4 mL (8 molar times) of water was added to facilitate sufficient hydroxylation, since the excess hydroxylation can direct towards black TiO<sub>2</sub>.<sup>2</sup> In addition the aqueous mediated reactions lead to crystal phase formation at relatively low calcination temperatures.<sup>3</sup> Stirring was continued for further 15 minutes. The hydrated titanium glycolate gel that has been formed was kept in a muffle furnace at 300 °C for 2 hours. After rapid cooling to room temperature, the sample was

washed using 100 mL each of ethanol, ether and water to remove the organic and inorganic impurities.

### **2. 2. 3. Synthesis of ZnO Microrods**

Zinc Nitrate hexahydrate (18.6 g, 0.25 M) was dissolved in 250 mL of deionized water. The solution was stirred at 1200 rpm and 19.3 mL of  $\text{NH}_4\text{OH}$  was added to make the solution basic (pH 8). White  $\text{Zn}(\text{OH})_2$  formed was washed with water continuously till the  $\text{NO}_3^-$  ions present in the  $\text{Zn}(\text{OH})_2$  sample gets completely removed. Absence of  $\text{NO}_3^-$  ion was tested by reacting the filtrate with concentrated  $\text{H}_2\text{SO}_4$  and a paper ball. The experiment using the filtrate was repeated until the paper ball showed no brown color. This confirms that all the  $\text{NO}_3^-$  ions present in the solution were completely removed.  $\text{Zn}(\text{OH})_2$  precipitate was then dispersed into 300 mL of deionized water. 10% of  $\text{HNO}_3$  was added to the mixture with constant stirring at 600 rpm till it reaches at pH 6 and subjected to further 3 hrs stirring at 1200 rpm again. It then heated at  $100\text{ }^\circ\text{C}$ , which is the ZnO precursor. The precursor sample was calcined at 300, 500, 700, 800 and  $900\text{ }^\circ\text{C}$  at a temperature ramp rate of  $5\text{ }^\circ\text{C min}^{-1}$ . The samples are named as ZnO-300, ZnO-500, ZnO-700, ZnO-800 and ZnO-900.

### **2. 2. 4. Synthesis of Microwave Power Induced $\text{TiO}_2$**

This synthetic method is the modified version of the method reported by Periyat *et al.*<sup>4</sup> In a typical experiment 0.4 M titanium butoxide (13.6 g) solution was mixed with 100 mL ethanol. The above solution was stirred for 10 minutes. 28.8 mL of deionized water was added slowly in small quantities using a glass dropper to allow the immediate

formation of a white suspension *via* hydrolysis. The suspension was vacuum dried prior to washing with acetone for the removal of organic moieties. The resultant  $\text{Ti}(\text{OH})_4$  formed was dispersed into 100 mL of deionized water by sonication to obtain a white sol. Stirring was continued for a further 30 minutes. The white sol was subjected to microwave irradiation power of 300 and 600 W in a teflon vessel using a C-MARS microwave. The pressure was released after five minutes cooling and these samples were used for further analysis.

### **2. 2. 5. Synthesis of ZnO Nanoribbons**

The reagents used were zinc (II) acetate dihydrate (Sigma-Aldrich, ACS reagent) and oxalic acid dihydrate (Sigma-Aldrich, ACS reagent). All reagents were used as supplied, and no further purification was carried out. This method is a modified version of the procedure reported by Pillai *et al.*<sup>5</sup> In a typical experiment zinc (II) acetate dihydrate (3.3 g) was dissolved in absolute ethanol (250 mL) and the solution was stirred for 30 minutes using a magnetic stirrer in a fume hood. Oxalic acid dihydrate (3.78 g)  $\text{C}_2\text{O}_4\text{H}_2 \cdot 2\text{H}_2\text{O}$  was dissolved in absolute ethanol (100 mL) and the solution was added slowly, with constant stirring, to the above zinc acetate solution. After the above addition of oxalic acid, a white sol is formed, which was stirred for a further 3 hrs. The suspension was then placed in an oil bath and kept at temperature of 80 °C for 12 hrs to form the xerogel. The xerogel was then calcined in a furnace by heating to 500 °C in air at a rate of 5 °C/min and then holding the sample at this temperature for 2 hrs.

## **2. 3. Photocatalysis**

### **2. 3. 1. Photocatalytic Experiments using TiO<sub>2</sub> and ZnO**

0.01599 g of methylene blue ( $10^{-4}$  M) and 0.0016 g of methylene blue ( $10^{-5}$  M) were made up to 500 mL in a standard flask to get intense blue colored dye solutions. The  $10^{-4}$  M model system was used for investigating the photoactivity of YAT-150 and BAT-150; and  $10^{-5}$  M solution was used for self-doped black anatase TiO<sub>2</sub> and ZnO microrods. 50 mL of the prepared methylene blue dye solution was taken in a beaker. To this solution 0.1g of the TiO<sub>2</sub> or ZnO sample was added and stirred under dark to obtain adsorption-desorption equilibrium that can eliminate any error due to initial adsorption effect. After stirring, it was exposed to direct sunlight/UV light beam with constant stirring. The degradation was monitored by taking 3 mL aliquots at certain time intervals. During the photocatalytic experiments the sunlight intensity was found were different.

During the photocatalytic studies of YAT-150, BAT-150 and BAT, the sunlight intensity was found in the range of 50000-70000 lux and that for ZnO microrods, was found in the range of 80000-90000 lux measured using Lutron, LX-107HA lux meter at Calicut University Campus, Kerala, India (Altitude: 11° 7' 34" North 75° 53' 25" East, Temperature:  $26 \pm 1$  °C) and the UV photocatalytic measurements were carried out using LZC-4X-Luzchem photoreactor at 600 lux intensity for both YAT-150 and BAT-150; and under 650 lux for ZnO microrods.

## **2. 4. Dye Sensitized Solar Cell (DSSC)**

### **2. 4. 1. Solar Cell Fabrication and Testing**

To prepare the DSSC working electrodes, microwave power induced TiO<sub>2</sub> and ZnO nanoribbons were used with the sample procedure. The sample (2 g) was dispersed in minimum quantity of ethanol and ball milled for 2 hrs. The resulting solution was mixed with 20 g of ethyl cellulose (5 wt%) and 7 g terpineol such that the sample: Ethyl cellulose: terpineol ratio was 2: 1: 7. This mixture was stirred for 2 hrs to ensure formation of a uniform dispersion. The mixture was then concentrated into a paste by removing the solvent under vacuum on a rotary evaporator. This paste was printed on an ITO glass using a screen printer. Films of varying thickness were deposited by repeated printing. The film thickness was measured using a profilometer. **2. 4. 2.**

### **Device Assembly**

These sample films were scratched into 4 × 4 mm squares and then sintered at 500 °C for 30 min in air. When the films is cooled to 80 °C, the adsorption of dye on the sample film was carried out by soaking the film in 20 mL of 0.3 mM N719 dye solution at 25 °C for 2 hrs and/or 24 hrs. The resulting dyed sample working electrodes were assembled and sealed with the counter electrodes made by thermal deposition of H<sub>2</sub>PtCl<sub>6</sub> on ITO glass to produce a sandwich type cell. The electrolyte, 0.6 M 1,2-dimethyl-3-propyl imidazolium iodide, 0.1 M LiI (Lancaster), 0.05M I<sub>2</sub> (Lancaster) and 0.5 M 4-tert-butylpyridine (Aldrich) in acetonitrile, was introduced into the cell *via* a vacuum filling method.

### 2. 4. 3. Device Testing

I-V characteristic of solar cells were measured by using a Keithley 2400 Source Meter under illumination of simulated sunlight (100 mW/cm<sup>2</sup>) provided by an Oriel solar simulator with AM 1.5 filter.

### 2. 5. Characterization Techniques Used

#### 2. 5. 1. X-ray Diffraction (XRD)<sup>6</sup>

X-ray diffraction technique is usually used for the characterization of crystalline materials based on the Bragg's law shown below.

$$n\lambda = 2d \sin\theta \quad (2. 1)$$

Where 'λ' is the X-ray wavelength, θ is the angle of diffraction from the lattice plane spaced with a distance 'd' and 'n' is an integer. The intensity of diffracted X-ray from the powder is plotted against 2θ values. XRD patterns of the precursor and calcined samples were obtained from Monash University, Australia, with a Siemens D 500 X-ray diffractometer in the diffraction angle range 2θ = 10-70° using CuK<sub>α</sub> (λ = 1.54 Å) irradiation for microwave power induced TiO<sub>2</sub> and ZnO nanoribbons. For all the other TiO<sub>2</sub> and ZnO sample characterization, Rigaku Miniflex Diffractometer with CuK<sub>α</sub> (λ = 1.54 Å) irradiation available at the Department of Physics, University of Calicut, was used. The diffraction angle range was varied with respect to the sample but limited in the range 20-80°. The spectra were plotted and compared with data from the Joint Committee Powder Diffraction Standards (JCPDS) for analysis. According to the main peak intensity of anatase TiO<sub>2</sub> and wurtzite ZnO respectively, (101) or (100) the

crystallite size was calculated using the Scherrer equation<sup>7</sup> (**Equation 2.2**).

$$\phi = \frac{0.9\lambda}{\beta \cos\theta} \quad (2.2)$$

Where,  $\phi$  = crystallite size (nm),  $\lambda$  = X-ray wavelength ( $\text{\AA}$ ),  $\theta$  = Bragg's angle (radian),  $\beta$  = full width at half maximum (radian).

### 2. 5. 2. FTIR Spectroscopy<sup>8</sup>

FTIR relies on the fact that the most molecules absorb light in the infra-red region of the electromagnetic spectrum. This absorption corresponds specifically to the bonds present in the molecule. The frequency range are measured as wave numbers typically over the range  $4000 - 400 \text{ cm}^{-1}$ . FTIR spectroscopic technique is also used to find out the presence of metal-oxygen, metal-metal, oxygen-oxygen *etc* stretching vibrations of nano/micro semiconducting architectures. Since for the detection of the formation of Ti-O and Zn-O stretching vibrations, the FTIR technique is used here. The FTIR spectra of the samples were measured from the Department of Chemistry, University of Calicut, using a Jasco-FT/IR-4100 spectrophotometer in the range  $4000-400 \text{ cm}^{-1}$ . A measured quantity of the sample was mixed with spectroscopic grade KBr in the ratio 1:100 and ground well followed by the preparation of the sample pellet.

### 2. 5. 3. Raman Spectroscopy<sup>9</sup>

Raman spectroscopy is a molecular spectroscopic technique, which is observed as inelastically scattered light, allows the identification of vibrational (phonon) states of molecules. As a result, Raman

spectroscopy provides an invaluable analytical tool for molecular fingerprinting as well as monitoring changes in molecular bond structure such as defect state, stresses and strains. Raman spectroscopy requires little to no sample preparation and is insensitive to aqueous absorption bands. This property of Raman facilitates the measurement of solids, liquids, and gases not only directly, but also through transparent containers such as glass, quartz, and plastic. Raman measurements of the black TiO<sub>2</sub> sample was obtained using Bruker MultiRam Raman Spectrophotometer available at the Department of Chemistry, University of Calicut and that of the ZnO microrods were recorded from CMET, Thrissur, using thermo-scientific Raman spectrophotometer.

#### **2. 5. 4. X-ray Photoelectron Spectroscopy (XPS)<sup>9</sup>**

XPS is an electron spectroscopic technique, where the kinetic energy of the emitted electron is recorded. The spectrum thus consists of a plot of the number of emitted electrons, or the power of the electron beam, as a function of the energy (or the frequency or wavelength) of the emitted electrons. XPS provides information about not only the atomic composition of a sample but also the structure and oxidation state of the compounds being examined. XPS measurements were recorded from Amrita Institute of Science and Technology, Kochi. The instrument used was Axis Ultra, Kratos Analytical, UK with an Al-K $\alpha$  (1486.6 eV) source.

### **2. 5. 5. Scanning Electron Microscopy (SEM)<sup>10</sup>**

The scanning electron microscope (SEM) uses a focused beam of high energy electrons to generate a variety of signals at the surface of solid specimens. The signals those are derived from electron-sample interactions reveal the information about the sample including surface morphology (texture), chemical composition and crystalline structure of materials. In most applications, data are collected over a selected area of the surface of the sample, and a two dimensional images are generated. The SEM images were obtained from Monash University, Australia by using a JEOL 7001F FESEM operated at 15 kV.

### **2. 5. 6. Transmission Electron Microscopy (TEM)<sup>10</sup>**

TEM is a surface morphological technique, where a high energy beam of electron is applied through a very thin sample and the interactions between the electrons and atoms can be used to observe features such as the structure, dislocations and grain boundaries of a crystal. In addition to these, chemical analysis can also be performed. TEM can be used to study the growth of layers, their composition and defects in semiconductors. High resolution TEM (HRTEM) can be used to analyze the quality, shape and size of various materials especially the nanomaterials. TEM images were recorded from Sophisticated Analytical Instrument Facility (SAIF), Cochin University of Science and Technology (CUSAT) using a JEOL/JEM 2100 Transmission Electron Microscope.

### **2. 5. 7. Photoluminescence Spectroscopy (PL)<sup>9</sup>**

Photoluminescence (PL) spectroscopy is a useful technique for the study of the optical properties of materials. This technique involves measuring the energy distribution of emitted photons after optical excitation. This energy distribution is then analyzed in order to determine the properties of a material, including defect states (species) and defect concentrations. It is widely recognized as a useful tool for characterizing the quality of semiconductor materials which may accompany radiative recombination. PL spectra of ZnO microrod samples were recorded from the Department of Chemistry, NIT, Calicut using Perkin Elmer LS 45 PL spectrophotometer.

### **2. 5. 8. UV-Visible Spectroscopy<sup>11</sup>**

UV-Visible absorption spectroscopy the response of a sample to ultraviolet and visible range of electromagnetic radiation. The principle of UV-Visible spectroscopy is according to Beer Lambert's law which states that the absorbance of a sample is directly proportional to the concentration of the solution and the path length (thickness) of the medium. It can be expressed mathematically as

$$A = \epsilon cl \quad (2.3)$$

Where 'A' is the absorbance, 'ε' is the molar absorptivity, 'c' is the concentration of the solution and 'l' is the path length of the medium.

From the UV-Visible absorption spectra, not only the absorption coverage can be derived but also the band gap of a material especially a semiconductor. The optical properties and absorbance spectra of

samples were measured using a Jasco-V-550-UV/VIS spectrophotometer recorded from the Department of Chemistry, University of Calicut. For the absorption measurement of the MB dye, the aliquots were taken in a PMMA cuvette and scanned in the wavelength range 200-800 nm. The absorption value at a wavelength 662 nm was used for plotting the kinetics of the reaction.

### **2. 5. 9. Dissolved Oxygen Concentration**

The dissolved oxygen concentration (DOC) in the dye solution was calculated using a EUTECH, Cyberscan DO 110 Dissolved Oxygen Meter in each interval of time.

### **2. 5. 10. Surface Area Measurements<sup>12</sup>**

The BET (Brunauer, Emmett and Teller) surface area measurements and pore analysis were carried out at Monash University, Australia, by nitrogen adsorption using a Quantachrome NOVA 2000e surface area analyzer. The measurements were carried out at liquid nitrogen temperature after degassing the powder samples for 2 h at 200 °C.

The specific surface area was determined using the BET equation.<sup>12</sup> In BET theory it is assumed that the adsorption of gas molecules on the solid surface can take place since the solid surface possesses uniform, localized sites. The BET equation is:

$$\frac{P/P_0}{V(1-P/P_0)} = \frac{1}{V_m C} + \frac{(C-1)P/P_0}{V_m C} \quad (2.4)$$

Where,  $V$  = volume of gas adsorbed (in  $\text{cm}^3/\text{g}$ ) at pressure  $P$ .  $V_m$  = volume adsorbed on the surface of the solid is completely covered with a monolayer of adsorbed gas molecules in  $\text{cm}^3/\text{g}$ .  $C$  = a constant depending upon the nature of the gas. Since ' $C$ ' and ' $V_m$ ' are constants for a given gas-solid system, a plot of  $P/V(P_0-P)$  Vs  $P/P_0$  will give a straight line. So  $V_m$  can be calculated. Total surface area of the sample can be calculated using the equation,

$$\text{Surface area (S)} = V_m N_A / M \quad (2.5)$$

Where,  $N$  = Avagadro Number,  $6.023 \times 10^{23} \text{ mol}^{-1}$ ,  $A$  = Cross sectional area of a single molecule of the adsorbate ( $\text{m}^2$ ) and  $M$  = Molecular weight of the adsorbate (g/mol).

## References

1. X. Jiang, Y. Wang, T. Herricks and Y. Xia, *J. Mater. Chem.*, 2004, **14**, 695.
2. C. Fan, C. Chen, J. Wang, X. Fu, Z. Ren, G. Qian and Z. Wang, *Sci. Rep.*, 2015, **5**, 11712.
3. M. Niederberger and G. Garnweitner, *Chem. Eur. J.*, 2006, **12**, 7282.
4. P. Periyat, N. Leyland, D. E. McCormack, J. Colreavy, D. Corr and S. C. Pillai, *J. Mater. Chem.*, 2010, **20**, 3650.
5. S. C. Pillai, J. M. Kelly, D. E. McCormack, P. O'Brien, R. Ramesh, *J. Mater. Chem.*, 2003, **13**, 2586.

6. C. N. R. Rao and J. Gopalakrishnan, *New Directions in Solid State Chemistry*, Cambridge University Press, London, 1997.
7. W. N. Scherrer and R. Jenkins, *Adv. X-ray Anal.*, 1983, **26**, 141.  
b) A. D. Krawitz, *Introduction to Diffraction in Materials Science and Engineering*, Wiley, New York, 2001.
8. D. H. Williams and I. Fleming, *Spectroscopic Methods in Organic Chemistry*, The McGraw- Hill Companies, UK, 1995.
9. D. A. Skoog, F. J. Holler and S. R. Crouch, *Principles of Instrumental Analysis*, Thomson Brooks/Cole, USA, 2007.
10. P. J. Goodhew, J. Humphreys and R. Beanland, *Electron Microscopy and Analysis*, CRC Press, 2000.
11. D. H. Williams and I. Fleming, *Spectroscopic Methods in Organic Chemistry*, The McGraw- Hill Companies, UK, 1995.
12. S. Brunauer, P. H. Emmett and E. J. Teller, *J. Am. Chem. Soc.*, 1938, **60**, 309.

# 3

Chapter

## Microwave Approach towards Oxygen Rich and Oxygen Deficient Black TiO<sub>2</sub> Nanomaterials for Solar Photocatalysis

### Contents

- 3. 1. Introduction
- 3. 2. Results and Discussion
- 3. 3. Conclusions
- References

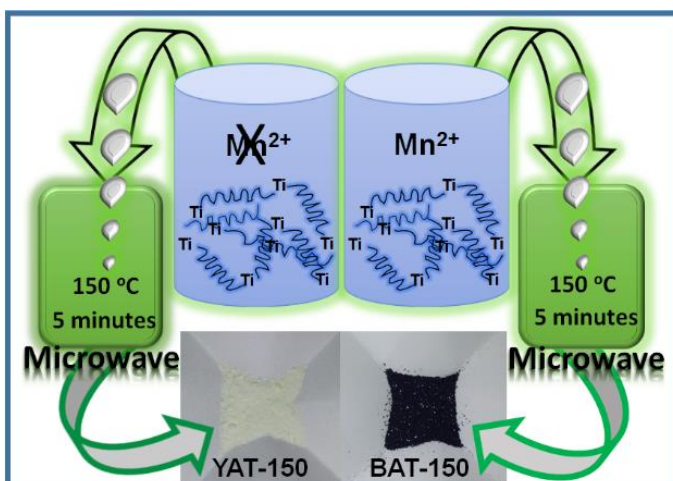
### 3. 1. Introduction

Synthesis of TiO<sub>2</sub> as a sunlight harvester which can absorb the entire solar spectrum from the UV to the IR region using a rapid strategy is a challenge among researchers. It is well known that non-stoichiometry in TiO<sub>2</sub> can alter the absorption coverage of a material, particularly in TiO<sub>2</sub>.<sup>1</sup> If TiO<sub>2</sub> is in an oxygen vacancy rich environment, a substantial positive absorption shift occurs that can facilitate the IR absorption.<sup>1,2</sup> Consequently the color of TiO<sub>2</sub> will be obviously black.<sup>1,2</sup> Very recently oxygen richness and oxygen vacancy richness have been applied on TiO<sub>2</sub> by various methods to induce optical properties and thereby reinforcement of photocatalysis.<sup>1-4</sup> However, the use of oxygen rich chemicals such as H<sub>2</sub>O<sub>2</sub> and high temperature implementation cannot notably alter the oxygen richness in anatase TiO<sub>2</sub> nanocrystals.<sup>4</sup>

For certain, inducing oxygen vacancy richness ( $\text{Ti}^{3+}$  doping) in such an oxygen rich environment is extremely difficult. In this study we are introducing for the first time a clean, cost effective and eco-friendly microwave synthesis of ‘yellow oxygen rich’ (YAT-150) and ‘black oxygen vacancy rich’ (BAT-150) anatase  $\text{TiO}_2$  nanoparticles which can effectively absorb energy from the UV to the IR region of the solar spectrum by in situ modification of the precursor titanium butoxide using Mn (II) acetate as an ‘anatase phase purifier’ within a five minute reaction time.

### **3. 2. Results and Discussion**

In order to construct the light harvesters, oxygen rich yellow anatase  $\text{TiO}_2$  (YAT-150) and oxygen vacancy black rich anatase  $\text{TiO}_2$  (BAT-150), a sol-gel assisted microwave technique was designed, which is schematically represented in **Scheme 3. 1**. As **Scheme 3. 1** depicts, the *in situ* Mn (II) modification led to black anatase  $\text{TiO}_2$  at a temperature of 150 °C whereas oxygen rich anatase  $\text{TiO}_2$  (YAT-150) was obtained without using Mn(II). Both the  $\text{TiO}_2$  samples were employed in photocatalysis under UV and sunlight illumination.<sup>5</sup> Both samples glitter (**Figure 3. 1**).



**Scheme 3. 1. Schematic illustration for the synthesis of yellow and black anatase TiO<sub>2</sub>.**

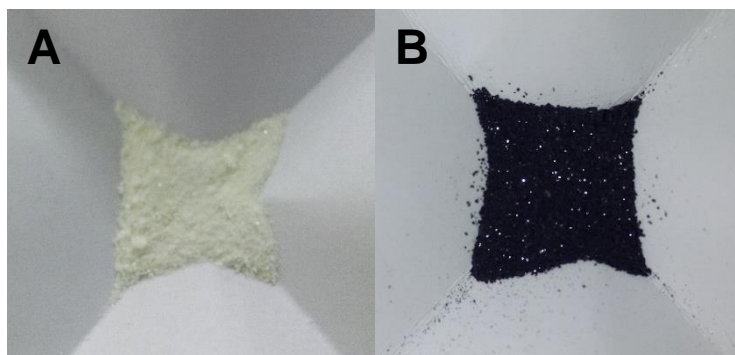


**Figure 3. 1. Digital photographs of A) Yellow anatase TiO<sub>2</sub> (YAT-150) and B) Black anatase TiO<sub>2</sub> (BAT-150).**

### 3. 2. 1. X ray Diffraction

The X-ray diffraction patterns (**Figure 3. 2**) of YAT-150 and BAT-150 confirm the formation of anatase TiO<sub>2</sub> (JCPDS 75-1537) and from **Figure 3. 2B** the overall anatase peak texturing along all directions with respect to YAT-150 (**Figure 3. 2A**) is observed. Interestingly two new anatase peaks along the (103) and (213) directions originate from BAT-150, these are unseen in YAT-150. These new high intensity peaks along the (103) and (213) planes prove the higher phase purity of black anatase TiO<sub>2</sub>. Thus Mn<sup>2+</sup> incorporation (also evident from the absorbance spectra and XPS measurements) into the anatase crystal lattice is directed towards the origin of these new anatase peaks along with peak texturing. Since the ionic radius of Mn<sup>2+</sup> (0.83 Å)<sup>6</sup> is greater than that of anatase Ti<sup>4+</sup> (0.74 Å),<sup>7</sup> Mn<sup>2+</sup> is forced to displace the lattice oxygen leading to oxygen vacancies. This would have definitely contributed towards the in situ location of Mn<sup>2+</sup> in the lattice site of anatase TiO<sub>2</sub> paving the way for oxygen vacancy richness. Although Mn<sup>2+</sup> is larger in size than Ti<sup>4+</sup>, the incorporation was confirmed by the positive shift occurring in the XRD pattern after Mn<sup>2+</sup> modification (inset of **Figure 3. 2**). Furthermore the (211) peak of YAT-150 disappeared and a high index anatase (105) peak was generated on account of the synergistic effects of the thermodynamic and kinetic factors which control crystal nucleation.<sup>8</sup> Mn<sup>2+</sup> modification tends to specifically lower the Gibbs free energy in the (105) orientation, and thus stabilizes the distinct atomic configuration along the (105) plane.<sup>8</sup>

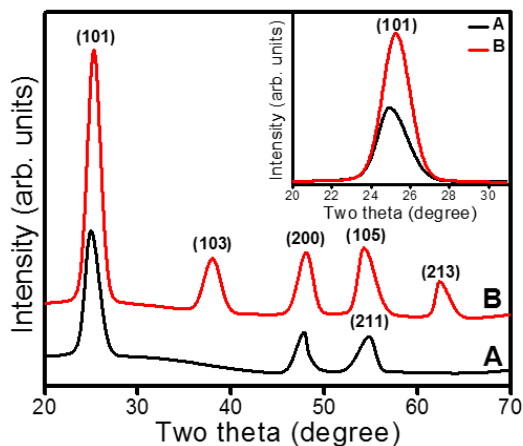


**Figure 3. 2. X ray diffraction pattern of A) YAT-150 and B) BAT-150. (Inset shows the peak shift and peak intensity variation (A) before and (B) after  $Mn^{2+}$  reduction).**

### 3. 2. 2. FTIR Spectroscopy

The FTIR spectra (**Figure 3. 3**) show a broad band around  $550\text{ cm}^{-1}$  for both oxygen rich and oxygen deficient anatase  $TiO_2$ . The assigned peaks for the Ti-O-Ti and Mn-O stretching vibrations are usually present at  $500$  and  $794\text{ cm}^{-1}$  <sup>9,10</sup> respectively which are masked within the broad band present in the range of  $400-900\text{ cm}^{-1}$ . The Ti-OH vibrations generally present at  $740$  and  $670\text{ cm}^{-1}$  may also be merged within the same broad band.<sup>11</sup> The bands at  $3410$  and  $1631\text{ cm}^{-1}$  are due to -OH stretching and bending vibration.<sup>12</sup> The peak at  $1440\text{ cm}^{-1}$  could be ascribed to the stretching vibration of surface adsorbed  $CO_2$ .<sup>13</sup> A noticeable peak is also present at  $1020\text{ cm}^{-1}$  which is the characteristic peak of  $\delta$ -(Ti-OH) deformation and this peak is more

intense for BAT-150, showing the highly deformed crystal lattice of BAT-150.<sup>14</sup>

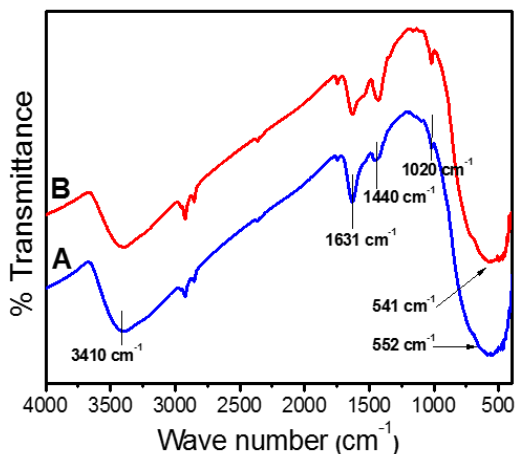


**Figure 3. 3. FTIR spectra of A) YAT-150 and B) BAT-150.**

### **3. 2. 3. UV-Visible Absorption Spectroscopy and Tauc Plot**

For YAT-150, the wavelength cut-off was found to be 520 nm (**Figure 3. 4B**) whereas the absorption of BAT-150 (**Figure 3. 4C**) is beyond the near IR (NIR) region. The former is due to oxygen richness and the latter is obviously because of the origin of oxygen vacancy richness when Ti<sup>3+</sup> doping arose due to Mn<sup>2+</sup> modification. These absorption features have definitely provided a positive contribution towards the higher photocatalytic efficiency of the TiO<sub>2</sub> nanoparticles that have been synthesized. In comparison, the standard Degussa-P25 photocatalyst has a wavelength cut-off in the UV region (**Figure 3. 4A**). The presence of absorption humps for BAT-150 in the range of 362-385 nm and 530-680 nm is associated with the d-d electronic transitions of Mn<sup>2+</sup> in an octahedral environment.<sup>15</sup> The absorption in

the narrower range of 360-385 nm is assigned to  $6A_{1g}(S) \rightarrow 4E_g(D)$  and  $4A_{1g} \rightarrow 4T_{2g}(D)$  transitions, and the  $4A_{1g} \rightarrow 4T_{1g}(G)$  transition reveals the incorporation of  $Mn^{2+}$  alone into the  $TiO_2$  lattice.<sup>15</sup> In the Tauc plot (**Figure 3. 5**) the band gap energy for YAT-150 is 3.02 eV which abruptly decrease to 1.72 eV for BAT-150, which is attributed to the high reduction capability of  $Mn^{2+}$  which has introduced defects into the crystal lattice of  $TiO_2$  directed towards the ultra-narrowed band gap. The reducing agent  $Mn^{2+}$  enters into the oxygen rich anatase  $TiO_2$ , YAT-150 and accepts the excess oxygen cloud leading to BAT-150, the  $Ti^{3+}$  doped black anatase  $TiO_2$ .

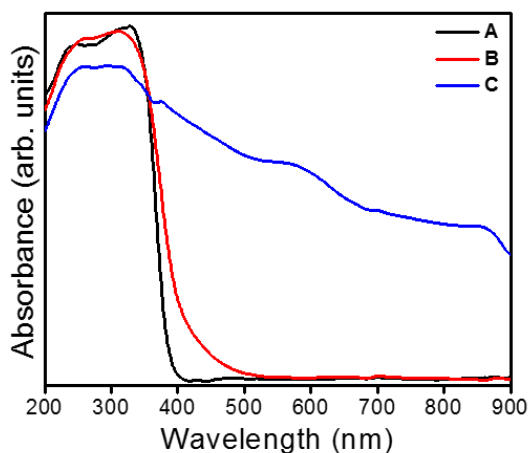


**Figure 3. 4. UV-Visible absorption spectra of A) Degussa-P25 B) YAT-150 and C) BAT-150.**

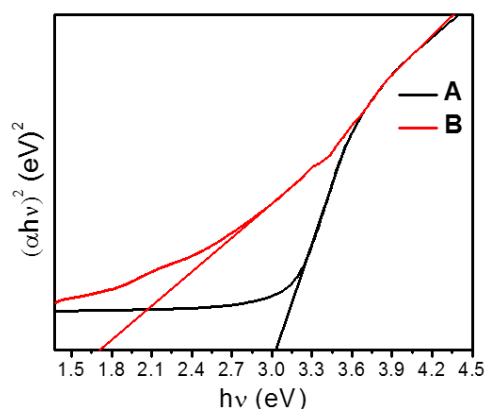


**Figure 3. 5. Tauc plot of A) YAT-150 and B) BAT-150.**

### 3. 2. 4. XPS Analysis

The XPS analysis of YAT-150 (**Figure 3. 6A**) shows that the Ti2p<sub>3/2</sub> and Ti2p<sub>1/2</sub> peaks are at 460.05 and 465.65 eV. These values are reduced to 457.65 and 462.65 eV respectively for BAT-150. For YAT-150, the Ti2p<sub>3/2</sub> peak at 460.05 eV is obviously due to oxygen richness present in the sample<sup>3</sup> whereas for BAT-150 the same peak is negatively shifted to 457.65 eV and is attributed to oxygen vacancy richness (Ti<sup>3+</sup> doping). The Mn2p spectrum (**Figure 3. 6B**), where the binding energy peaks are observed at 640.55, 644.14, 651.95 eV and a satellite peak at 646.95 eV shows the evidence for Mn<sup>2+</sup> doping alone into the crystal lattice of BAT-150.<sup>16</sup> The presence of these peaks is responsible for the negative peak shift occurring for Ti2p<sub>3/2</sub> towards 457.65 eV in BAT-150 and also confirms the Ti<sup>3+</sup> doped oxygen vacancy rich environment.<sup>17</sup> Simultaneously the oxidation state of Ti approaches +3 from +4 (Ti<sup>4+</sup>→Ti<sup>3+</sup>). In the O1s XPS spectrum, the highest binding energy peak corresponding to Ti-O-Ti at 531.35 eV for YAT-150, is negatively shifted to 528.65 eV for BAT-150, which is attributed to the change in oxygen environment<sup>4,18</sup> as shown in **Figure**

**3. 6C.** The peaks at 533.85 and 535.85 eV for YAT-150 prove the presence of Ti-OH and -OH respectively due to surface adsorbed water molecules. For BAT-150, these peaks are shifted to 531.15 and 532.85 eV.<sup>19,20</sup> The splitting between Ti2p<sub>3/2</sub> and Ti2p<sub>1/2</sub> is found to be 5.6 eV for YAT-150 which could be assigned to TiO<sub>2</sub> being in the anatase phase.<sup>21</sup> After Mn<sup>2+</sup> modification the peak separation decreased to 5 eV which could be assigned to the peak texturing, peak formation and the band gap reduction occurring within Ti<sup>3+</sup> doped black anatase TiO<sub>2</sub> (BAT-150). The band gap narrowing occurring due to the transformation of YAT-150 to BAT-150 (from 3.02 to 1.72 eV) as discussed earlier under the UV-Visible absorption spectroscopy and Tauc plot section is due to mid-gap band generation which is revealed from XPS analysis.

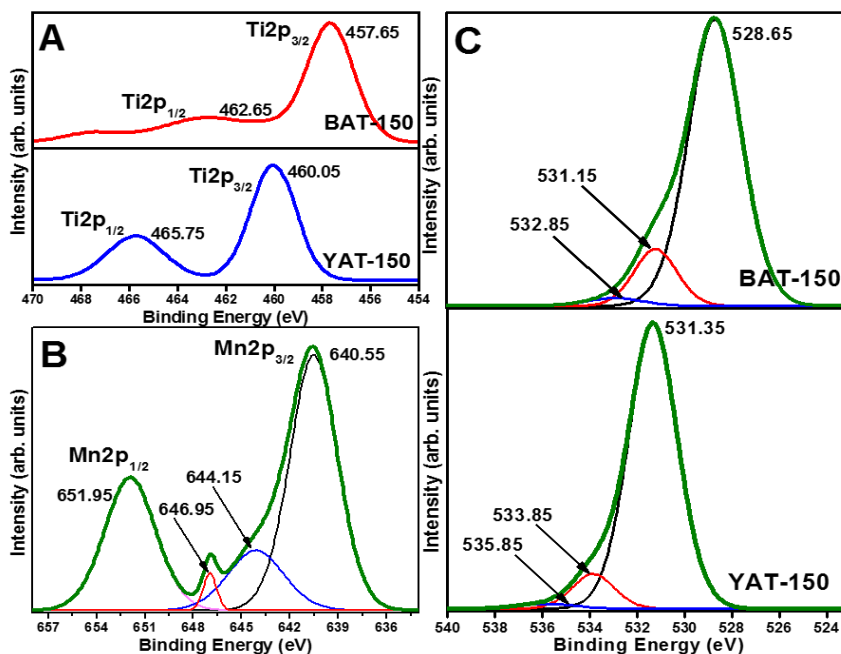


**Figure 3. 6. XPS spectra of A) Ti2p of YAT-150 and BAT-150 B) Mn2p of BAT-150 C) O1s of YAT-150 and BAT-150.**

Mid-gap band states are either above the valence band (VB) or below the conduction band (CB). These mid-band states will overlap with the respective band (VB or CB) leading to a reduction in band gap energy.<sup>2</sup> Here the valence band edge is observed at 2.01 eV and 4.15 eV for YAT-150 and BAT-150, below the Fermi energy confirming the substantial upward binding shift of 2.14 eV by introducing oxygen vacancy richness and simultaneously doping  $\text{Ti}^{3+}$  into the oxygen rich environment (**Figure 3. 7**). Since the optical band gap of YAT-150 is 3.02 eV, the conduction band minimum would occur at -1.01 eV as depicted in the DOS diagram (**Figure 3. 8**). From **Figure 3. 8**, oxygen vacancy rich  $\text{TiO}_2$  (BAT-150) displays a conduction band minimum at 2.43 eV. The increase in the VB maximum is due to the increased oxygen vacancy richness. The degree of oxygen richness is diminished here, which is evident from the XPS spectra *i.e.* the VB maximum colossally increased from 2.01 eV to 4.15 eV (from YAT-150 to BAT-150). These features can be easily perceived from the DOS diagram.

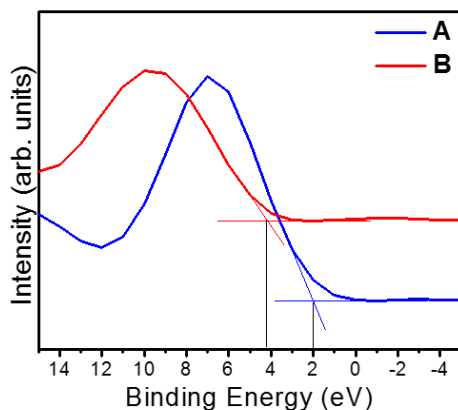


**Figure 3. 7. The Valence band spectra of A) YAT-150 and B) BAT-150.**

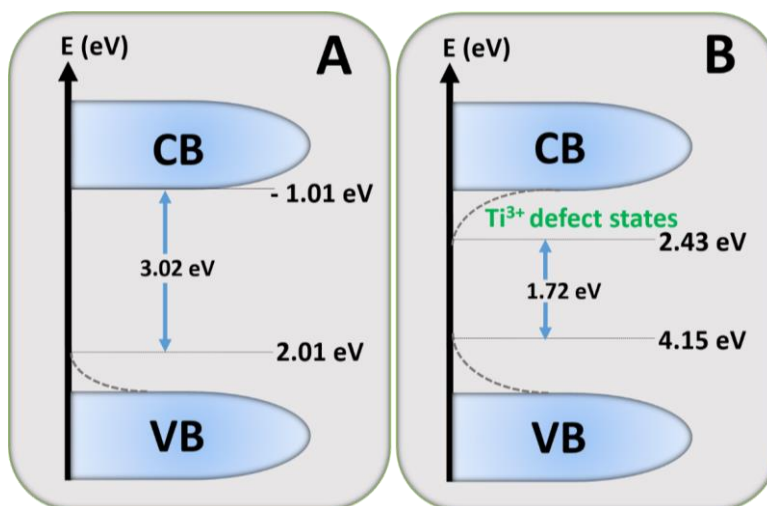


**Figure 3. 8. Density of States (DOS) for A) YAT-150 and B) BAT-150.**

### 3. 2. 5. TEM Analysis

The particle sizes of YAT-150 and BAT-150 are in the nanometer range and are confirmed in the TEM studies (**Figure 3. 9A and 3. 9B**). The TEM studies reveal that both YAT-150 and BAT-150 are ultra-small nanoparticles of around 5 nm in size. No considerable change in size and shape is observed due to the variation in oxygen concentration. The HRTEM images are also displayed here (**Figure 3. 9C and 3. 9D**) and the fringe spacing ( $d$ ) of YAT-150 and BAT-150 is found to be 0.34 and 0.339 nm respectively, which are in exact agreement with the standard data of (101) plane of anatase  $\text{TiO}_2$  (JCPDS 75-1537).<sup>22</sup> The corresponding SAED patterns are also displayed in the insets to show the sharp diffraction pattern and high anatase phase purity.

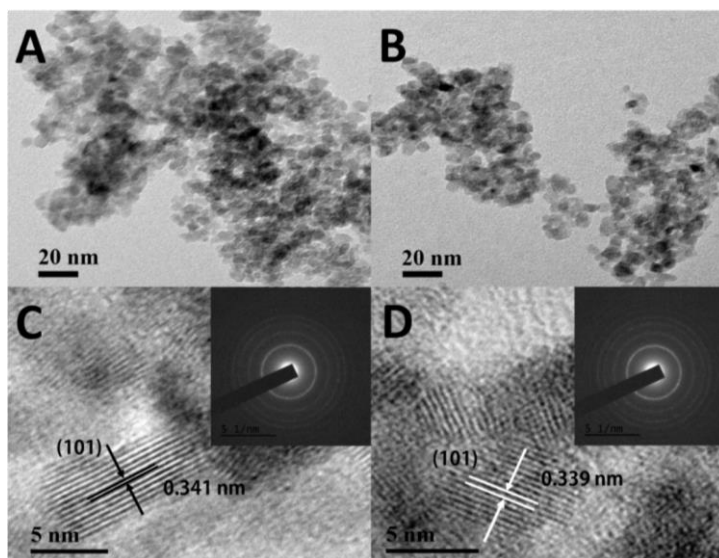


**Figure 3. 9. TEM images of A) YAT-150, B) BAT-150 and HRTEM images of C) YAT-150 D) BAT-150.**

### **3. 2. 6. Photocatalysis**

In order to examine the photocatalytic activity of YAT-150 and BAT-150, methylene blue dye degradation measurements were carried out both under natural sunlight and UV light. The absorption spectra of methylene blue using Degussa-P25 (**Figure 3. 10**), YAT-150 and BAT-150 (**Figure 3. 11**) shows two peaks at 614 and 662 nm that could be assigned to the methylene blue dimer and monomer peaks respectively.<sup>23</sup> Photocatalysis under natural sunlight was performed using YAT-150, BAT-150 and Degussa-P25. These results have projected a captivating outlook for YAT-150 and BAT-150 which have been synthesized using the sol-gel assisted microwave strategy. The photodegradation of the dye occurred within 40 and 20 minutes for YAT-150 and BAT-150 respectively, whereas the commercially

available Degussa-P25 photocatalyst completed the catalytic process, taking more than 90 minutes.

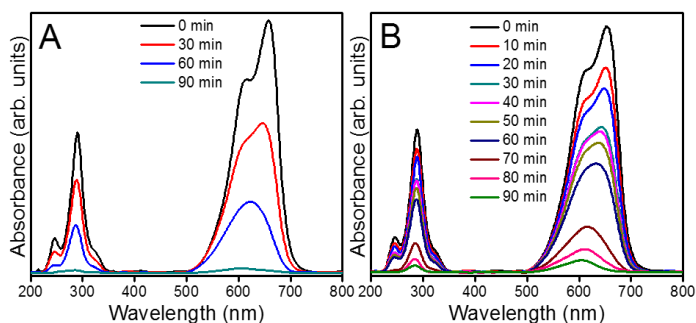


**Figure 3. 10. UV-Visible spectra of photodegradation using Degussa-P25 A) under UV illumination and B) under sunlight illumination.**

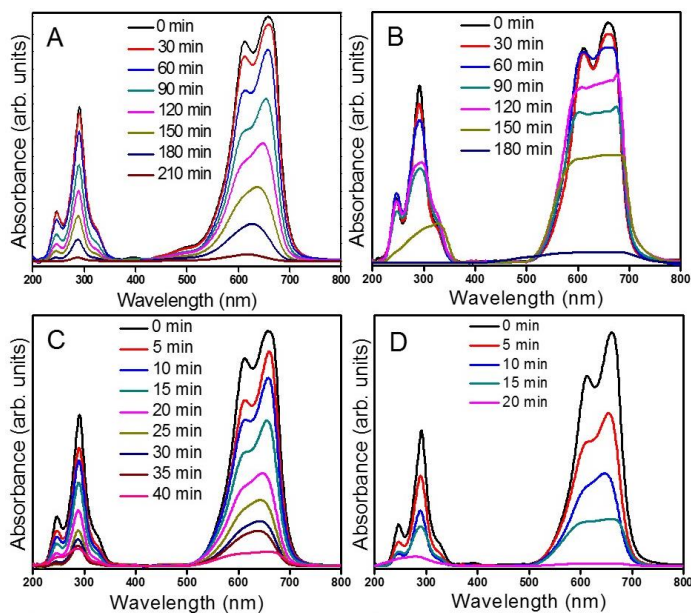
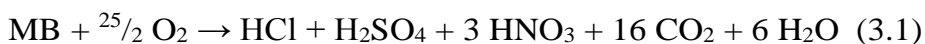


**Figure 3. 11. UV-Visible spectra of photodegradation under UV illumination using A) YAT-150, B) BAT-150 and under sunlight illumination using C) YAT-150, D) BAT-150.**

Generally the photooxidation of methylene blue dye occurs under aerobic conditions, where the amount of dissolved oxygen is sufficient to enhance the photocatalytic process along with the photocatalysts by trapping the electrons that are formed during the photoexcitation of the valence band of TiO<sub>2</sub>. The photooxidation reaction under aerobic conditions can be described by the following equation.<sup>24,25</sup>



Besides the oxidation process, a demethylation process can also occur during dye degradation.<sup>26</sup> In the present work, all photocatalytic measurements were carried out in the presence of air to supply sufficient molecular oxygen. The dissolved oxygen concentration (DOC) measurements were performed and the average DOC values during the photocatalytic process are shown in **Table 3. 1**. This higher concentration of dissolved oxygen in the photocatalytic reaction mixture will have undoubtedly paved the way for enhancing the photocatalytic efficiency by trapping the conduction band electron leading to the formation of super oxide radicals (O<sub>2</sub><sup>-•</sup>) by reduction. The so formed super oxide (O<sub>2</sub><sup>-•</sup>) and hydroxyl (OH<sup>•</sup>) radicals that have been formed due to the reaction between water and the hole generated at the TiO<sub>2</sub> valence band jointly facilitate the photodestruction of the methylene blue dye.<sup>27</sup> These photocatalytic aspects confirmed the remarkable activity of both YAT-150 and BAT-150. BAT-150 is twice as active as YAT-150.

**Table 3. 1. Dissolved Oxygen Concentration in the MB dye solution during photocatalysis (mg/L).**

YAT – 150		BAT – 150		Degussa – P25	
UV	SUNLIGHT	UV	SUNLIGHT	UV	SUNLIGHT
5.42	5.37	5.65	5.43	5.96	4.95

It is evident from **Figure 3. 12** that the photocatalytic activities of YAT-150 and BAT-150 were 2-fold and 4-fold more active than the Degussa-P25 photocatalyst. In the presence of UV illumination, YAT-150 performed the photodegradation within 210 minutes whereas BAT-150 only took 180 minutes. However, Degussa-P25 showed the highest photocatalytic activity under UV light owing to its wide area absorption in the UV region and mixed phase behaviour. The higher adsorption capability of Degussa-P25 as compared to that of YAT-150 and BAT-150 results in the higher photocatalytic efficiency of Degussa-P25 under UV irradiation. Degussa-P25 contains 75% anatase and 25% rutile phase and its high photocatalytic activity has been reported elsewhere.<sup>28,29</sup> BAT-150 utilized the first 60 minutes for monomer-dimer equilibration (a decrease in only the monomer peak) and thereafter the degradation was jointly concerted (**Figure 3. 11B**). Dimerization may facilitate the inhibition of the hazardous activity of toxic active sites. The active sites of organic pollutants are initially restrained by keeping dimerized moieties prior to degradation. For certain, the degradation was performed within 120 minutes. A hypsochromic shift is observed in all the catalytic processes, which is attributed to N-demethylation (**Figure 3. 10 and 3. 11**).<sup>23</sup>

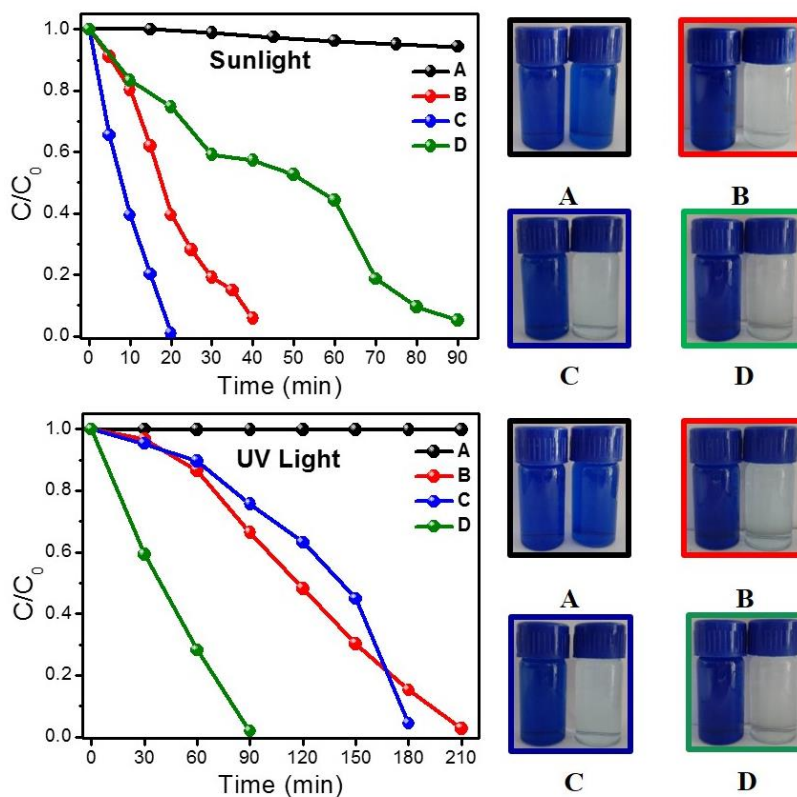


**Figure 3. 12. Photodegradation plot of methylene blue dye degradation under sunlight and UV light using A) No catalyst B) YAT-150, C) BAT-150 and D) Degussa- P25.**

### 3. 3. Conclusions

A green and rapid sol-gel assisted microwave strategy is established for the synthesis of oxygen rich yellow anatase  $\text{TiO}_2$  and  $\text{Ti}^{3+}$  doped oxygen vacancy rich black anatase  $\text{TiO}_2$ . The as synthesized black and yellow anatase  $\text{TiO}_2$  nanoparticles were characterized using XRD, TEM, XPS, FTIR and UV-VIS spectroscopy. XRD studies revealed the origin of new anatase peaks along the (103), (213) and (105)

direction with peak texturing in black anatase TiO<sub>2</sub> when compared to yellow colored anatase TiO<sub>2</sub>. The anatase phase pure yellow and black TiO<sub>2</sub> nanoparticles were of an ultra-small size (~5 nm), confirmed using TEM analysis. XPS studies evidently demonstrated the occurrence of a large upward binding shift of 2.14 eV as anatase TiO<sub>2</sub> changed from an oxygen rich to oxygen vacancy rich environment. These yellow and black anatase TiO<sub>2</sub> nanoparticles were employed as solar photocatalysts and their activity was compared with commercially available Degussa- P25. The photocatalytic efficiencies of yellow and black anatase TiO<sub>2</sub> were two-fold and four-fold more active than the commercially available photocatalyst, Degussa-P25.

## References

1. X. Chen, L. Liu and F. Huang, *Chem. Soc. Rev.*, 2015, **44**, 1861.
2. X. Chen, L. Liu, Y. Y. Peter and S. S. Mao, *Science*, 2011, **331**, 746.
3. L. L. Tan, W. J. Ong, S. P. Chai and A. R. Mohamed, *Chem. Commun.*, 2014, **50**, 6923.
4. V. Etacheri, M. K. Seery, S. J. Hinder and S. C. Pillai, *Adv. Funct. Mater.*, 2011, **21**, 3744.
5. S. Thakur and N. Karak, *J. Mater. Chem. A*, 2015, **3**, 12334.
6. B. Murugan and A. V. Ramaswamy, *J. Phys. Chem. C*, 2008, **112**, 20429.
7. Z. V. Saponjic, N. M. Dimitrijevic, O. G. Poluektov, L. X. Chen, E. Wasinger, U. Welp and T. Rajh, *J. Phys. Chem. B*, 2006, **110**, 25441.

8. H. B. Jiang, Q. Cuan, C. Z. Wen, J. Xing, D. Wu, X. Q. Gong and H. G. Yang, *Angew. Chem. Int. Ed.*, 2011, **50**, 3764.
9. S. C. Pillai, P. Periyat, R. George, D. E. McCormack, M. K. Seery, H. Hayden and S. J. Hinder, *J. Phys. Chem. C*, 2007, **111**, 1605.
10. D. Wang, J. Huang, X. Li, P. Yang, Y. Du, C. M. Goh and C. Lu, *J. Mater. Chem. A*, 2015, **3**, 4195.
11. L. Shao, L. Zhang, M. Chen, H. Lu and M. Zhou, *Chem. Phys. Lett.*, 2011, **343**, 178.
12. R. Nakamura, A. Imanishi, K. Murakoshi and Y. Nakato, *J. Am. Chem. Soc.*, 2003, **125**, 7443.
13. N. T. Nolan, M. K. Seery and S. C. Pillai, *J. Phys. Chem. C*, 2009, **113**, 16151.
14. T. Bezrodna, G. Puchkovska, V. Shymanovska, J. Baran and H. Ratajczak, *J. Mol. Struct.*, 2004, **700**, 175.
15. B. S. Reddy, N. O. Gopal, K. V. Narasimhulu, C. L. Raju, J. L. Rao and B. C. V. Reddy, *J. Mol. Struct.*, 2005, **751**, 161.
16. M. C. Biesinger, B. P. Payne, A. P. Grosvenor, L. W. Lau, A. R. Gerson and R. S. C. Smart, *Appl. Surf. Sci.*, 2011, **257**, 2717.
17. S. Rtimi, J. Nestic, C. Pulgarin, R. Sanjines, M. Bensimon and J. Kiwi, *Interface Focus*, 2015, **5**, 20140046.
18. R. Ren, Z. Wen, S. Cui, Y. Hou, X. Guo and J. Chen, *Sci. Rep.*, 2015, **5**, 10714.

19. T. Leshuk, R. Parviz, P. Everett, H. Krishnakumar, R. A. Varin and F. Gu, *ACS Appl. Mater. Interfaces*, 2013, **5**, 1892.
20. M. M. Khan, S. A. Ansari, D. Pradhan, M. O. Ansari, J. Lee and M. H. Cho, *J. Mater. Chem. A*, 2014, **2**, 637.
21. T. Harifi and M. Montazer, *Appl. Catal. A: Gen.*, 2014, **473**, 104.
22. M. Dürr, A. Schmid, M. Obermaier, S. Rosselli, A. Yasuda and G. Nelles, *Nat. Mater.*, 2005, **4**, 607.
23. D. P. DePuccio, P. Botella, B. O'Rourke and C. C. Landry, *ACS Appl. Mater. Interfaces*, 2015, **7**, 1987.
24. A. Houas, H. Lachheb, M. Ksibi, E. Elaloui, C. Guillard and J. M. Herrmann, *Appl. Catal. B: Environ.*, 2001, **31**, 145.
25. C. Yogi, K. Kojima, N. Wada, H. Tokumoto, T. Takai, T. Mizoguchi and H. Tamiaki, *Thin Solid Films*, 2008, **516**, 5881.
26. T. Zhang, T. Oyama, A. Aoshima, H. Hidaka, J. Zhao and N. Serpone, *J. Photochem. Photobiol. A*, 2001, **140**, 163.
27. J. Yu, X. Zhao and Q. Zhao, *Thin Solid Films*, 2000, **379**, 7.
28. D. C. Hurum, A. G. Agrios, K. A. Gray, T. Rajh and M. C. Thurnauer, *J. Phys. Chem. B*, 2003, **107**, 4545.
29. V. Puddu, H. Choi, D. D. Dionysiou and G. L. Puma, *Appl. Catal. B: Environ.*, 2010, **94**, 211.

# 4 Chapter

## One Pot Gel Combustion Synthesis of Black TiO<sub>2-x</sub> and its Application in Solar Photocatalysis

### Contents

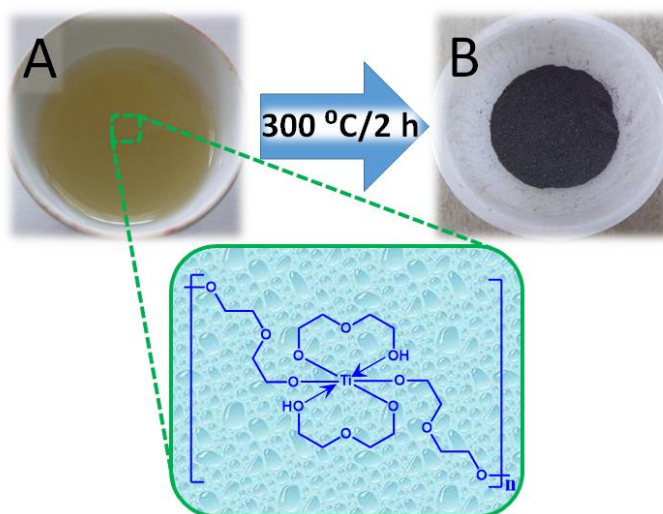
- 4. 1. Introduction
- 4. 2. Results and Discussion
- 4. 3. Conclusions
- References

#### 4. 1. Introduction

An explosion of interest have been triggered after the discovery of black TiO<sub>2</sub> by Chen *et al.* which was substantially able to absorb energy from the IR region of the solar spectrum due to its black color.<sup>1</sup> Different strategies like H<sub>2</sub>/Ar treatment,<sup>2</sup> H<sub>2</sub>-N<sub>2</sub> treatment<sup>3</sup> and argon treatment<sup>4</sup> methods also came in to act for the synthesis of black TiO<sub>2</sub> with desired absorption coverage and applications. Controlling the hydrogenation/argon treatment/nitrogenation procedures along with high pressure conditions have made the synthesis of black TiO<sub>2</sub> difficult and time consuming. The metal reduction method that has been implemented later using Al,<sup>5</sup> Zn<sup>6</sup> and Mg<sup>7</sup> were also accompanied by H<sub>2</sub>/Ar treatments. Due to the persistence of same difficulties, electrochemical anodization<sup>8</sup> was applied on a later stage. Very recently Shah *et al.* reported a facile hydrothermal approach to prepare

defective  $\text{TiO}_{2-x}$  nanocrystals using Ti (III)-salt as a precursor and L-ascorbic acid as reductant and structure direction agent.<sup>9</sup> However, the drawbacks of these methods include the prolonged reaction time and use of a structure directing agent, harsh and expensive chemicals. Keeping these facts in mind, lately we have successfully used Mn (II) for reducing oxygen rich yellow anatase  $\text{TiO}_2$  to oxygen vacancy rich black anatase  $\text{TiO}_2$  which has been explained in the previous chapter of this thesis.<sup>10</sup> Inspired from this facile strategy a rapid synthetic strategy for black anatase  $\text{TiO}_2$  has been developed in a one pot manner, in the absence of any dopant/reducing agents and without any high pressure sophisticated environment along with  $\text{H}_2/\text{N}_2/\text{Ar}$  treatments. In brief, a one pot gel combustion strategy has been used to synthesize  $\text{Ti}^{3+}$  self-doped, oxygen vacancy rich black anatase  $\text{TiO}_{2-x}$  for the first time using titanium butoxide, diethylene glycol and water as only precursors. It has been early reported that gel combustion method can lead to the formation of defects in crystals, such as stacking fault and dislocations.<sup>11</sup> Myung *et al.* recently reported the gel-combustion strategy<sup>4</sup> and Zhang *et al.* reported a sol-gel method<sup>12</sup> in argon atmosphere for the synthesis of defective black  $\text{TiO}_2$ . A very recent report says that the glycolation (used in the present work) can increase the stability of black  $\text{TiO}_2$  nanoparticles in physiological environment, so that it can possess high anticancer effect in vitro and in vivo.<sup>13</sup> Obviously the so formed black  $\text{TiO}_{2-x}$  has shown a wide area absorption at NIR region and correspondingly a narrowed band gap (1.51 eV) which has facilitated the swift and effective photocatalysis under solar illumination.

During synthesis, at the stage of complexation, the precursors are mixed homogeneously in molecular level, so that the possibility for bulk diffusion restriction can be eliminated completely during the anatase phase formation. Rapid cooling after 2 hours can leads to the formation of nanostructures with defects.<sup>14</sup> In this way the defective structures were manipulated that can be correlated with high lattice strain. In other words, if the magnitude of defects are more, more will be the lattice strain. Here the lattice strain ( $\epsilon = 0.334$ , obtained from Rigaku data analysis software, PDXL using Halder-Wagner method) was a large value, indicating the highly defective structure of black  $\text{TiO}_{2-x}$ .<sup>14</sup> The digital photographs and the proposed Ti glycolate gel structure are shown in **Scheme 4. 1**.



**Scheme 4. 1. Digital photographs of (A) Ti glycolate gel and (B) black anatase  $\text{TiO}_{2-x}$  with the Ti glycolate gel structure.**

## 4. 2. Results and Discussion

### 4. 2. 1. X ray Diffraction

The XRD pattern of the black  $\text{TiO}_{2-x}$  sample (**Figure 4. 1A**) revealed the formation anatase phase of  $\text{TiO}_2$  (JCPDS 75-1537). The broad XRD peaks indicate the small average crystallite size of black  $\text{TiO}_{2-x}$  and the average crystallite size was 4.92 nm correspond to the main XRD peak along (101) plane.

### 4. 2. 2. FTIR Spectroscopy

The formation of black  $\text{TiO}_{2-x}$  nanomaterial was further confirmed by FTIR spectrum (**Figure 4. 1B**) and it was found that the broad peak around  $523\text{ cm}^{-1}$  is attributed to the formation of Ti-O-Ti bond of nanotitania.<sup>15</sup> The peaks at  $3430\text{ cm}^{-1}$  and  $1622\text{ cm}^{-1}$  are correspond to the stretching and bending vibrations of -OH present in the nanosystem.<sup>16</sup> Very small FTIR peak intensity at  $\sim 2900\text{ cm}^{-1}$  corresponds to C-H stretching vibrations.<sup>17</sup>

### 4. 2. 3. Raman Spectroscopy

Raman spectrum of BAT (**Figure 4. 1C**) confirms the formation of anatase phase alone. The Raman peaks present are at  $151\text{ cm}^{-1}$  ( $E_g$ ),  $405\text{ cm}^{-1}$  ( $B_{1g}$ ),  $516\text{ cm}^{-1}$  ( $A_{1g}+B_{1g}$ ) and  $637\text{ cm}^{-1}$  ( $E_g$ ).<sup>18</sup> These values indicate a slight increment/decrement in all the Raman shift values as compared to those reported earlier.<sup>18</sup> All the peaks are broad in nature. These facts directing towards the confirmation of a large amount of defects present in the lattice as well as on the surface of BAT, the  $\text{Ti}^{3+}$  self-doped black anatase  $\text{TiO}_{2-x}$ .

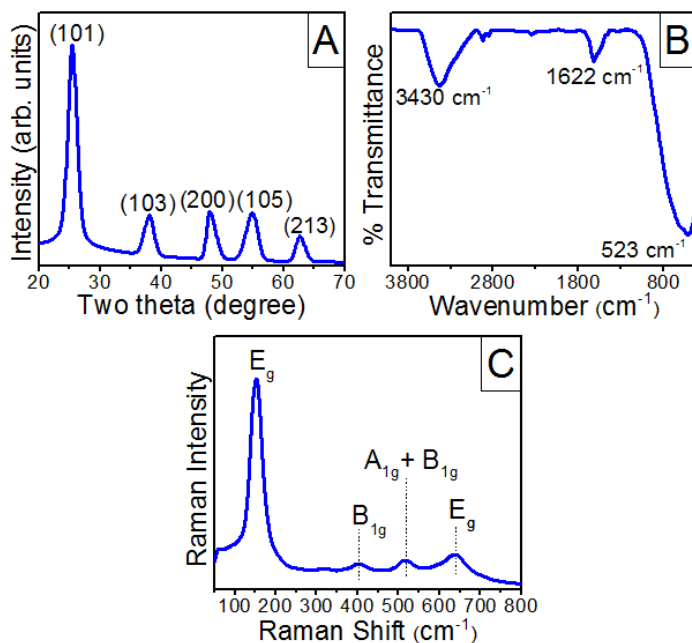


**Figure 4. 1. A) XRD B) FTIR and C) Raman spectrum of BAT.**

#### 4. 2. 4. XPS Analysis

In XPS,  $2p_{3/2}$  and  $2p_{1/2}$  peaks of  $\text{TiO}_2$  are present at 457.6 and 463.3 eV respectively (**Figure 4. 2A**). The peak at 457.6 eV corresponds to the presence of high  $\text{Ti}^{3+}$  concentration.<sup>19</sup> In the O1s XPS spectrum, the Ti–O–Ti peak is observed at 528.7 eV and this reduced value as compared to early reported ones, is attributed to the oxygen vacancy richness present in BAT (**Figure 4. 2B**).<sup>20</sup> The peaks at 531.2 and 532.9 eV confirm the presence of Ti–OH and free -OH species respectively.<sup>21</sup> Very recently Fan *et al.* reported that sufficient hydroxylation can lead to the formation of black  $\text{TiO}_2$ .<sup>22</sup> Evidently the notable band tailing of 0.9 eV observed from VB XPS (**Figure 4. 2C**)

undoubtedly clarifies the existence of highly defective surface structure of  $\text{TiO}_2$ .<sup>1</sup>

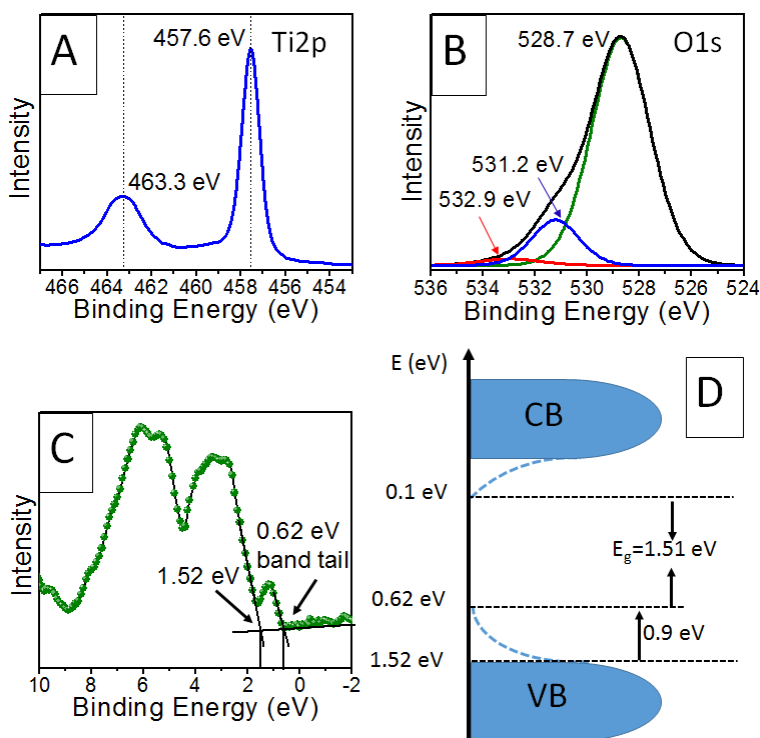


**Figure 4. 2. A) Ti2p XPS, B) O1s XPS, C) Valence band (VB) XPS and D) Density of states (DOS) of BAT.**

The density of States (**Figure 4. 2D**) shows that the narrowed band gap energy of black anatase  $\text{TiO}_{2-x}$  (1.51 eV obtained from Tauc plot, **Figure 4. 4B**) is due to the existence of mid gap band states in between the valence band and the conduction band.<sup>23</sup> The mid gap band states due to VB maximum and CB minimum are mainly due to O2p and Ti3d orbitals respectively. From the DOS diagram (**Figure 4. 2D**), it

can be easily perceived that the main absorption onset of BAT is located at 1.52 eV. In addition the maximum energy associated with band tail, blue shifted, resulting the VB maximum at 0.62 eV. In addition there may be conduction band tail states arising from disorders that extend below the conduction band minimum. In this way, the CB minimum is observed at 0.1 eV.<sup>1,10</sup>

#### **4. 2. 5. TEM Analysis**

A distorted spherical morphology of anatase TiO<sub>2</sub> is observed from TEM analysis (**Figure 4. 3A**). Size of a single black TiO<sub>2-x</sub> nanoparticle was measured which was around 23 nm. The particle size of black TiO<sub>2-x</sub> suggests that five to six nano crystallites combined together to form a single black TiO<sub>2-x</sub> nanoparticle. Furthermore the surface defects present in a single particle is shown in **Figure 4. 3B**. The lattice fringes of TiO<sub>2</sub> are clearly visible at a certain area of the particle and it fades out in a large area which is highlighted in the HRTEM image (**Figure 4. 3B**). Correspondingly the loss of lattice fringe continuum can be easily perceived to predict the defect states present on the surface of a crystal.<sup>24</sup> The SAED pattern of BAT is shown in **Figure 4. 3C**.

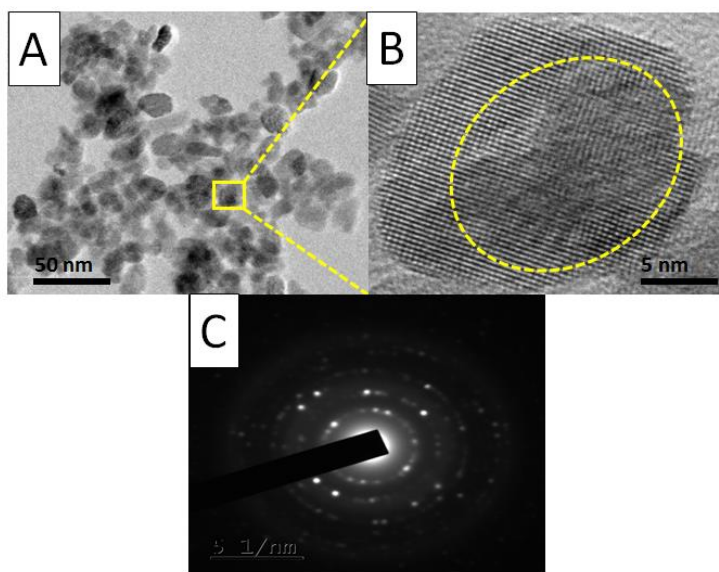


**Figure 4. 3. A) TEM B) HRTEM and C) SAED pattern of BAT (In Figure 4. 3B, region with in the dotted yellow circle visualizes the defective surface layer).**

#### **4. 2. 6. UV-Visible Absorption Spectroscopy and Tauc Plot**

The black colored defective  $\text{TiO}_{2-x}$  has obviously wide area absorption around 900 nm (NIR region) which is clearly visible from **Figure 4. 4A**, where the commercially available photocatalyst, Degussa- P25 has a wavelength cut-off around 390 nm. The corresponding band gap energy was calculated using Tauc plot (**Figure 4. 4B**) and the band gap energy values were obtained 3.26 and 1.51 eV respectively for Degussa-P25 and BAT. As evident from Tauc plot this synthetic strategy provides substantial decrement in band gap energy leading towards the rapid photo excitation of electron from VB to CB that could efficiently enhance the rate of photocatalysis.

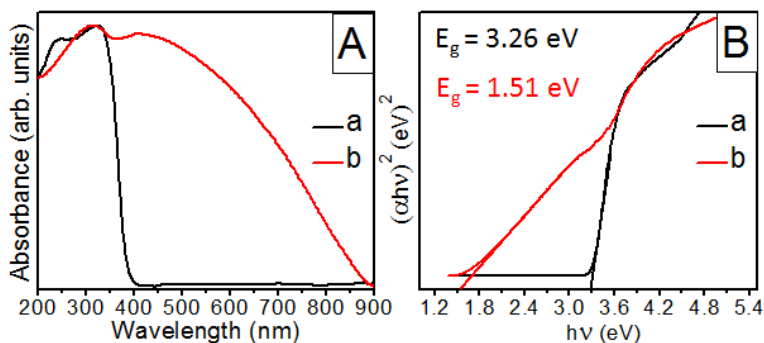


**Figure 4. 4. A) UV-Visible absorption spectra and B) Tauc plot of a) Degussa-P25 and b) BAT.**

#### 4. 2. 7. Photocatalysis

Methylene blue (MB) has been extensively used as photocatalytic model system at different concentration levels under different light irradiation source such as AM 1.5 G filter and Xe lamp (300 W) with a UV cut-off filter ( $\lambda \geq 420$  nm).<sup>2,25</sup> According Zhu *et al.* only 50% of degradation was occurred by using 10 mg/L MB model system (100 mL) and 100 mg Ti<sup>3+</sup> black TiO<sub>2</sub>.<sup>26</sup> The N<sub>2</sub> gas flow treated Ti<sup>3+</sup> self-doped anatase TiO<sub>2-x</sub> prepared by NaBH<sub>4</sub> reduction have shown photodegradation within 30 minute time by dispersing 20 mg of photocatalyst into 100 ml of methylene blue solution (20 mg/L).<sup>25</sup> Shah *et al.* reported MB degradation within 120 minutes under 300 W Xe lamp (Cut-off filter > 420 nm).<sup>9</sup> Leshuk *et al.* have successfully designed black TiO<sub>2</sub> by hydrogenation, however the degradation rate of MB was very low.<sup>27</sup> According to their report, from the degradation plot it was observed only a slight change in C/C<sub>0</sub> value from 1 to 0.92 confirmed almost zero activity towards the photodegradation of MB.<sup>27</sup>

The same group have also reported hydrogenated black anatase TiO<sub>2</sub> and the MB degradation was carried out by consuming nearly 150 minutes under AM 1.5 G filter.<sup>2</sup> Lately we have developed an oxygen vacancy rich black anatase TiO<sub>2</sub> for MB degradation under direct sunlight having 50K-70K lux intensity, where four fold more photoactivity than Degussa-P25 was observed.<sup>10</sup> This direct sunlight irradiation method has been earlier employed for self-healing also.<sup>28</sup> We have followed here the similar strategy (under direct sunlight) for the photocatalytic examination since the universal energy source sun can only transmit the maximum light energy with all magnitude of wavelengths.

The photocatalytic activities of BAT and standard Degussa-P25 were evaluated and the decomposition plot of methylene blue (MB) under solar illumination are shown in **Figure 4. 5**. The photocatalytic activity of BAT was higher than the commercially available photocatalyst Degussa-P25. For BAT the photodegradation was completed within 12 min, whereas Degussa-P25 has taken more than 18 minutes for the same process (**Figure 4. 5A, 4. 5B & 4. 5C**). In both the photocatalytic processes the characteristic monomer peak of MB was blue shifted owing to N-demethylation.<sup>29</sup>

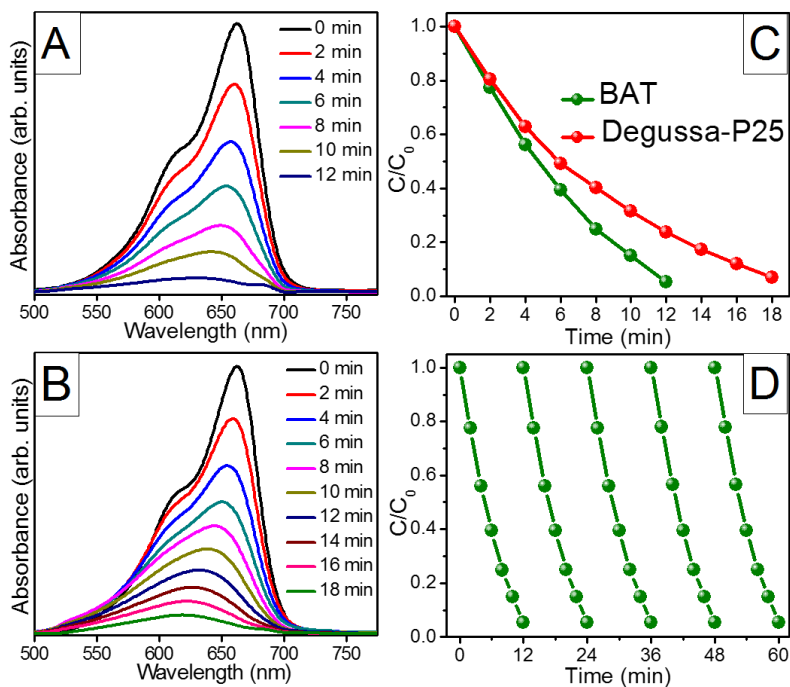


**Figure 4. 5. UV-Visible absorption spectra of methylene blue (MB) photodegradation using A) BAT and B) Degussa-P25. C) MB Degradation plot of BAT and Degussa-P25, D) MB degradation recycling efficiency for five consecutive runs using BAT.**

Retention of photocatalytic activity in five consecutive cycles were also obtained for BAT (**Figure 4. 5D**). During the solar illumination, the surface oxygen vacancy sites restrain the possibility of electron-hole recombination can be explained as follows. Since the band gap energy is very low for BAT the possibility for returning back of electron to the hole is very high. When the electron tend to do so, the surface oxygen vacancy sites trap the electrons and keep the hole to

electron spacing in an agreeable combination for efficient photocatalysis.

### 4. 3. Conclusions

A one pot gel combustion strategy towards  $\text{Ti}^{3+}$  self-doped, black anatase  $\text{TiO}_{2-x}$  has been developed. The defective anatase  $\text{TiO}_2$  nanocrystals were comprised of enormous  $\text{Ti}^{3+}$  and oxygen vacancy sites which are considered as the key players for photocatalysis. As synthesized black  $\text{TiO}_{2-x}$  was employed as photocatalyst using methylene blue dye as model system under the universal energy source sunlight. It was demonstrated that the black anatase  $\text{TiO}_2$  was 33% more photoactive than the commercially available photocatalyst Degussa-P25. In addition, this facile route gives an insight to implement the easily synthesized black anatase  $\text{TiO}_{2-x}$  in several applications such as in dye sensitized solar cells, water splitting, Li ion batteries. These NIR absorbing glycolated  $\text{TiO}_2$  nanostructures may be successfully used as a photothermal agent in cancer photothermal therapy and in further biomedical applications.

### References

1. X. Chen, L. Liu, Y. Y. Peter and S. S. Mao, *Science*, 2011, **331**, 746.
2. T. Leshuk, R. Parviz, P. Everett, H. Krishnakumar, R. A. Varin and F. Gu, *ACS Appl. Mater. Interfaces*, 2013, **5**, 1892.
3. Y. Zhu, D. Liu and M. Meng, *Chem. Commun.*, 2014, **50**, 6049.

4. S. T. Myung, M. Kikuchi, C. S. Yoon, H. Yashiro, S. J. Kim, Y. K. Sun and B. Scrosati, *Energy Environ. Sci.*, 2013, **6**, 2609.
5. Z. Wang, C. Yang, T. Lin, H. Yin, P. Chen, D. Wan, F. Xu, F. Huang, J. Lin, X. Xie and M. Jiang, *Energy Environ. Sci.*, 2013, **6**, 3007.
6. Z. Zhao, H. Tan, H. Zhao, Y. Lv, L. J. Zhou, Y. Song and Z. Sun, *Chem. Commun.*, 2014, **50**, 2755.
7. A. Sinhamahapatra, J. P. Jeon and J. S. Yu, *Energy Environ. Sci.*, 2015, **8**, 3539.
8. J. Dong, J. Han, Y. Liu, A. Nakajima, S. Matsushita, S. Wei and W. Gao, *ACS Appl. Mater. Interfaces*, 2014, **6**, 1385.
9. M. W. Shah, Y. Zhu, X. Fan, J. Zhao, Y. Li, S. Asim and C. Wang, *Sci. Rep.*, 2015, **5**, 15804.
10. S. G. Ullattil and P. Periyat, *Nanoscale*, 2015, **7**, 19184.
11. T. V. Anuradha and S. Ranganathan, *Bull. Mater. Sci.*, 2007, **30**, 263.
12. L. R. Grabstanowicz, S. Gao, T. Li, R. M. Rickard, T. Rajh, D. J. Liu and T. Xu, *Inorg. Chem.*, 2013, **52**, 3884.
13. W. Ren, Y. Yan, L. Zeng, Z. Shi, A. Gong, P. Schaaf, D. Wang, J. Zhao, B. Zou, H. Yu, G. Chen, E. M. B. Brown and A. Wu, *Adv. Healthcare Mater.*, 2015, **4**, 1526.

14. U. Zavyalova, B. Nigrovski, K. Pollok, F. Langenhorst, B. Müller, P. Scholz and B. Ondruschka, *Appl. Catal. B: Environ.*, 2008, **83**, 221.
15. S. C. Pillai, P. Periyat, R. George, D. E. McCormack, M. K. Seery, H. Hayden and S. J. Hinder, *J. Phys. Chem. C*, 2007, **111**, 1605.
16. R. Nakamura, A. Imanishi, K. Murakoshi and Y. Nakato, *J. Am. Chem. Soc.*, 2003, **125**, 7443.
17. R. Nakamura and Y. Nakato, *J. Am. Chem. Soc.*, 2004, **126**, 1290.
18. Z. Lu, C. T. Yip, L. Wang, H. Huang and L. Zhou, *ChemPlusChem*, 2012, **77**, 991.
19. S. Rtimi, J. Nestic, C. Pulgarin, R. Sanjines, M. Bensimon and J. Kiwi, *Interface focus*, 2015, **5**, 20140046.
20. R. Ren, Z. Wen, S. Cui, Y. Hou, X. Guo and J. Chen, *Sci. Rep.*, 2015, **5**, 10714.
21. P. V. R. K. Ramacharyulu, D. B. Nimbalkar, J. P. Kumar, G. K. Prasad and S. C. Ke, *RSC Adv.*, 2015, **5**, 37096.
22. C. Fan, C. Chen, J. Wang, X. Fu, Z. Ren, G. Qian and Z. Wang, *Sci. Rep.*, 2015, **5**, 11712.

23. A. Naldoni, M. Allieta, S. Santangelo, M. Marelli, F. Fabbri, S. Cappelli, C. L. Bianchi, R. Psaro and V. D. Santo, *J. Am. Chem. Soc.*, 2012, **134**, 7600.
24. X. Chen, D. Zhao, K. Liu, C. Wang, L. Liu, B. Li, Z. Zhang and D. Shen, *ACS Appl. Mater. Interfaces*, 2015, **7**, 16070.
25. X. Xin, T. Xu, J. Yin, L. Wang and C. Wang, *Appl. Catal. B: Environ.*, 2015, **176**, 354.
26. G. Zhu, T. Lin, X. Lü, W. Zhao, C. Yang, Z. Wang, H. Yin, Z. Liu, F. Huang and J. Lin, *J. Mater. Chem. A*, 2013, **1**, 9650.
27. T. Leshuk, S. Linley and F. Gu, *Can. J. Chem. Eng.*, 2013, **91**, 799.
28. S. Thakur and N. Karak, *J. Mater. Chem. A*, 2015, **3**, 12334.
29. D. P. DePuccio, P. Botella, B. O'Rourke and C. C. Landry, *ACS Appl. Mater. Interfaces*, 2015, **7**, 1987.

# 5 Chapter

## Solution Processed, Oxygen Deficient ZnO Microrods for Solar Photocatalysis

### Contents

- 5. 1. Introduction
- 5. 2. Results and Discussion
- 5. 3. Conclusions  
References

### 5. 1. Introduction

ZnO is a semiconductor with wide band gap energy (3.37 eV) similar to TiO<sub>2</sub> (3.2 eV), which means the wavelength of absorption is low ( $\lambda < 380$  nm) and hence the lower photocatalytic efficiency under UV region. Thus visible light absorbing ZnO particles of narrowed band gap energy are under investigation by the scientific world that can facilitate effective photocatalysis. Generally the band gap narrowing for visible light absorption is introduced on ZnO by doping with metals or non metals.<sup>1,2,3,4</sup> Doping with metal may cause the formation of secondary impurities and leads to decrease in photoactivity.<sup>1</sup> Also the addition of such impurity elements (metals and non metals) are not economical and the need of expensive solvents for washing procedure to remove byproducts keeps it away from cost-effectiveness. In this direction there are a few ZnO fabrication techniques have been

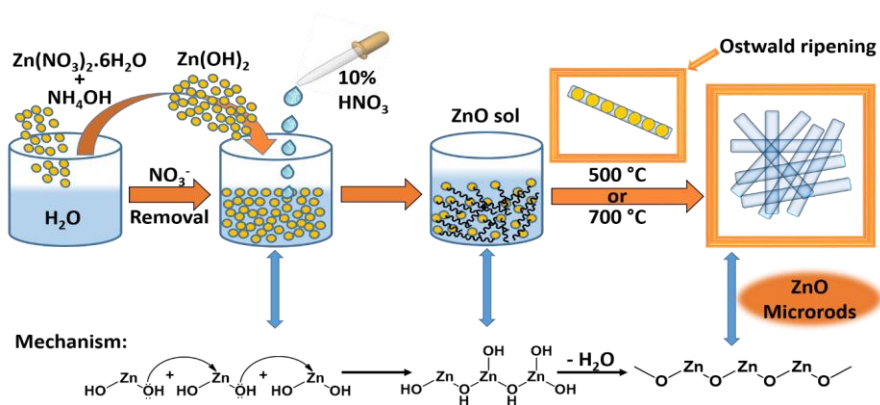
proposed to incorporate oxygen deficient sites and thus by decreasing band gap energy towards a higher photocatalytic performance such as vacuum deoxidation,<sup>2</sup> ball milling,<sup>3</sup> cold plasma treatment<sup>4</sup> and electrospinning.<sup>5</sup> The present work is devoted to a temperature controlled synthesis of dopant free solar ZnO photocatalysts through a solution processing strategy that holds high temperature stable oxygen vacancy sites and narrowed band gap energy of ZnO. Here the oxygen vacancy richness is found as a kind of self-doping mechanism in ZnO without introducing any impurity element. Moreover these temperature driven ZnO nanocrystals are firmly rigid in their oxygen vacancy richness even at 900 °C which led them to an extremely narrowed band gap energy in the range 3.05- 3.09 eV, is a new invention to date. As prepared ZnO photocatalysts were systematically inspected using methylene blue dye solution as model system both under UV and natural sunlight illumination.

## **5. 2. Results and Discussion**

### **5. 2. 1. Synthetic Mechanism**

ZnO nanocrystals were prepared by a solution processing route in which zinc (II) nitrate hexahydrate was first converted to zinc (II) hydroxide by reacting with ammonium hydroxide. Conversion to ZnO was completed by heat treatment of zinc (II) hydroxide at higher temperature 300, 500, 700, 800 and 900 °C in presence of oxygen. The ZnO precursor obtained were with irregular shape and after calcination at 300 °C, the nanocrystalline ZnO were formed with no specific shape. Whereas, when the calcination was carried out at 500 °C the

ZnO microrod were formed and the rod morphology was retained after 700 °C calcination. At 800 and 900 °C the rod shape has been lost and the aforementioned observations are evident from SEM images (**Figure 5. 1**). Padmanabhan *et al.* used  $\text{Zn}(\text{NO}_3)_2 \cdot 6\text{H}_2\text{O}$  and ammonium carbamate as precursors for the synthesis of ZnO micro rods using microwave method.<sup>6</sup> The weakly basic condition leads to the orientation of ZnO along c-axis and the morphology can be changed (micro-spheres  $\rightarrow$  micro-rods  $\rightarrow$  micro-javelins) by adjusting the time intervals of microwave power.<sup>6</sup>



**Scheme 5. 1. Growth Mechanism of ZnO microrods with proposed mechanism of the formation of ZnO network.**

Growth mechanism of ZnO microrod in the present work is described in the **Scheme 5. 1**. As described in the scheme  $\text{Zn}(\text{NO}_3)_2 \cdot 6\text{H}_2\text{O}$  was used to ensure the increased OH concentration, which can lead to rod like morphology by ensuring the sufficient growth rate along (001) direction.<sup>7</sup> The persistence of surface adsorbed water even after the heat treatment, accelerate the growth and ripening rate in one dimensional fashion leading to the formation of ZnO rods.<sup>7</sup>

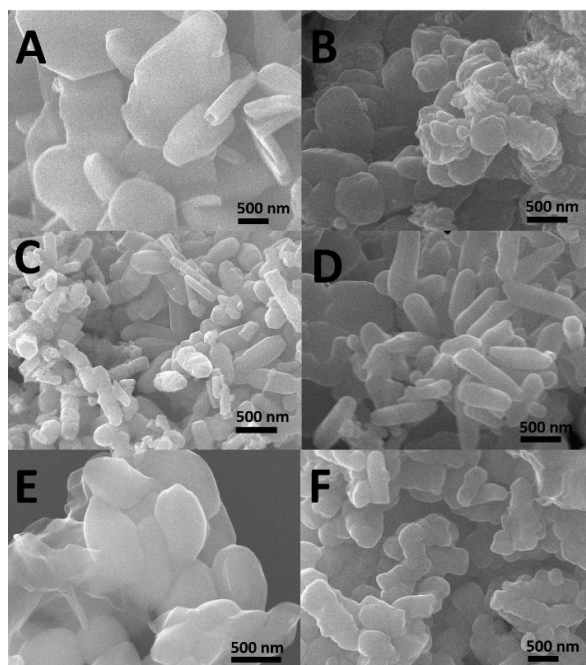


**Figure 5. 1.** SEM images of A) ZnO precursor B) ZnO-300 C) ZnO-500 and D) ZnO-700 E) ZnO-800 and F) ZnO-900.

### 5. 2. 2. SEM Analysis

Surface morphological studies of all calcined ZnO samples were done using Scanning electron Microscope (SEM) are shown in **Figure 5. 1**. The SEM analysis showed that, except the less crystalline ZnO precursor and ZnO-300, other samples (ZnO-500 and ZnO-700) are rod shaped (**Figure 5. 1**). The rod morphology has been lost after calcination at 800 and 900 °C (ZnO-800 and ZnO-900).

### 5. 2. 3. X-ray Diffraction (XRD)

The XRD patterns of ZnO-300, ZnO-500, ZnO-700, ZnO-800 and ZnO-900 (**Figure 5. 2**) have shown high phase purity of ZnO samples and they are in correct agreement with the typical wurtzite ZnO

structure (JCPDS-01-036-1451). However, the XRD pattern of ZnO precursor contain peaks that can be assigned to  $\text{Zn}(\text{NO}_3)_2$  and  $\text{Zn}(\text{OH})_2$  along with a small percentage of  $\text{ZnO}^8$  (**Figure 5. 3**). The average crystallite sizes of ZnO calcined at different temperatures calculated using Sherrer equation were around  $40 \pm 5$  nm revealed the nanocrystalline nature of ZnO that have been synthesized. The enlarged XRD patterns of ZnO major peaks are shown inset and it is clear from figure that the peak shift occurred as the temperature changes from 300 to 900 °C. It is due to variation in residual strain within the crystal lattice.<sup>9</sup> As the temperature changes from 300 to 900 °C the lattice strain varies and thereby the compressive strain is shuttling along (101) direction.<sup>10</sup> In particular as the temperature varies, strain will vary inhomogeneously, hence different crystallites will be strained by different amounts and correspondingly the shifts in  $2\theta$  will also vary.<sup>10</sup>

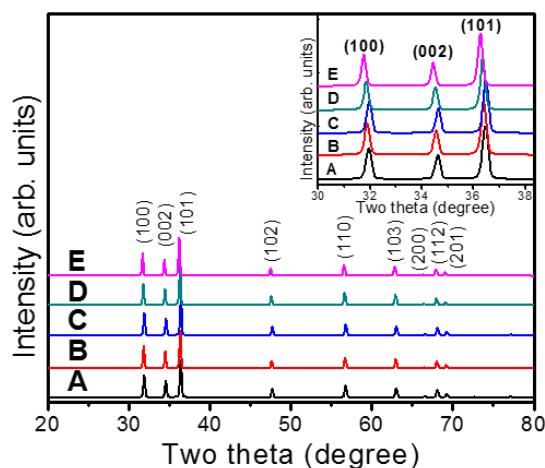


**Figure 5. 2.** XRD spectra of A) ZnO-300 B) ZnO-500 C) ZnO-700 D) ZnO-800 and E) ZnO-900 (Inset presents the shifting of major peaks).

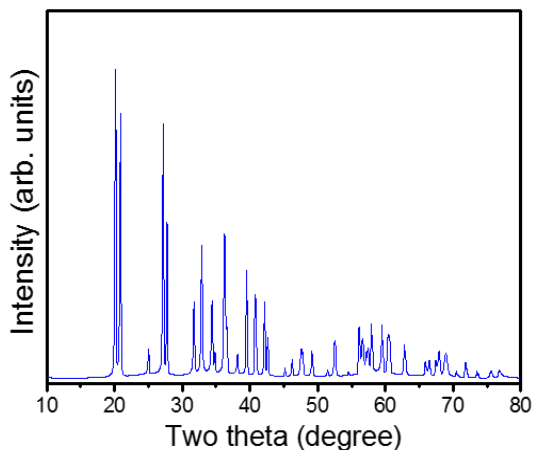


**Figure 5. 3. XRD pattern of the ZnO precursor.**

#### **5. 2. 4. FTIR and Raman Spectroscopy**

The formation of ZnO wurtzite structure was further confirmed by FT-IR and Raman spectral analysis. The IR spectrum of ZnO precursor (**Figure 5. 4**) has shown a very broad band in the range 3000-3500  $\text{cm}^{-1}$  as compared to the calcined samples.<sup>1,3</sup> It is due to the N-H stretching vibration at  $\sim 3250 \text{ cm}^{-1}$  present along with O-H stretching ( $\sim 3450 \text{ cm}^{-1}$ ) in the ZnO precursor. The N-H stretching arises due to the presence of ammonium hydroxide weakly bound to ZnO. As shown in **Figure 5. 5A**, after calcination at high temperatures, the peak of N-H vibration was disappeared and the band at  $\sim 3450 \text{ cm}^{-1}$  is alone visible. This band corresponds to the O-H stretching arising from -OH groups bound to the ZnO or surface adsorbed water molecules and the peak at  $1630 \text{ cm}^{-1}$  could be assigned to O-H bending.<sup>11</sup> These spectral features indicate that zinc hydroxide has been formed by the reaction between zinc nitrate and ammonium hydroxide. The peak at  $1383 \text{ cm}^{-1}$

is attributed to the surface adsorbed CO<sub>2</sub> molecules on ZnO.<sup>11</sup> Only for ZnO-300, ZnO-500 and ZnO-700 samples a band at 1020 cm<sup>-1</sup> is present, which is the threshold frequency band representing the activation energy for electronic conduction.<sup>12</sup> This threshold energy may direct towards the high photocatalytic efficiency of these three ZnO nanocrystals samples as compared to ZnO-800 and ZnO-900. For ZnO-700, ZnO-800 and ZnO-900, the absorptions corresponding to water, hydroxyl and N-H vibrations are no longer present and only visible a strong Zn-O-Zn band at ~450 cm<sup>-1</sup> which is the characteristic peak of nanocrystalline ZnO.<sup>12</sup> However ZnO-500 projecting its identity on account of the most intense Zn-O-Zn and O-H stretching bands. These features would have positively contributed to its higher photoactivity. For ZnO-900 having a weak Zn-O-Zn band have shown the least photocatalytic activity under UV/sunlight illumination and it is evident from the photocatalytic measurements (Section 3.7).

Raman active phonons of wurtzite ZnO have C<sub>6v</sub> symmetry and according to group theory A<sub>1</sub>+2B<sub>1</sub>+E<sub>1</sub>+2E<sub>2</sub> are the Raman active phonons where B<sub>1</sub> (low) and B<sub>1</sub> (high) are silent normally. Except E<sub>2</sub>, both A<sub>1</sub> and E<sub>1</sub> are Raman active as well as IR active. E<sub>2</sub> is a non-polar phonon mode with two frequencies, E<sub>2</sub> (high) and E<sub>2</sub> (low) ascribed to oxygen atoms and Zn respectively. Both A<sub>1</sub> and E<sub>1</sub> experience, frequencies for transverse optical (TO) and longitudinal optical (LO) since they are polar phonon modes. The dominant peak at 435 cm<sup>-1</sup> corresponds to the wurtzite characteristic E<sub>2</sub> (high) vibration mode with orientation along c-axis. A second order forbidden frequency mode at 330 cm<sup>-1</sup> is described by E<sub>2</sub>-E<sub>1</sub> (low) phonons and the defect

induced peak at  $580\text{ cm}^{-1}$  could be assigned to the  $A_1(\text{LO})$  and  $E_1(\text{LO})$  vibration mode indicate the presence of oxygen vacancies.<sup>13</sup>

From **Figure 5. 5B**, all the calcined ZnO samples have demonstrated an intense peak at  $435\text{ cm}^{-1}$ , the characteristic of wurtzite phase of ZnO. The maximum intense peak at  $580\text{ cm}^{-1}$  was obtained for the ZnO-500 (**Figure 5. 5B. b**) indicating the presence of higher number of oxygen vacancy sites in the ZnO-500 sample compared to other calcined samples. In Raman spectra of ZnO, peak at  $560\text{ cm}^{-1}$  generally attributed to the existence of Zn interstitial ( $\text{Zn}_i$ ) sites.<sup>3</sup> The peaks at  $377$  and  $405\text{ cm}^{-1}$  owing to  $A_1(\text{TO})$  and  $E_1(\text{TO})$  vibration modes, which are the characteristics of structural or doping induced disorder.<sup>3</sup> Here all the calcined ZnO samples showed no peak at  $560\text{ cm}^{-1}$  confirms the absence of Zn interstitial ( $\text{Zn}_i$ ) sites, whereas the peaks at  $377$  and  $405\text{ cm}^{-1}$  with low intensity indicate the structural induced disorder present in all the calcined ZnO samples.<sup>3</sup>

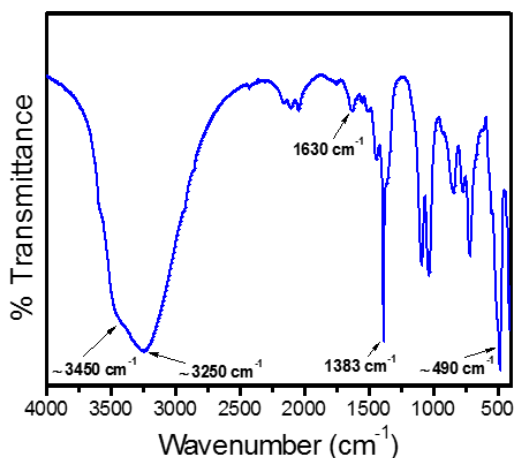


**Figure 5. 4.** FTIR spectrum of the ZnO precursor.

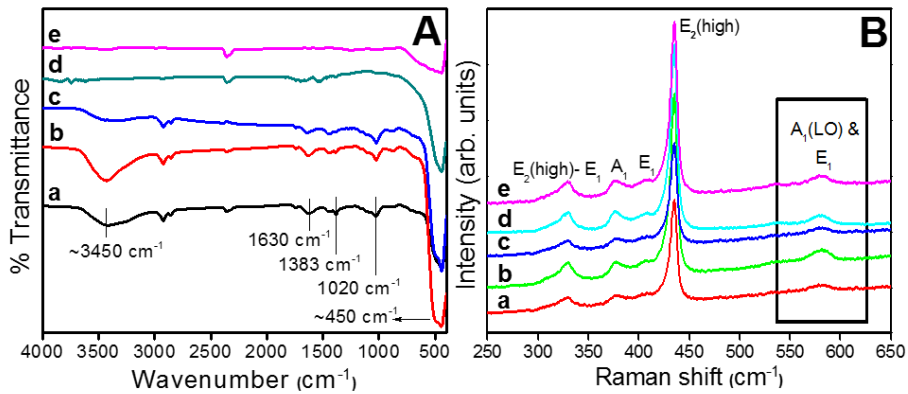


**Figure 5.5. A) FTIR and B) Raman spectra of a) ZnO-300 b) ZnO-500 c) ZnO-700 d) ZnO-800 and e) ZnO-900 (The oxygen vacancy defect vibration mode is highlighted in figure 5.5B).**

### 5.2.5. Photoluminescence (PL) Spectroscopy

For further confirmation of defects present in the ZnO lattice PL spectroscopy was also been carried out. From PL spectra (**Figure 5.6**) the peaks at 420, 459, 483 and 530 nm are clearly visible. The emission at 420 nm is attributed to the lattice defects related to oxygen vacancies ( $V_o$ ) and interstitial oxygen ( $O_i$ ).<sup>3</sup> This violet emission band at 420 nm may also be due to the interface traps existing between the ZnO-ZnO grain boundaries *i.e.* it should be emitted from the radiative transition between interface traps and the valence band.<sup>14</sup> The absence of emission at 438 nm eliminates the possibility of Zn interstitial, which was the earlier observation using Raman spectra (**Figure 5.5B**) is confirmed here. The green yellow emission band at 459 nm is originating from the lattice oxygen vacancies and the 483 nm emission associated with the transition between  $V_o$  and  $O_i$ , reveals the existence of oxygen interstitial.<sup>3</sup> The green emission at 530 nm is also ascribed

to oxygen vacancies<sup>14</sup> whereas no noticeable green emission at 530 nm is observed for ZnO-300 rather than an emission broadening around 550 nm indicating the capture of holes by singly ionized oxygen vacancy to generate doubly ionized surface defect states.<sup>14</sup>

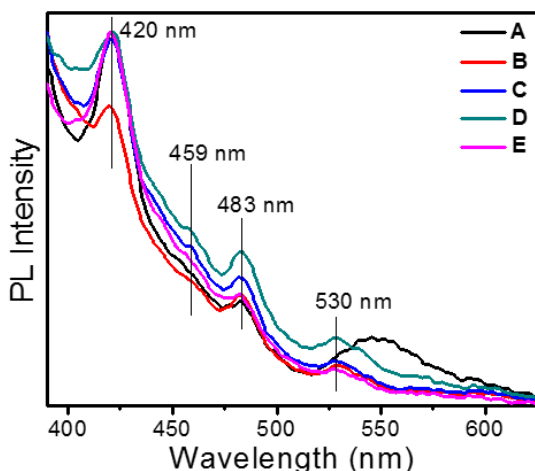


**Figure 5. 6. PL spectra of A) ZnO-300 B) ZnO-500 C) ZnO-700 D) ZnO-800 and E) ZnO-900.**

### **5. 2. 6. UV-Visible absorption spectroscopy & Tauc Plot**

The absorption spectrum of all ZnO samples shows vast area absorption bands beyond the UV region. From **Figure 5. 7A** it is evident that unlike the conventional ZnO, these oxygen vacancy rich ZnO samples extended their absorption from UV to visible region even at higher temperature 900 °C. With increase in temperature, ZnO absorption wavelength is increased and maximum cut off wavelength is obtained as 480 nm for ZnO-900. The ZnO-300 appears as pale yellow in color. As the temperature increases from 300 to 900 °C, color of the ZnO sample changes from pale yellow to yellow (**Figure 5. 8**)

indicating the self-doping of ZnO and higher visible light absorption. The band gap energies of all calcined ZnO samples were calculated from Tauc plot (**Figure 5. 7B**) are given in **Table 5. 1**. From **Figure 5. 7** and **Table 5. 1** it is clear that band gap energy of these ZnO samples, lies in the narrower range 3.05 – 3.09 eV. XRD (**Figure 5. 2**) confirms that there is presence of strain leading to the change in  $2\theta$  value. This compressive strain is obviously due to lattice defects and here it is predominantly due to oxygen vacancy defects confirmed by PL and Raman spectroscopy. Thus the defect states paved the way to yellow color of the calcined ZnO materials and they have shown visible region absorption which has directed towards band gap reduction.

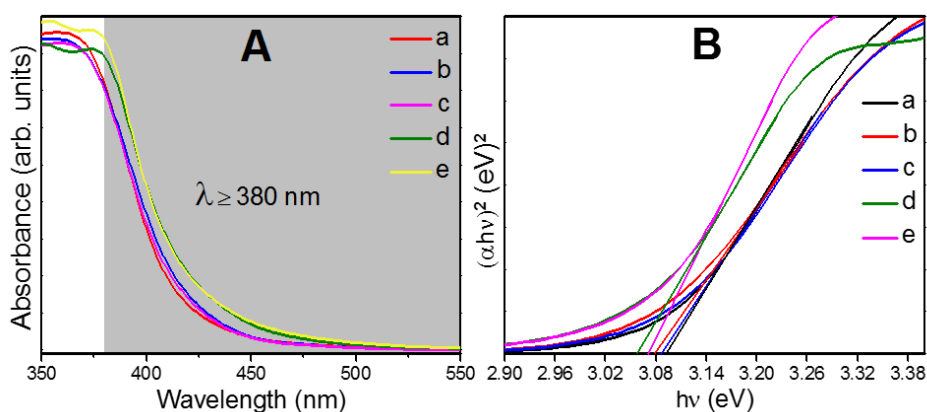


**Figure 5. 7. A) Absorption spectra and B) Tauc plot of a) ZnO-300 b) ZnO-500 c) ZnO-700 d) ZnO-800 and e) ZnO-900.**

**Table 5. 1. Band gap energy of ZnO samples**

<b>Sample</b>	<b>Band gap energy (eV)</b>
ZnO-300	3.09
ZnO-500	3.08
ZnO-700	3.09
ZnO-800	3.05
ZnO-900	3.07

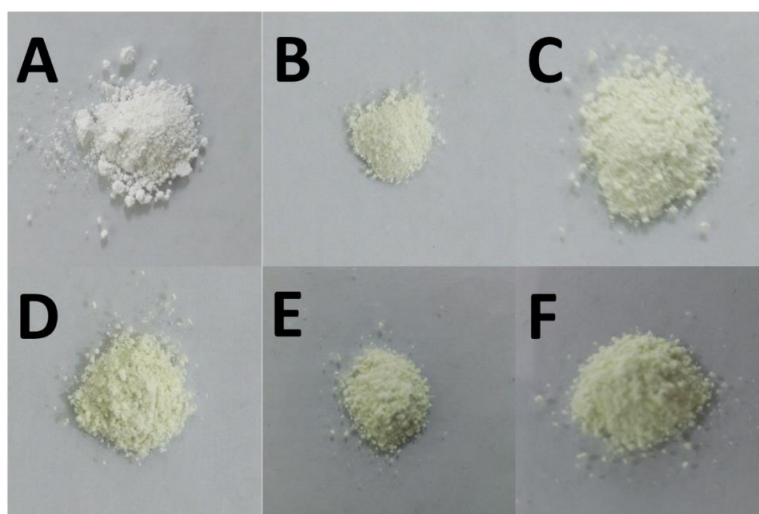


**Figure 5. 8. Photographs of A) ZnO precursor B) ZnO-300 C) ZnO-500 D) ZnO-700 E) ZnO-800 F) ZnO-900.**

### **5. 2. 7. Photocatalysis**

Photocatalytic studies of ZnO precursor and all calcined ZnO (300 to 900 °C) samples were carried out using methylene blue dye as a model system. In order to compare the photocatalytic efficiency of as synthesized ZnO samples, similar experiments were also carried out

using standard Degussa-P25 under the same conditions. The degradation was easily followed by decolorization of the dye solution using UV-Visible spectroscopy. The absorbance spectra as a function of time for the degradation of dye solution under both UV and natural sunlight were shown in **Figure 5. 9** and **5. 10** respectively. The photocatalysis follow first order kinetics which displayed inset of **Figure 5. 9** and **5. 10**.

From Figure it can be seen that all the ZnO nanocrystals are extraordinary platform for photocatalysis. In all the photocatalytic processes the major absorption peak of methylene blue at 662 nm were blue shifted in the absorption spectrum owing to N-demethylation of the dye solution.<sup>15</sup> While looking into UV assisted photodegradation (**Figure 5. 10**), the photocatalytic activity of Degussa- P25 was slightly higher as compared to ZnO photocatalysts and the order of photocatalytic efficiency is found to be Degussa-P25 > ZnO-300 > ZnO-700 > ZnO-800 > ZnO-500 > ZnO-900. The higher activity of Degussa-P25 under UV light is well studied and is mainly due to its wide absorption ability in the UV region and it contains a mixed phase (75% anatase and 25% rutile) with a high BET surface area around 45 m<sup>2</sup>/g. All these factors would have contributed towards the higher activity of Degussa-P25 under UV irradiation.<sup>16,17,18</sup>

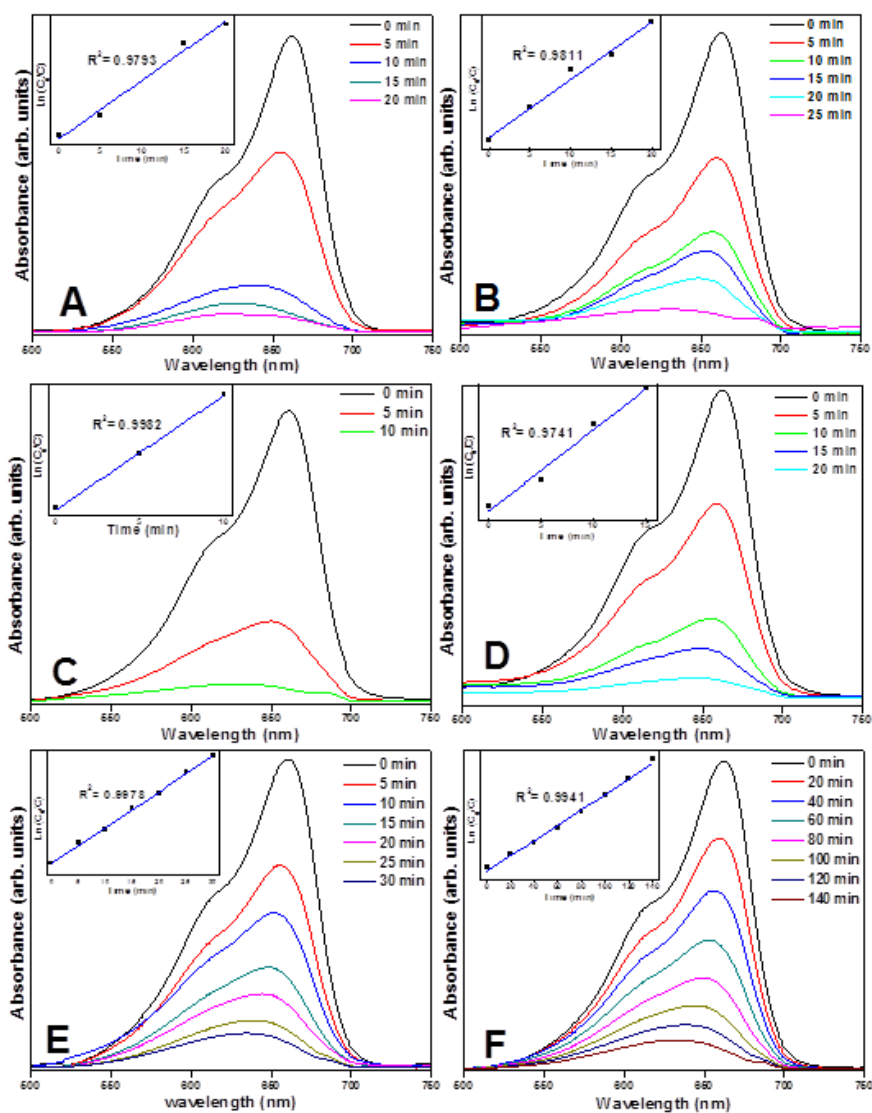


**Figure 5. 9. UV-Vis spectra of degradation of methylene blue by A) Degussa-P25 B) ZnO-300 C) ZnO-500 D) ZnO-700 E) ZnO-800 and F) ZnO-900 in presence of natural sunlight (kinetic plots are shown inset).**

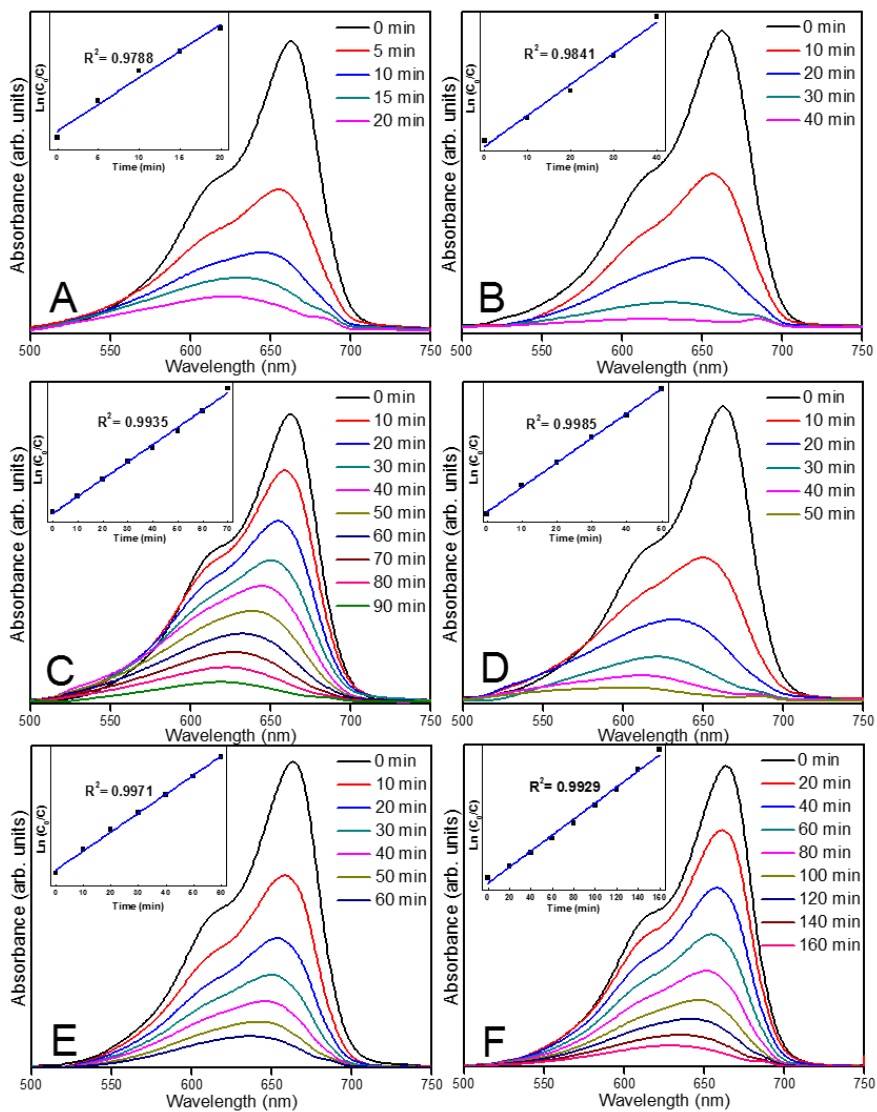


**Figure 5.10. UV-Vis spectra of degradation of methylene blue by A) Degussa-P25 B) ZnO-300 C) ZnO-500 D) ZnO-700 E) ZnO-800 and F) ZnO-900 under UV illumination (kinetic plots are shown inset).**

**Figure 5. 11** indicates the degradation of dye using Degussa-P25 and ZnO samples in presence of sunlight. In presence of sunlight, degradation follows the order ZnO-500 > ZnO-700 > Degussa-P25 > ZnO-300 > ZnO-800 > ZnO-900. The maximum photoactivity was observed in the case of ZnO-500 having the lowest band gap energy of 3.08 eV, which is twice active than that of standard Degussa-P25. The ZnO-500 took only 10 minutes for dye degradation whereas Degussa-P25 have taken 20 minutes.

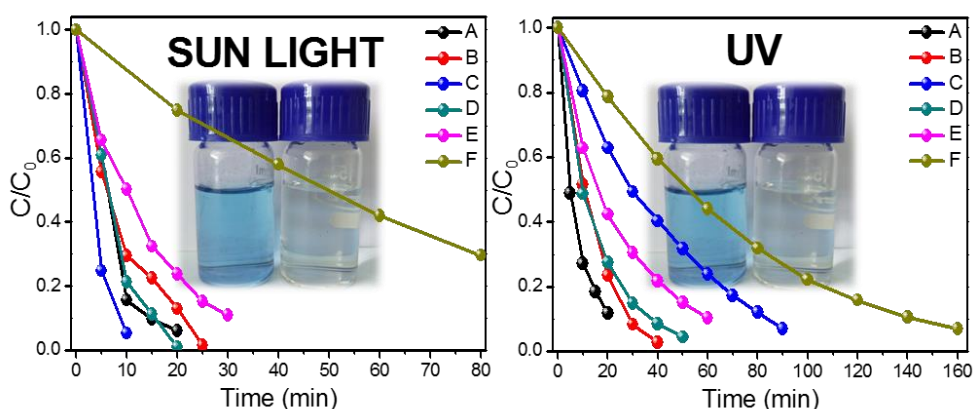


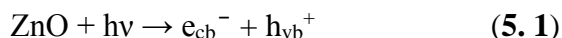
**Figure 5. 11. Photodegradation of methylene blue under natural sunlight and UV illumination using A) Degussa-P25 B) ZnO-300 C) ZnO-500 D) ZnO-700 E) ZnO-800 and F) ZnO-900.**

The higher solar photocatalytic activity of ZnO-500 and ZnO-700 than standard Degussa-P25 can be explained as follows. It is already reported that, with the increase in oxygen deficiency a drastic increase in photocatalytic performance can be introduced.<sup>19,20</sup> The band gap energy of these samples are in the range of 3.05-3.09 eV which corresponds to visible light region in the electromagnetic spectrum. This narrower range of narrowed band gap energy along with increase

in oxygen deficiency of as synthesized ZnO samples facilitated a peculiar way to show higher photocatalytic efficiency. The band gap narrowing in ZnO samples are undoubtedly due to the excess oxygen vacancies (which is evident from Raman spectra, **Figure 5. 5B**) as a kind of self-doping mechanism present in the lattice.<sup>21</sup> Also it is clear from Raman spectra that, since there is no dopant and the presence of Zn interstitials here, oxygen vacancy is the only key player that is responsible for band gap narrowing, hence higher visible light absorption and thus optimizing higher photocatalytic efficiency of ZnO samples. The maximum photocatalytic efficiency under sunlight was obtained for ZnO-500 (**Figure 5. 9**) which has relatively the maximum intense peak at  $580\text{ cm}^{-1}$  (**Figure 5. 5B**) further reveals the dependence of photocatalysis on oxygen vacancy concentration. Other samples such as ZnO-800 and ZnO-900 show lower photocatalytic activity. According to previous reports as the temperature increases ZnO loses its oxygen vacancy sites which led to noticeable shift of absorption peaks towards the lower absorption region, consequently an increment in band gap energy also occurs.<sup>19,20</sup> However, here the higher wavelength absorption is retained along with slightly low oxygen vacancies at high temperatures as compared to the most active photocatalyst ZnO-500. Moreover on account of the densification of these samples occurs at high temperatures, the microrod morphology was disappeared. All these factors have contributed towards the lower photocatalytic activity of ZnO-800 and ZnO-900. Also, the ZnO precursor has lower sunlight photocatalytic activity due to its poor visible light absorption and weak crystallinity.

### 5. 2. 8. Photocatalytic Reaction Mechanism

Generally a photocatalytic process commence with the photoexcitation of electrons from valence band to conduction band access to the generation of holes at the valence band. As a result an electron-hole separation arises as follows.



In defect free ZnO fast electron-hole recombination taking place. However, the recombination rate is reduced in defect rich ZnO. This is happening due to the presence of an electron acceptor, obviously here the surface oxygen vacancy sites ( $V_o$ ) of as synthesized ZnO sample that can trap the photogenerated electrons. These oxygen vacancy sites of ZnO samples are highly beneficial for restraining electron-hole recombination leading to the formation of  $O_2^{\cdot -}$  radical by reduction as shown below.



When the oxygen vacancy concentration is very high, the oxygen vacancy state will be above the valence band as a forbidden state as depicted in **Figure 5. 12**. Zheng *et al.*<sup>22</sup> have already reported that the separation efficiency of electron and hole is controlled by oxygen vacancies. Moreover some oxygen interstitials ( $O_i$ ) are also generated (which is evident from PL spectra, **Figure 5. 6**) in the as prepared ZnO samples during light absorption and temperature processing. These  $O_i$

combines with the hole generated at the valence band facilitate oxidation to  $\text{OH}^\bullet$  described by the following equations.



According to band bending approximation,<sup>60</sup> oxygen vacancies are believed to be more efficient in suppressing electron-hole recombination and thus exhibiting high photocatalytic efficiency<sup>23</sup> which is in correct agreement with the photocatalytic efficiency as shown in **Figure 5. 11**, where ZnO-500 shows maximum photocatalytic efficiency due to maximum oxygen vacancy sites present as compared to ZnO-300, ZnO-700, ZnO-800 and ZnO-900.

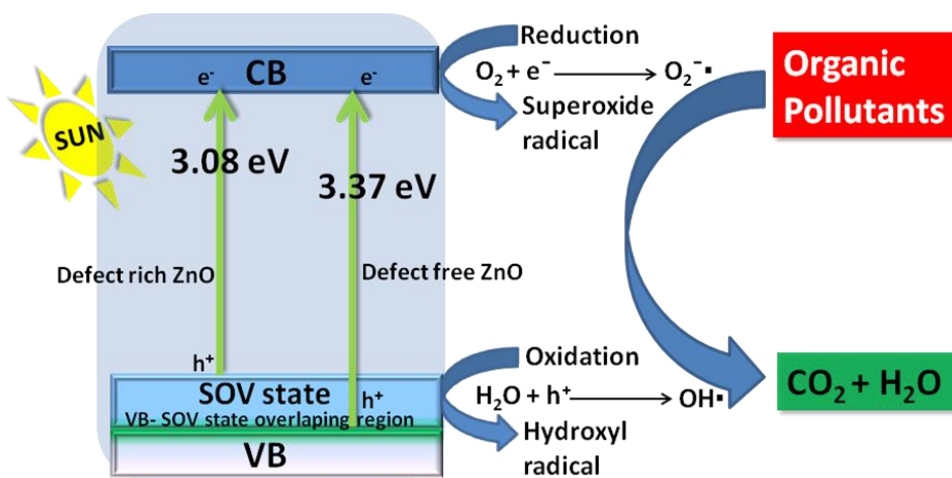


**Figure 5. 12. Photocatalysis mechanism of Oxygen deficiency enriched ZnO nanocrystals (VB: Valence band, CB: Conduction band, SOV state: Surface oxygen vacancy state).**

**Figure 5. 12** displays that the oxygen vacancy sites are occupied just above the valence band of ZnO nanocrystals as a kind of self-doping mechanism (ZnO-500 with band gap 3.08 eV is shown). Consequently the valence band and the oxygen vacancy state overlap together leads to the narrowing of band gap which is far less than the defect free ZnO (3.37 eV). Thus by utilizing the natural sunlight, electrons are excited from the high energy valence band to the conduction band easily results in the formation of  $O_2^{\cdot -}$  and  $OH^{\cdot}$  by reduction and oxidation respectively photocatalyzes the mineralization of organic dye pollutants into  $CO_2$  and  $H_2O$ .

### 5. 3. Conclusions

ZnO nanocrystals having narrowed band gap energy with rich oxygen vacancy sites were achieved by a facile and dopant free, solution processing method that has been designed only by using zinc nitrate hexahydrate, ammonium hydroxide and nitric acid. As synthesized ZnO nanocrystals have narrowed band gap energies in the range 3.05 – 3.09 eV which is due to the presence of excess oxygen vacancy sites in the crystal lattice and these vacancy sites are retained even after annealing at high temperature, 900 °C. These ZnO nanocrystals were successfully applied as photocatalysts under normal sunlight due to their extended substantial absorption ranges upto 480 nm. Rod shaped ZnO-500 and ZnO-700 with band gap energies 3.08 and 3.09 eV respectively have demonstrated greater photocatalytic efficiency than the commercially available photocatalyst Degussa-P25 which revealed the combined activity of morphology and oxygen deficiency character of ZnO. The Degussa-P25 has performed dye degradation by taking

more than 20 minutes while ZnO-500 and ZnO-700 have completed the same within 10 minutes and 20 minutes respectively. These high temperature stable solar active ZnO nanocrystals will unambiguously serve as remarkable photocatalysts and in future they may pave the way as a photocatalytic self-cleaner in ceramic tiles since its fabrication needs high temperature processing (~900 °C) along with light harvesting capability.

## References

1. R. Georgekutty, M. K. Seery and S. C. Pillai, *J. Phys. Chem. C*, 2008, 112, 13563.
2. Y. Lv, C. Pan, X. Ma, R. Zong, X. Bai and Y. Zhu, *Appl. Catal. B: Environ.*, 2013, **138**, 26.
3. D. Chen, Z. Wang, T. Ren, H. Ding, W. Yao, R. Zong and Y. Zhu, *J. Phys. Chem. C*, 2014, **118**, 15300.
4. Z. Pei, L. Ding, J. Hu, S. Weng, Z. Zheng, M. Huang and P. Liu, *Appl. Catal. B: Environ.*, 2013, **142**, 736.
5. M. Samadi, H. A. Shivaee, A. Pourjavadi and A. Z. Moshfegh, *Appl. Catal. A: Gen.*, 2013, **466**, 153.
6. S. C. Padmanabhan, D. Ledwith, S. C. Pillai, D. E. McCormack and J. M. Kelly, *J. Mater. Chem.*, 2009, **19**, 9250.
7. H. L. Cao, X. F. Qian, Q. Gong, W. M. Du, X. D. Ma and Z. K. Zhu, *Nanotechnol.*, 2006, **17**, 3632.

8. A. Pimentel, D. Nunes, P. Duarte, J. Rodrigues, F. M. Costa, T. Monteiro and E. Fortunato, *J. Phys. Chem. C*, 2014, **118**, 14629.
9. B. D. Cullity and S. R. Stock, "Elements of X-ray diffraction", 3rd Edit., Prentice Hall. 2001, *Chapter 4*, pp. 123.
10. S. A. Ansari, M. M. Khan, S. Kalathil, A. Nisar, J. Lee and M. H. Cho, *Nanoscale*, 2013, **5**, 9238. b) J. K. Cockcroft, P. Barnes and M. P. Attfield, Powder Diffraction on the Web, an Open Access Web Based Course. 2000, *chapter 15*, pp. 5.
11. X. L. Cheng, H. Zhao, L. H. Huo, S. Gao and J. G. Zhao, *Sensors Actuators B: Chem.*, 2004, **102**, 248.
12. V. R. Kumar, K. V. Narasimhulu, N. O. Gopal, H. K. Jung, R. P. S. Chakradhar and J. L. Rao, *J. Phys. Chem. Solids*, 2004, **65**, 1367.
13. T. Ngo-Duc, K. Singh, M. Meyyappan and M. M. Oye, *Nanotechnol.*, 2012, **23**, 194015.
14. B. J. Jin, S. Im and S. Y. Lee, *Thin Solid Films*, 2000, **366**, 107.
15. C. Yogi, K. Kojima, N. Wada, H. Tokumoto, T. Takai, T. Mizoguchi and H. Tamiaki, *Thin Solid Films*, 2008, **516**, 5881.
16. M. Keshmiri, T. Troczynski and M. Mohseni, *J. Hazard. Mater.*, 2006, **128**, 130.
17. V. Puddu, H. Choi, D. D. Dionysiou and G. L. Puma, *Appl. Catal. B: Environ.*, 2010, **94**, 211.

18. D. C. Hurum, A. G. Agrios, K. A. Gray, T. Rajh and M. C. Thurnauer, *J. Phys. Chem. B*, 2003, **107**, 4545.
19. J. Wang, Z. Wang, B. Huang, Y. Ma, Y. Liu, X. Qin and Y. Dai, *ACS Appl. Mater. Interfaces*, 2012, **4**, 4024.
20. Y. Tang, H. Zhou, K. Zhang, J. Ding, T. Fan and D. Zhang, *Chem. Eng. J.*, 2015, **262**, 260.
21. A. Janotti and C. G. Van de Walle, *J. Cryst. Growth*, 2006, **287**, 58.
22. Y. Zheng, C. Chen, Y. Zhan, X. Lin, Q. Zheng, K. Wei and Y. Zhu, *Inorg. Chem.*, 2007, **46**, 6675.
23. S. Mukhopadhyay, P. P. Das, S. Maity, P. Ghosh and P. S. Devi, *Appl. Catal. B: Environ.*, 2015, **165**, 128.

# 6 Chapter

## Microwave Power Induced TiO<sub>2</sub> Nanostructures for Efficient Dye Sensitized Solar Cells

### Contents

- 6. 1. Introduction
- 6. 2. Results and Discussion
- 6. 3. Conclusions
- References

### 6. 1. Introduction

Structurally different nano and micro sized TiO<sub>2</sub> nanostructures have been prepared and utilized for light harvesting in the area of visible light photocatalysis, water splitting and dye sensitized solar cells<sup>1-5</sup> using different synthetic strategies. The synthetic methods those have been used to prepare TiO<sub>2</sub> materials include sol-gel, microwave, hydrothermal, solvothermal, micelle, inverse micelle, chemical vapor deposition (CVD), physical vapor deposition (PVD), gel combustion and electrospinning.<sup>6-10</sup> Till date several reports are available for the synthesis of TiO<sub>2</sub> nanostructures such as spheres,<sup>11,12</sup> beads,<sup>13,14</sup> nanotubes,<sup>15</sup> nanorods,<sup>16</sup> nanosheets<sup>17</sup> and cuboid<sup>18</sup> morphologies with high structural orderliness for DSSC applications. However, in most of the previous reports, the conversion efficiencies were limited in the range 2-5%. Very recently TiO<sub>2</sub> blocking layers have been

implemented for improving the conversion efficiency.<sup>19-21</sup> Li *et al.* reported 5.38% conversion efficiency by inserting TiO<sub>2</sub> compact layer between ITO nanowires and porous TiO<sub>2</sub> shell.<sup>19</sup> Salvinelli *et al.*<sup>20</sup> reported an efficiency of 3.1% using sputtered TiO<sub>2</sub> blocking layer on Cd-Si oxide layer. By the similar technique it was reported that the efficiency can be achieved upto 4.9%<sup>21</sup> on ZnO: Al based DSSC. Keeping these facts in mind, our present work has devoted to develop anatase TiO<sub>2</sub> nanoparticles for DSSC application through a rapid microwave technique using low cost materials. This facile synthetic strategy using titanium butoxide, ethanol and deionized water as only precursors led the way to anatase TiO<sub>2</sub> nanoparticles and its application as a photoanode material in DSSC.

## 6. 2. Results and Discussion

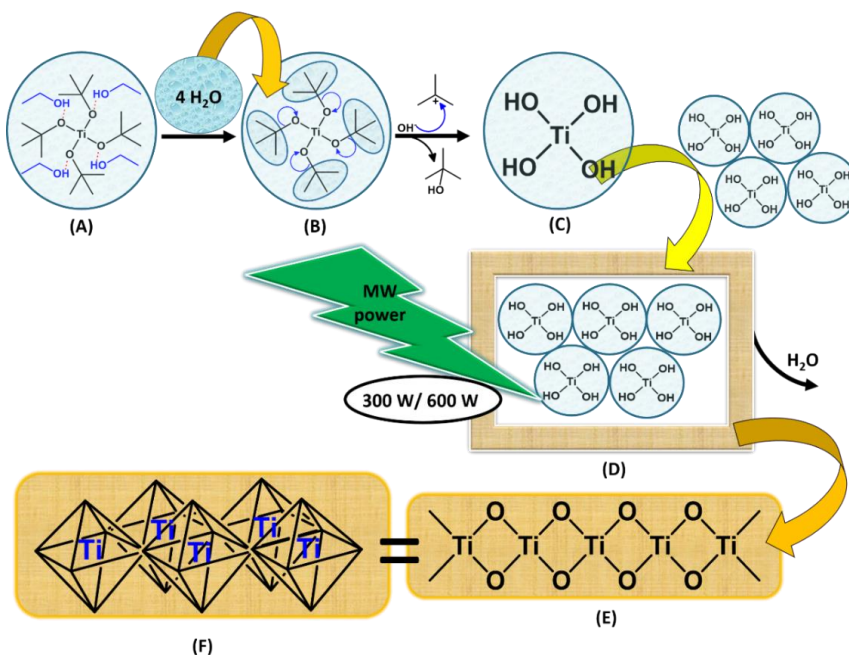
### 6. 2. 1. Growth mechanism of TiO<sub>2</sub> Nanonetwork

The overall synthesis of TiO<sub>2</sub> by the hydrolysis and condensation reactions by using titanium butoxide and water can be represented by the following **equations 6. 1** and **6. 2**.



Schematic representation for the formation of TiO<sub>2</sub> nanonetwork are shown in Scheme 6. 1. As shown in scheme, after the mixing ethanol and titanium butoxide (A), four water molecules are added to the system. While the water molecule enters in to the titanium butoxide system (B), tertiary (3°) carbocation is formed since it is highly stable.

The three electron donating –CH<sub>3</sub> groups donate electron to the highly electronegative oxygen atoms attached to titanium forming the tertiary (3°) carbocation. This carbocation is stabilized by the attack of OH<sup>-</sup> from water to the positively charged carbon atom forming tertiary butanol. Whereas the unstable tetra-positively charged oxo anion (TiO<sub>4</sub><sup>4+</sup>) accept 4 H<sup>+</sup> ions leading to the formation of Ti(OH)<sub>4</sub>, the titanium hydroxide (C). The same process carrying out in the whole system directing towards the propagation of titanium hydroxide molecules (D) by applying microwave power leads to a rally of condensation reactions heading to the formation of the anatase TiO<sub>2</sub> nano network (E and F). In **Scheme 6. 1**, (F) indicates the TiO<sub>6</sub> octahedra of anatase TiO<sub>2</sub> nano network which are edge shared.



**Scheme 6. 1.** The growth mechanism of anatase TiO<sub>2</sub> nanonetwork.

### 6. 2. 2. X ray Diffraction

XRD spectra of TiO<sub>2</sub> nanoparticles synthesized using microwave method is shown in **Figure 6. 1**. The sample showed amorphous characteristics before microwave irradiation (**Figure 6. 1a**). After microwave irradiation for 5 minutes, crystalline anatase TiO<sub>2</sub> was formed (**Figure 6. 1b**) at 300 W and the same result was obtained at 600 W power as well (JCPDS Card No. 21-1272). These results have proved that crystalline anatase TiO<sub>2</sub> can be prepared by a comparatively low microwave power (300 W) within a smaller time 5 minutes. The crystallite size of as synthesized titanium dioxide were calculated using the Scherrer equation are shown in **Table 6. 1**. A small increase in crystallite size from 6.5 to 6.8 nm was observed when the microwave power was increased from 300 W to 600 W.

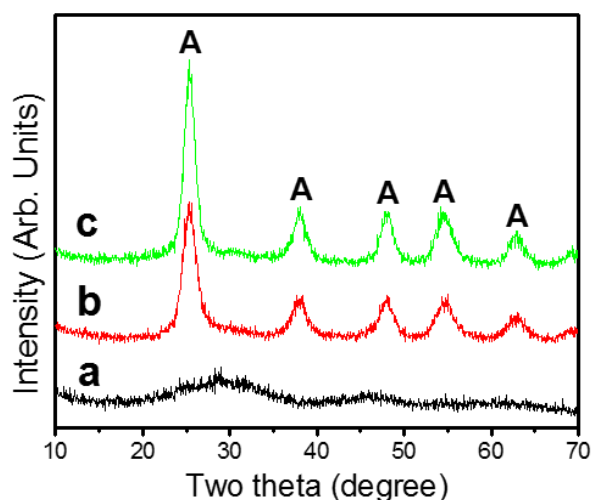


**Figure 6. 1.** XRD pattern of TiO<sub>2</sub> a) before irradiation b) at 300 W c) 600 W for 5 min irradiation (A=Anatase).

### 6. 2. 3. BET Surface Area

The surface area, pore volume and pore size of all microwave synthesized samples using ethanol were measured using a BET surface area analyzer. It can be seen from **Table 6. 1** that the microwave synthesized TiO<sub>2</sub> samples show very high surface area. The 300 W treated samples shows comparatively higher surface area as compared to the 600 W samples. This is attributed to the aggregation of particles which is higher for the samples prepared at 600 W. This aggregation will reduce the surface area of these samples. The N<sub>2</sub> adsorption and desorption isotherms are shown in **Figure 6. 2**. The adsorption and desorption isotherms of all samples have shown type IV behaviour with the typical hysteresis loop. This is the characteristic of mesoporous materials. The mesoporous nature of these samples is also evident from the adsorption and desorption measurements using BJH method (**Table 6. 1**).

**Table 6. 1. Crystallite size, BET Surface area and pore size of anatase TiO<sub>2</sub>.**

Power	Surface area (m <sup>2</sup> /g)	Pore volume (cm <sup>3</sup> /g)	Pore size (nm)	Crystallite size (nm)
300 W	210	0.263	2.3	6.5
600 W	205	0.266	2.4	7.8

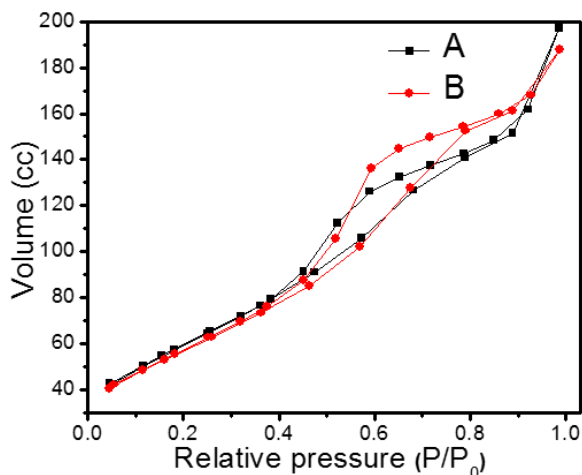


**Figure 6. 2. Type IV isotherm of TiO<sub>2</sub> synthesized using microwave power A) 300 W and B) 600 W.**

#### **6. 2. 4. SEM and TEM Analysis**

Scanning electron micrographs (SEM) of the TiO<sub>2</sub> samples prepared using the microwave method are shown in **Figure 6. 3A** and **6. 3B**. These TiO<sub>2</sub> particles are aggregated and have uniform distribution. However, the particle size of the aggregate varies at different microwave power. At 600 W power spherical aggregates are of large size (**Figure 6. 3B**) compared to lower power 300 W (**Figure 6. 3A**). These TiO<sub>2</sub> particles can adsorb more number of dye molecules on its surface as a result of its higher surface area.<sup>22</sup> It should have positively contributed towards the improvement in the efficiency of dye sensitized solar cells. The TEM image of microwave synthesized TiO<sub>2</sub> 600 W power is shown in **Figure 6. 3C**. TiO<sub>2</sub> nanoparticles of nearly uniform shape and spherical morphology were observed with

average particle size below 10 nm. The samples were further confirmed by high-resolution TEM (HRTEM) images (**Figure 6. 3D**). From the HRTEM image mesoporous fringes are clearly visible and the spacing of fringe pattern is found 0.34 nm, which corresponds to the (101) plane of anatase phase.<sup>23</sup> These observations indicate the mesoporous nature of the TiO<sub>2</sub> samples that have been synthesized along with its crystalline nature.

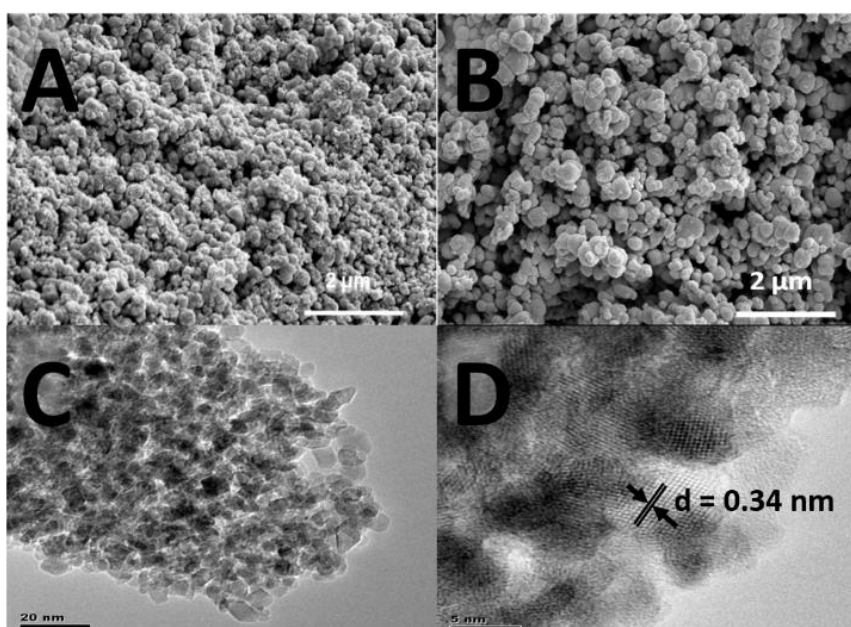


**Figure 6. 3. SEM images of anatase TiO<sub>2</sub> synthesized using microwave power A) 300 W and B) 600 W, C) TEM and D) HRTEM images of anatase TiO<sub>2</sub> synthesized using microwave power 600 W.**

### 6. 2. 5. Microwave TiO<sub>2</sub> as DSSC Photoanode

The anatase TiO<sub>2</sub> nanoparticles that have been synthesized are deposited on ITO plate using the screen-printing method in order to investigate the performance of those TiO<sub>2</sub> nanoparticles as DSSC working electrodes. The thickness of the films were measured by profilometer and it is found to be an average thickness value of 12 μm. Solar cells were constructed with the photoanode films made by using the TiO<sub>2</sub> synthesized at 300 W and 600 W. These cells were tested under dark condition and different illumination intensities of 10.3, 38.5 and 100 % of the sun. The device performance parameters obtained for the solar cell made up of TiO<sub>2</sub> synthesized at 300 and 600 W under different light illuminations are presented in **Table 6. 2 and 6. 3**. The I-V and IPCE data of these films under different illumination power were shown in **Figure 6. 4 and 6. 5**. As the illumination increases from 10.3 to 100% there is a significant increase in short circuit current (J<sub>SC</sub>) from 1.02 to 10.34 as shown in **Table 6. 2** for TiO<sub>2</sub> synthesized at 300 W whereas short circuit current (J<sub>SC</sub>) increased from a value from 1.28 to 11.84 which is slightly higher than the cell constructed using the TiO<sub>2</sub> synthesized at 600 W. The higher efficiencies of 6.43% and 6.60% were observed for the solar cells made up of TiO<sub>2</sub> synthesized at 300 and 600 W under 100% sunlight intensity. Interestingly 6.58% of efficiency is achieved under 10.3% sunlight (**Table 6. 3**) for DSC fabricated using TiO<sub>2</sub> synthesized at 600 W. This clearly evidenced the higher conversion efficiency of the solar cells at lower intensity of sunlight.

**Table 6. 2. Summary of open-circuit voltage, short-circuit current density, fill factor and overall light conversion efficiency of anatase TiO<sub>2</sub> (300 W/5 min) photoanode film.**

Light intensity	Dark sun	10.3% sun	38.5% sun	100.0% sun
Voc (mV)	-	725	772	804
Jsc (mA/cm <sup>2</sup> )	-	1.02	3.91	10.34
Fill factor	-	0.792	0.788	0.773
Efficiency (%)	-	5.68	6.18	6.43

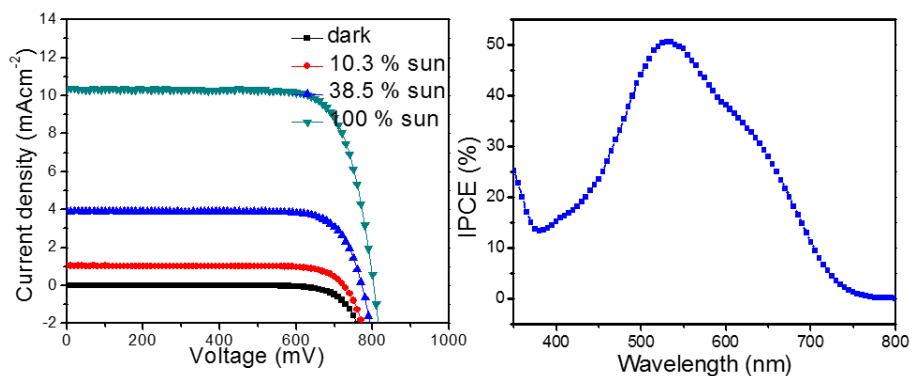


**Figure 6. 4. I-V characteristic of the solar cell fabricated using TiO<sub>2</sub> synthesized at 300 W photoanode films under different solar irradiation power (dark, 10.3, 38.5 and 100% sun) and IPCE curve.**

**Table 6. 3. Summary of open-circuit voltage, short-circuit current density, fill factor and overall light conversion efficiency of anatase TiO<sub>2</sub> (600 W/5 min) photoanode film.**

Light intensity	Dark sun	10.3% sun	38.5% sun	100.0% sun
Voc (mV)	-	693	737	766
Jsc (mA/cm <sup>2</sup> )	-	1.28	4.63	11.84
Fill factor	-	0.767	0.745	0.728
Efficiency (%)	-	6.58	6.60	6.60

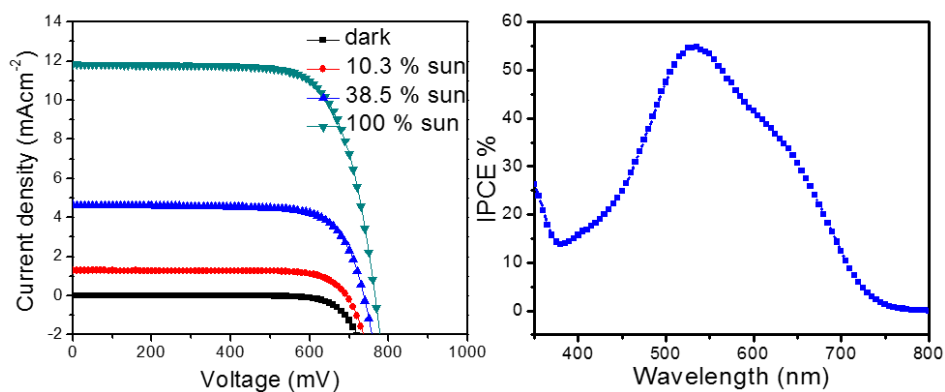


**Figure 6. 5. I-V characteristic of the solar cell fabricated using TiO<sub>2</sub> synthesized at 600 W photoanode films under different solar irradiation power (dark, 10.3, 38.5 and 100% sun) and IPCE curve.**

Incident photon current efficiency (IPCE) can be defined as the number of electrons in the external circuit under short circuit conditions per incident photon at a given wavelength.<sup>24</sup> IPCE at 540 nm has been measured for the solar cell constructed using photoanode film of anatase TiO<sub>2</sub> synthesized at 300 and 600 W are shown in **Figure 6. 4** and **6. 5**. As compared to the solar cell fabricated by TiO<sub>2</sub> synthesized using 300 W, the quantum efficiency was enhanced from 50% to 55% for the solar cell fabricated using TiO<sub>2</sub> that has been synthesized at 600 W. Connecting all the parameters those have been described here, it can be seen that the surface area is greater in the case of 300 W microwave treated TiO<sub>2</sub> (210 m<sup>2</sup>/g) as compared to 600 W microwave treated TiO<sub>2</sub> (205 m<sup>2</sup>/g). According to previous reports surface area is a crucial factor for the solar cell efficiency. Yu *et al.* reported the highest solar cell efficiency of TiO<sub>2</sub> nanosheets with a surface area ~2.5 times lower than that of TiO<sub>2</sub> nanoparticles (101 m<sup>2</sup>/g) and almost the same surface area to that of commercially available Degussa-P25 (45 m<sup>2</sup>/g).<sup>25</sup> Similarly here 210 m<sup>2</sup>/g and 205 m<sup>2</sup>/g are the surface area those have been calculated for 300 and 600 W microwave processed TiO<sub>2</sub> respectively. Here the reasons for the slight increase in the solar cell efficiency of 600 W microwave processed TiO<sub>2</sub> are due to higher pore volume, larger crystallite size and thereby good crystallization higher current density, J<sub>SC</sub> (11.84 mAcm<sup>-2</sup>) which is greater than 300 W microwave processed TiO<sub>2</sub> (10.34 mAcm<sup>-2</sup>) and most importantly the higher IPCE value, 55%. The higher pore volume can enhance transfer and diffusion of electrolyte. It is well known that the efficient diffusion of I<sub>3</sub><sup>-</sup> /I<sup>-</sup> to regenerate the dye is important to the photovoltaic response of the

solar cells.<sup>25</sup> Higher crystallize size and thereby good crystallization of 600 W microwave power processed TiO<sub>2</sub> meaning fewer imperfections located on the surface and in the bulk of particles, is beneficial to reduce the recombination of photogenerated electrons and holes at defects.<sup>26</sup> The maximum value of the IPCE spectra appears at 535 nm, and the IPCE of 600 W microwave power treated anatase TiO<sub>2</sub> solar cell is about 55%, obviously higher than that of the 300 W microwave power treated anatase TiO<sub>2</sub> solar cell (50%).

### **6. 3. Conclusions**

A rapid microwave assisted sol-gel synthesis of randomly oriented mesoporous anatase TiO<sub>2</sub> nanoparticles have been developed using titanium butoxide, ethanol and water as only precursors. Crystalline mesoporous anatase TiO<sub>2</sub> nanoparticles were obtained by using different microwave power 300 and 600 W on the TiO<sub>2</sub> sol for 5 minute irradiation. The crystallinity, morphology and textural properties of these anatase TiO<sub>2</sub> nanoparticles were examined by powder XRD, SEM, TEM and BET measurements. These TiO<sub>2</sub> nanomaterials consist of particles size ~10 nm and they have been successfully applied as photoanode in dye sensitized solar cells, obtained a higher efficiency of 6.6% with a fill factor of 73% using 1 sun. Solar cell efficiency of anatase TiO<sub>2</sub> nanoparticles that have been synthesized using 300 and 600 W power reveals that a notable increment in conversion efficiency from 6.43% to 6.6% respectively has been observed under 1 sun with increment in IPCE value from 50% to 55%.

## References

1. Y. Liu, Y. Chu, L. L. Li, L. H. Dong and Y. J. Zhuo, *Chem. Eur. J.*, 2007, **13**, 6667.
2. Y. Liu, Z. Chen, Z. Kang, I. Bello, X. Fan, I. Shafiq, W. Zhang and S. T. Lee, *J. Phys. Chem. C*, 2008, **112**, 9214.
3. X. Zhang, Y. Liu and Z. Kang, *ACS Appl. Mater. Interfaces*, 2014, **6**, 4480.
4. S. Lian, H. Huang, J. Zhang, Z. Kang and Y. Liu, *Solid State Commun.*, 2013, **155**, 53.
5. F. Shao, J. Sun, L. Gao, S. Yang and J. Luo, *J. Phys. Chem. C*, 2011, **115**, 1819.
6. P. Periyat, N. Leyland, D. E. McCormack, J. Colreavy, D. Corr and S. C. Pillai, *J. Mater. Chem.*, 2010, **20**, 3650.
7. F. A. Deorsola and D. Vallauri, *J. Mater. Sci.*, 2008, **43**, 3274.
8. O. Carp, C. L. Huisman and A. Reller, *Prog. Solid State Chem.*, 2004, **32**, 33.
9. U. Ozgur, Y. I. Alivov, C. Liu, A. Teke, M. A. Reshchikov, S. Dogan, V. Avrutin, S. J. Cho and H. Morkoc, *J. Appl. Phys.*, 2005, **98**, 041301.
10. G. J. Wilson, A. S. Matijasevich, D. R. Mitchell, J. C. Schulz and G. D. Will, *Langmuir*, 2006, **22**, 2016.

11. D. Zhang, H. Yin, Z. Li, Y. Zhou, T. Yu, J. Liu and Z. Zou, *RSC Adv.*, 2015, **5**, 65005.
12. H. E. Wang, L. X. Zheng, C. P. Liu, Y. K. Liu, C. Y. Luan, H. Cheng, Y. Y. Li, L. Martinu, J. A. Zapien and I. Bello, *J. Phys. Chem. C*, 2011, **115**, 10419.
13. M. Pazoki, N. Taghavinia, A. Hagfeldt and G. Boschloo, *J. Phys. Chem. C*, 2014, **118**, 16472.
14. C. W. Hsu, C. R. Ke, L. Chen, P. Chen and J. M. Ting, *Sol. Energy Mater. Sol. Cells*, 2016, **144**, 7.
15. J. Luo, L. Gao, J. Sun and Y. Liu, *RSC Adv.*, 2012, **2**, 1884.
16. X. Chen, Q. Tang, Z. Zhao, X. Wang, B. He and L. Yu, *Chem. Commun.*, 2015, **51**, 1945.
17. C. Chen, L. Xu, G. A. Sewvandi, T. Kusunose, Y. Tanaka, S. Nakanishi and Q. Feng, *Cryst. Growth Des.*, 2014, **14**, 5801.
18. K. Patra, A. Dutta and A. Bhaumik, *J. Phys. Chem. C*, 2014, **118**, 16703.
19. L. Li, C. Xu, Y. Zhao, S. Chen and K. J. Ziegler, *ACS Appl. Mater. Interfaces*, 2015, **7**, 12824.
20. G. Salvinelli, G. Drera, C. Baratto, A. Braga and L. Sangaletti, *ACS Appl. Mater. Interfaces*, 2014, **7**, 765.

21. Alberti, G. Pellegrino, G. G. Condorelli, C. Bongiorno, S. Morita, A. La Magna and T. Miyasaka, *J. Phys. Chem. C*, 2014, **118**, 6576.
22. M. Zikalova, A. Zikal, L. Kavan, M. K. Nazeeruddin, P. Liska, M. Grätzel, *Nano Lett.*, 2005, **5**, 1789.
23. Y. Zhang, F. M. Liu, *RSC Adv.*, 2015, **5**, 66934.
24. Hagfeldt, G. Boschloo, L. Sun, L. Kloo and H. Pettersson, *Chem. Rev.*, 2010, **110**, 6595.
25. J. Yu, J. Fan and K. Lv, *Nanoscale*, 2010, **2**, 2144.
26. Q. J. Xiang, K. L. Lv and J. G. Yu, *Appl. Catal. B*, 2010, **96**, 557.

# 7 Chapter

## Sol-Gel Derived ZnO Nanoribbons as Photoanode Material in Dye Sensitized Solar Cell

### Contents

- 7. 1. Introduction
- 7. 2. Results and Discussion
- 7. 3. Conclusions
- References

### 7. 1. Introduction

Although TiO<sub>2</sub> semiconducting oxide film have been the most widely studied DSSC photoanode material,<sup>1,2,3,4</sup> Zinc oxide (ZnO) has recently been identified as a promising material for use as photoanode in DSSCs.<sup>5,6</sup> Exploitation of the advantages of ZnO such as the similar band gap of ZnO to that of TiO<sub>2</sub>, higher electron mobility than TiO<sub>2</sub>, easy tailoring and easy surface modification led towards a suitable photoanode material alternative to TiO<sub>2</sub>.<sup>7,8,9</sup> Structurally different nano and micro sized ZnO have been prepared and utilized for visible light photocatalysis and electrochemical water splitting.<sup>10,11,12,13</sup> For e.g. Liu *et al.* reported the controlled fabrication of highly oriented ZnO microrod and microtube arrays and nano ZnO tetrapods, nano tetra spikes, nanowires and spheres were developed.<sup>10,11</sup> This illustrates the

ease with which ZnO can be made and its utilization for variety of applications.<sup>10,11,12,13,14,15,16,17</sup>

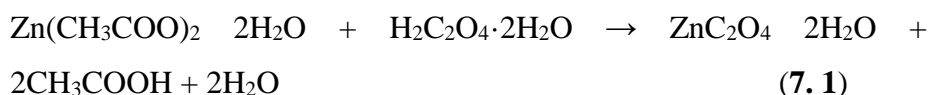
Sol-gel route is one preferred methods for the synthesis of nanomaterials, because of its low cost and relatively mild processing. In fact, sol-gel methods, especially those involving polymeric precursors, have provided the impetus for the majority of scientific and technological applications of ZnO nanoparticles. Previous work on the DSSCs, has identified that the electrode material morphology, shape and size, surface structure, particle size, porosity and the film thickness are all important factors for optimizing device performance.<sup>18</sup> For ZnO, these factors can easily be tailored through the modification of wet-chemical methods such as sol-gel method to obtain the ZnO nanostructures having required properties.

Various ZnO nanostructures, such as nanotips, nanorods, nano flowers, nanosheets, nanobelts have been fabricated using different methodology and used as DSSC photoanode materials.<sup>19,20,21,22</sup> For example, a DSSC fabricated using ZnO nanorod showed an efficiency of 1% whereas higher efficiencies of 1.9% were achieved with the nano flower material<sup>26,27</sup> and 1.5% with the nanosheet ZnO based materials.<sup>28</sup> DSSCs fabricated using ZnO nano tips electrode have been reported to have a power conversion efficiency of 0.77% under the illumination of a one sun-simulated sunlight.<sup>29</sup> Aspects that have not been explored in detail in these previous studies are the relationship between photoanode film thickness and dyeing time on the DSSC efficiency.

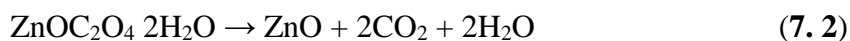
In this work, the facile synthesis of ZnO nanoparticles through simple and low cost sol-gel method from a zinc (II) acetate precursor in the presence of oxalic acid and its application as a photoanode in DSSCs. The structure and morphology of the nanocrystalline ZnO produced on calcination has been studied using variety of characterization techniques, such as XRD, Raman, FTIR, TEM and SEM. Further this new material was successfully applied as a photoanode in DSSCs and the influence of ZnO film thickness on the efficiency of the dye sensitized solar cells were examined.

## 7. 2. Results and discussion

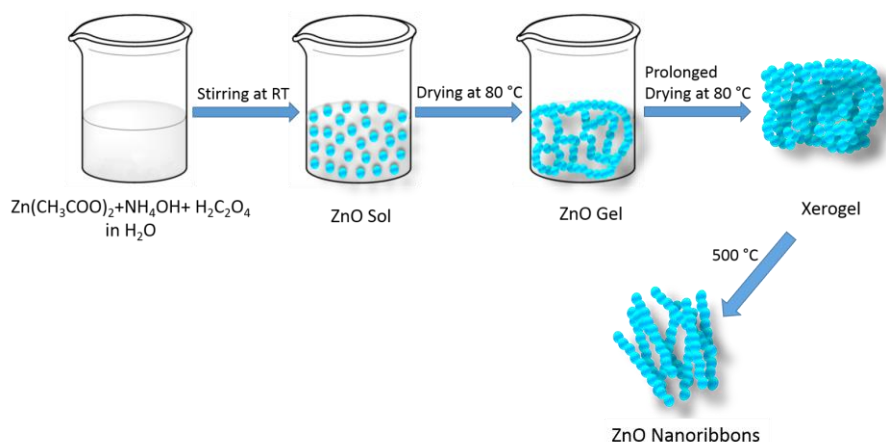
Nanocrystalline ZnO was prepared by a straightforward one step sol-gel route in which zinc (II) acetate was first converted to zinc (II) oxalate by reacting with oxalic acid as shown in **equation 7. 1**.



Conversion to ZnO was completed by heat treatment of zinc (II) oxalate at 500 °C in presence of oxygen (**equation 7. 2**):



A schematic illustration of the synthesis of ZnO nanoribbon is shown in **Scheme 7. 1**.



**Scheme 7. 1. Schematic illustration of the synthesis of ZnO nanoribbons.**

### 7. 2. 1. X ray Diffraction

The XRD pattern of the xero-gel obtained at 80 °C and the ZnO obtained by heating xero-gel at 500 °C were shown in **Figure 7. 1**. The XRD pattern at 80 °C consists mainly of peaks that can be assigned to zinc (II) oxalate (JCPDS 01-075-7129) along with a small percentage of ZnO whereas the XRD at 500 °C is typical pattern of ZnO with a wurtzite structure (JCPDS -01-036-1451). The crystal size of ZnO calculated using Scherrer equation was  $25 \pm 5$  nm. The nanocrystalline nature and phase purity of the ZnO calcined at 500 °C was clear from the XRD measurements.

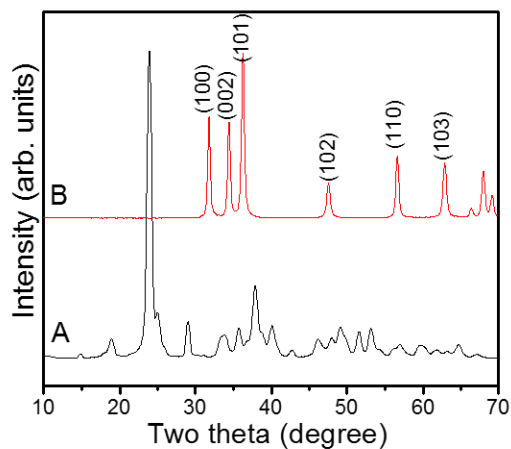


**Figure 7. 1. Powder XRD pattern of A) the zinc oxalate precursor and B) ZnO formed by calcination at 500 °C.**

### 7. 2. 2. FTIR Spectroscopy

The formation of nanocrystalline ZnO with a wurtzite structure from zinc oxalate was further confirmed by FT-IR spectral analysis, which is shown in **Figure 7. 2**. The spectrum of as-prepared xero-gel of ZnO precursor prior to calcination showed an absorption peak at  $3400\text{ cm}^{-1}$ , which corresponds to the O-H stretching arising from OH groups bound to the ZnO or surface adsorbed water molecules. The three bands occurring in the region of  $1000\text{-}500\text{ cm}^{-1}$  and a sharp peak at  $1630\text{ cm}^{-1}$  correspond to the to the asymmetric and symmetric stretching of the carboxyl ( $-\text{CO}_2^-$ ).<sup>23</sup> The band at  $1630\text{ cm}^{-1}$  is mainly due to -OH bending but there may be an underlying band due to the asymmetric  $-\text{CO}_2$  stretch, the symmetric stretch is either at  $1316$  or  $1361\text{ cm}^{-1}$  or both. Further the symmetric and asymmetric stretching bands of acetate species can be observed at  $1316$  and  $1361\text{ cm}^{-1}$ .<sup>24</sup> These spectral features indicate that zinc oxalate has been formed by

the reaction between zinc acetate and oxalic acid as indicated by the previous equation 1 and 2. For the ZnO calcined at 500 °C, the absorptions corresponding to water, hydroxyl, oxalate and acetate vibrations are no longer present and showed only a strong ZnO peak at 490  $\text{cm}^{-1}$ .<sup>25</sup>

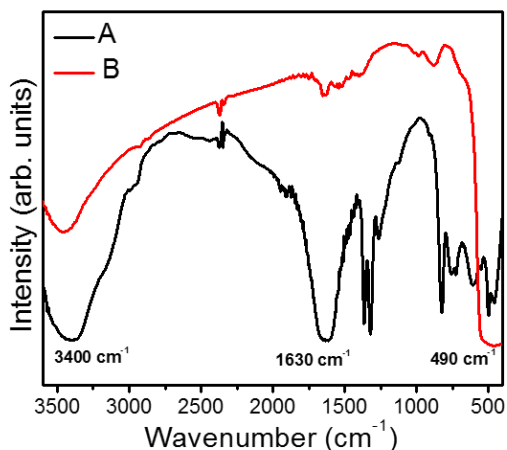


**Figure 7. 2. FTIR spectra of a) the zinc oxalate suspension prepared at 80 °C and b) ZnO calcined at 500 °C.**

### 7. 2. 3. Raman and UV-Visible Spectroscopy

The Raman spectrum of ZnO calcined at 500 °C is shown in **Figure 7. 3A**. The most intense peak at 436  $\text{cm}^{-1}$  corresponds to  $E_2$  mode of ZnO hexagonal wurtzite structure, while the one at 326  $\text{cm}^{-1}$  can be assigned as the second order Raman spectrum arising from the zone boundary phonons  $3E_{2H} - E_{2L}$ .<sup>26</sup> A strong  $E_2$  mode indicates highly crystalline ZnO with only a very low oxygen vacancy. The absorption spectrum of the ZnO powder calcined at 500 °C was shown in **Figure 7. 3B**. Maximum absorbance of the ZnO showed a value of 374 nm. The band

gap was calculated from this absorbance is found to be 3.3 eV which is in agreement with the reported value.<sup>27</sup>

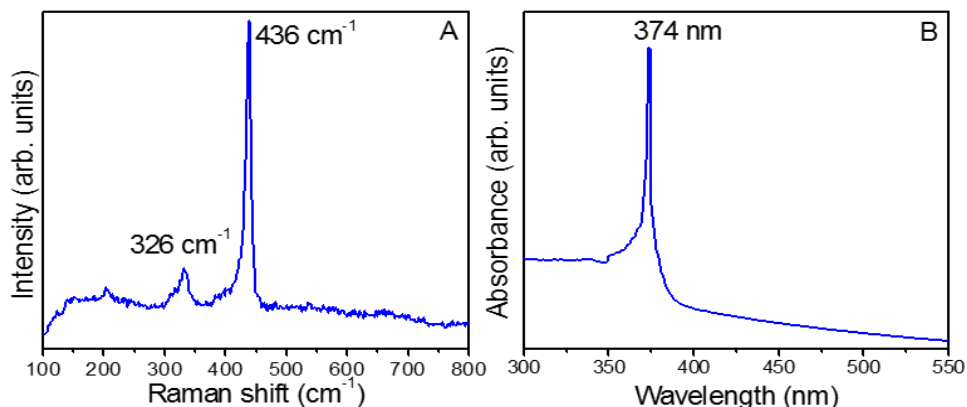


**Figure 7. 3. A) Raman spectrum and B) absorption spectrum of ZnO calcined at 500 °C.**

#### 7. 2. 4. TEM and SEM Analysis

**Figure 7. 4A** represents the TEM image of nanocrystalline ZnO synthesized and **Figure 7. 4A** shows a selected area diffraction pattern (SAED) from a region of the TEM sample and indexed according to the hexagonal wurtzite ZnO structure. In **Figure 7. 4A**, ZnO particles are arranged in two distinct types, they are not single crystal. One type (a majority) appears to be a roughly linear assemblage of crystallites in the 5-50 nm size range whilst the other appears featureless at this magnification. In the SAED, the ring-like pattern indicates the finely polycrystalline morphology, however, the sharp spots in the rings confirm that individual nanocrystals are well formed and relatively perfect. **Figure 7. 4C** represents the higher magnification image of

ZnO nanocrystals and at this higher magnification (**Figure 7. 4C**), the perfection of the larger crystallites of ZnO is evident whilst the featureless ZnO particles (**Figure 7. 4A**) resolve into very finely polycrystalline assemblages of 2-10 nm particles (**Figure 7. 4D**). The SEM image (**Figure 7. 5**) indicates the nanoribbon morphology of ZnO.

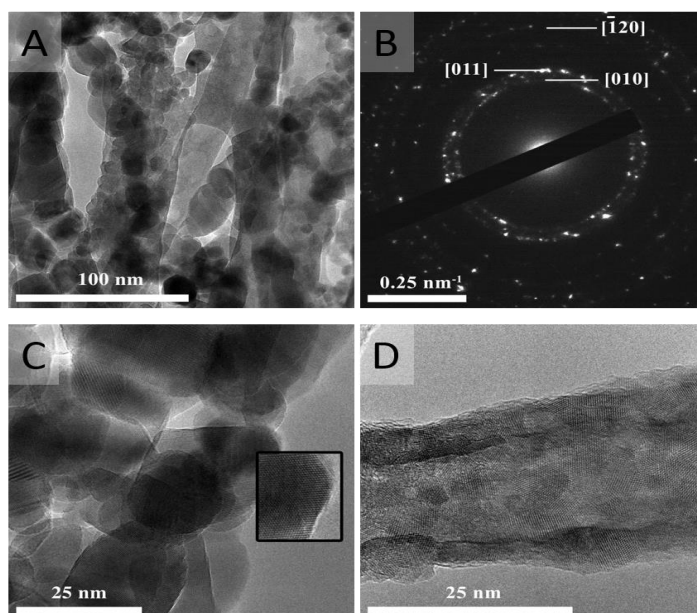


**Figure 7. 4. A) TEM image of well-ordered ZnO nano ribbon B) SAED pattern C) HRTEM of part of a crystalline ZnO ribbon showing (inset) the high degree of order in these nanocrystals and D) higher magnification TEM image of ZnO nanoribbon.**

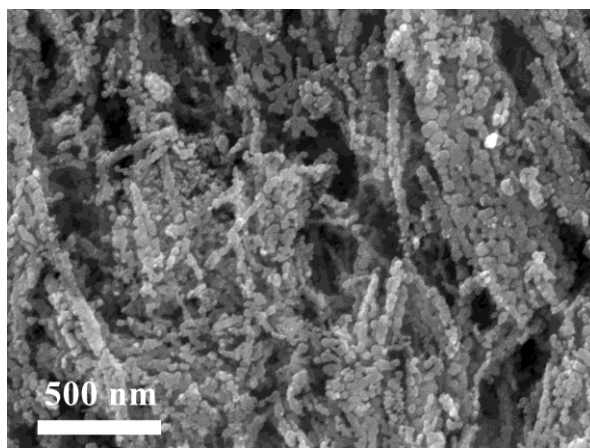


**Figure 7. 5. SEM micrograph of a ZnO photoanode film annealed at 500 °C showing the nanoribbon morphology.**

#### **7. 2. 5. ZnO as DSSC Photoanode**

In order to investigate the performance of the ZnO as DSSC working electrodes, ZnO films having different thicknesses were deposited using the screen-printing method. The thickness of the films were measured by profilometer and showed values of 4, 8, 12, 16 and 20  $\mu\text{m}$ . A typical SEM micrograph of a ZnO film annealed at 500 °C as shown in Figure 7. 5. The ribbon-like arrangement of ZnO morphology observed in the HRTEM of the powdered sample annealed at 500 °C is clearly evident in SEM image (**Figure 7. 5**). Solar cells constructed with ZnO photoanaode of different thicknesses (4-20  $\mu\text{m}$ ) were tested under dark condition and different illumination intensities of 10.3, 38.5 and 100 % of sun. These photoanode films had been dyed in a 0.3 mM solution of N719 dye for either 2 or 24 hrs. This allowed us to compare the effect of dyeing time on device efficiency and to explore whether

precipitation of the dyes, the stability of the ZnO film or other factors affected the cell efficiency.

**Figure 7. 6** and **7. 7** shows the I-V characteristic of devices constructed with ZnO films having thicknesses 8, 12, 16 and 20  $\mu\text{m}$  for the two different dyeing times and at various light intensities. The device performance parameters obtained under 1 sun (100% sun intensity) illuminations are presented in **Table 7. 1**. For the initial set of experiments, conducted with films dyed for 24 hours there is a significant increase in short circuit current ( $J_{\text{SC}}$ ) and fill factor as the film thickness increases from 4  $\mu\text{m}$  to 16  $\mu\text{m}$ , (see **Figure 7. 6** and **Table 7. 1**) which results in an increase in efficiency from 0.45 % for a 4  $\mu\text{m}$  thick film to 1.86 % for a 16  $\mu\text{m}$  film. However, a further increase in film thickness to 20  $\mu\text{m}$  causes a slight decrease in efficiency to 1.67%, arising mainly from a decrease in the fill factor. The observed increase in  $J_{\text{SC}}$ , and hence efficiency, is probably due to an increase in dye loading that is associated with the higher film thickness resulting in higher photon absorption.<sup>6,37</sup> The plot of efficiency Vs thickness is shown in **Figure 7. 8**, where the efficiency was linearly increases with thickness upto 16  $\mu\text{m}$  and then decreases for 20  $\mu\text{m}$  film thickness.

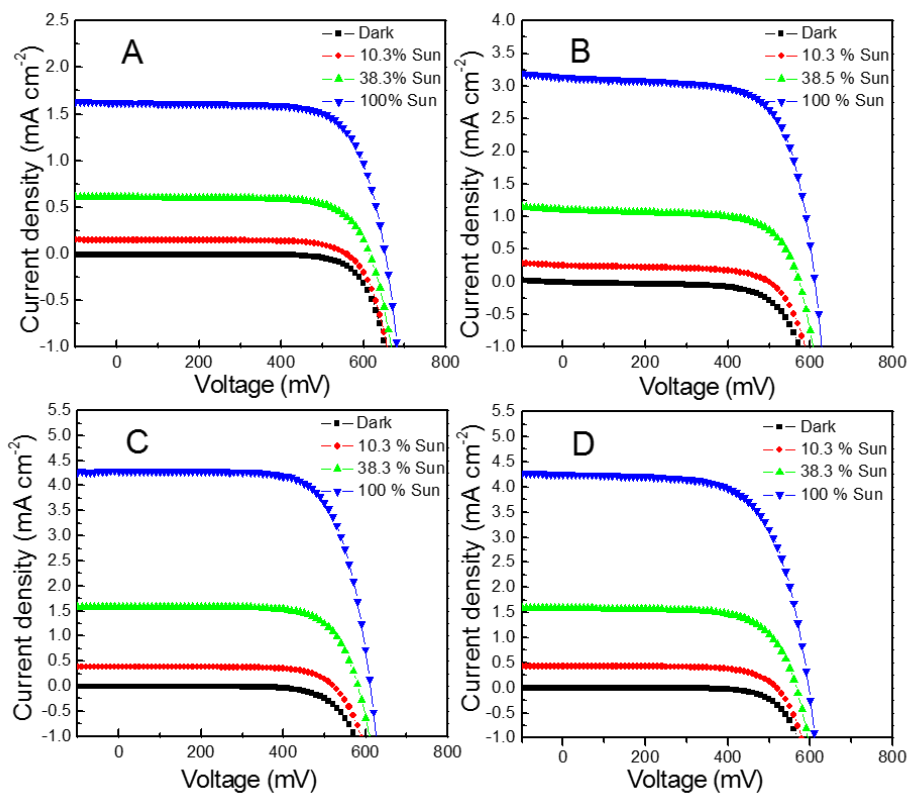


**Figure 7. 6. I-V characteristic of the solar cell fabricated using 24 hr dyed ZnO photoanode films having different thickness: A) 8  $\mu\text{m}$ , B) 12  $\mu\text{m}$ , C) 16  $\mu\text{m}$ , and D) 20  $\mu\text{m}$  under different solar irradiation power.**

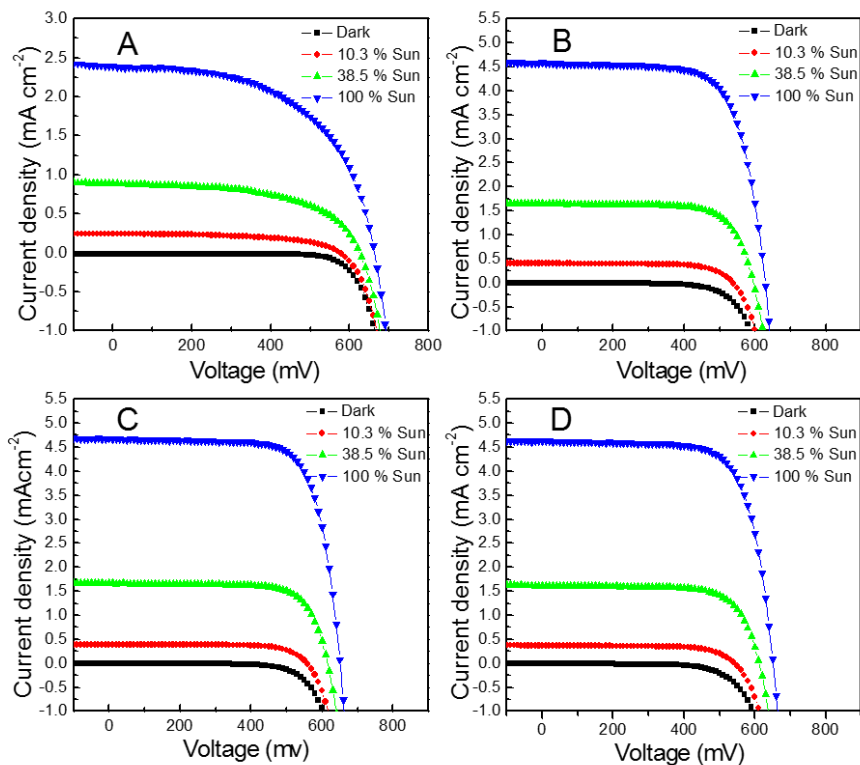


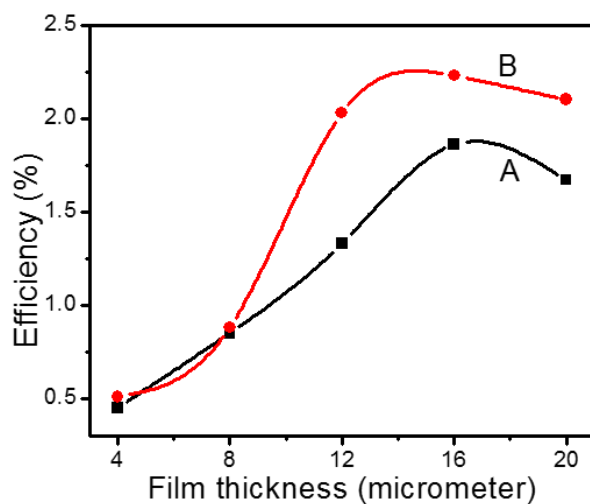
**Figure 7. 7. I-V characteristic of the solar cell fabricated using 2 hr dyed ZnO photoanode films having different thickness: A) 8  $\mu\text{m}$ , B) 12  $\mu\text{m}$ , C) 16  $\mu\text{m}$ , and D) 20  $\mu\text{m}$  under different solar irradiation power.**

**Table 7. 1. Summary of open-circuit voltage, short-circuit current density, fill factor and overall light conversion efficiency relative to the type of ZnO film under 1 sun (100 % sun intensity) illumination.**

<b>24 h Dyeing</b>					
<b>Film Thickness (<math>\mu\text{m}</math>)</b>	4	8	12	16	20
<b>Voc (mV)</b>	629	636	612	612	596
<b>Jsc (mA/cm<sup>2</sup>)</b>	1.15	1.88	3.14	4.29	4.25
<b>Fill Factor (%)</b>	63	71	70	71	66
<b>Efficiency (%)</b>	0.45	0.85	1.33	1.86	1.67

<b>2 h Dyeing</b>					
<b>Film Thickness (<math>\mu\text{m}</math>)</b>	4	8	12	16	20
<b>Voc (mV)</b>	651	663	629	651	651
<b>Jsc (mA/cm<sup>2</sup>)</b>	1.54	2.39	4.59	4.68	4.63
<b>Fill Factor (%)</b>	52	55	70	73	72
<b>Efficiency (%)</b>	0.51	0.88	2.03	2.23	2.17



**Figure 7. 8. Plot of efficiency Vs thickness of A) 24 hr dyed films and B) 2 hrs dyed films.**

To examine whether the dyeing time influenced the cell performance, devices constructed with films dyed for two hours were tested. The trend in device performance followed that observed for films dyed for 24 hrs, that is, an increase in short circuit current and fill factor accompanies the increase in film from 4  $\mu\text{m}$  to 16  $\mu\text{m}$ , no further increase in efficiency for the 20  $\mu\text{m}$  thick films. The highest efficiencies of 2.2 % were observed for these films when compared with 1.9 % for the 24 hour dyed films. This difference in efficiency for different dyeing time has been attributed to the precipitation of the dye in pores of the nanocrystalline ZnO structure as the dyeing time increases.<sup>6,28</sup> The dissolution of ZnO structure by the acidic carboxylic anchoring groups of the sensitizer can take place and the resulting  $\text{Zn}^{2+}$

ions complexes with the N719 dye, causing precipitation of these complexes in the pores of the film.<sup>37</sup> This gives rise to a filter effect by forming inactive dye molecules, so that net yield for charge carrier injection is decreased and a corresponding decrease in efficiency will take place for solar cell constructed with longer time dyed film electrode.

### **7.3. Conclusions**

In conclusion, a facile sol-gel synthesis of nanocrystalline ZnO has been developed using zinc acetate and oxalic acid as precursors. The morphology and spectroscopic properties of the ZnO have been studied by powder XRD, FTIR and Raman spectroscopy, SEM and TEM. These ZnO material consists of crystallites having around 25 nm in size. These nanocrystalline ZnO material has been successfully applied as photoanode in the dye sensitized solar cells and obtained an efficiency of 2.2% with a very high fill factor of >73%. Investigations on the effect of varying the ZnO photoanode film thickness and dyeing time influenced the solar cell performance. Solar cell efficiency study using different thickness film thickness (4-20  $\mu\text{m}$ ) showed that the efficiency increased from 0.51% to 2.23% when the film thickness increases from 4  $\mu\text{m}$  to 16  $\mu\text{m}$  and then remains constant or decreases slightly for 20  $\mu\text{m}$  film. Thus, the optimum thickness to obtain maximum efficiency was 16  $\mu\text{m}$  irrespective of the dyeing time.

### **References**

1. F. Y. Moussa, Y. Boukennous and A. Elkechai, *Mater. Sci. Semicond. Process.*, 2013, **16**, 51.

2. M. Hamadani, V. Jabbari and A. Gravand, *Mater. Sci. Semicond. Process.*, 2012, **15**, 371.
3. S. Erten-Ela , S. Sogu and K. Ocakoglu, *Mater. Sci. Semicond. Process.*, 2014, **23**, 159.
4. R. Jayakrishnan, S. Gandhi and P. Suratkar, *Mater. Sci. Semicond. Process.*, 2011, **14**, 223.
5. K. Keis, E. Magnusson, H. Lindstrom, S.E. Lindquist and A. Hagfeldt, *Sol. Energy Mater. Sol. Cells*, 2002, **73**, 51.
6. Q. Zhang, T. P. Chou, B. Russo, S. A. Jenekhe and G. Cao, *Adv. Mater.*, 2008, **47**, 2402.
7. T. P. Chou, Q. Zhang, G. E. Fryxell and G. Cao, *Adv. Mater.*, 2007, **19**, 2588.
8. M. Grätzel, *Nature*, 2001, **414**, 338.
9. E. M. Kaidashev, M. Lorenz, H. von Wenckstern, A. Rahm, H. C. Semmelhack, K. H. Han, G. Benndorf, C. Bundesmann, H. Hochmuth and M. Grundmann, *Appl. Phys. Lett.*, 2003, **82**, 3901.
10. Y. Liu, Y. Chu, L. L. Li, L. H. Dong and Y. J. Zhuo, *Chem. Eur. J.*, 2007, **13**, 6667-6673.
11. Y. Liu, Z. Chen, Z. Kang, I. Bello, X. Fan, I. Shafiq, W. Zhang, and S-T Lee, *J. Phys. Chem. C*, 2008, **112**, 9214.

12. X. Zhang, Y. Liu and Z. Kang, *ACS Appl. Mater. Interfaces*, 2014, **6**, 4480.
13. S. Lian, H. Huang, J. Zhang, Z. Kang and Y. Liu, *Solid State Commun.*, 2013, **155**, 53.
14. B. Weintraub, Z. Zhou, Y. Li and Y. Deng, *Nanoscale*, 2010, **2**, 1573.
15. Z. L.Wang, *J. Phys.: Condens. Matter*, 2004, **16**, 829.
16. Z. L.Wang, *Mater. Sci. Eng. B*, 2009, **R64**, 33.
17. U. Ozgur, Y. I. Alivov, C. Liu, A. Teke, M. A. Reshchikov, S. Dogan, V. Avrutin, S. J. Cho and H. Morkoc, *J. Appl. Phys.*, 2005, **98**, 041301.
18. A. Hagfeldt, G. Boschloo, H. Lindström, E. Figgemeier, A. Holmberg, V. Aranyos, E. Magnusson and L. Malmqvist, *Coord. Chem. Rev.*, 2004, **248**, 1501.
19. H. H. Chen, A. Du Pasquier, G. Saraf, J. Zhong and Y. Lu, *Semicond. Sci. Technol.*, 2008, **23**, 45004.
20. A. Du Pasquier, H. H. Chen and Y. C. Lu, *Appl. Phys. Lett.*, 2006, **89**, 253513.
21. A. E. Suliman, Y. Tang and L. Xu, *Sol. Energy Mater. Sol. Cells*, 2007, **91**, 1658.

22. C. Y. Jiang, X. W. Sun, G. Q. Lo and D. L. Kwong, *Appl. Phys. Lett.*, 2007, **90**, 263501.
23. E. Reverchon, G. D. Porta, D. Sannino and P. Ciambelli, *Powder Technol.*, 1999, **102**, 127.
24. C. P. Sibin, S. R. Kumar, P. Mukundan and K. G. K. Warriar, *Chem. Mater.*, 2002, **14**, 2876.
25. K. G. Kanade, B. B. Kale, R. C. Aiyer and D. K. Das, *Mater. Res. Bull.*, 2006, **41**, 590.
26. J. J. Wu and S. C. Liu, *J. Phys. Chem. B*, 2002, **106**, 9546.
27. S. Park, S. J. Tark, J. S. Lee, H. Lim and D. Kim, *Sol. Energy Mater. Sol. Cells*, 2009, **93**, 1020.
28. S. Nakade, Y. Makimoto, W. Kubo, T. Kitamura, Y. Wada and S. Yanagida, *J. Phys. Chem. B*, 2006, **109**, 3488.

# 8 Chapter

## Overall Conclusions and Future Outlook

### Contents

- 8. 1. Overall Conclusions
- 8. 2. Future Outlook
- References

### 8. 1. Overall Conclusions

The aim of the present research work was to explore the preparation of semiconducting metal oxide micro/nanomaterials of TiO<sub>2</sub> and ZnO a using different methods such as microwave, gel combustion, solution processing and sol-gel method. Later the same metal oxide and were employed in the area of photocatalysis and/or dye sensitized solar cells (DSSC). The introduction and the experimental sections have been reviewed in Chapter 1 and 2 respectively. The research works are included under chapter 3 to chapter 7.

In Chapter 3, a green and rapid microwave syntheses of ‘yellow oxygen rich’ (YAT-150) and ‘black oxygen vacancy rich’ (BAT-150) anatase TiO<sub>2</sub> nanoparticles have been reported for the first time by *in situ* Mn<sup>2+</sup> modification. As synthesized ultra-small (~5 nm) yellow and black anatase TiO<sub>2</sub> nanoparticles were found two fold and four fold

more photoactive than the commercially available photocatalyst Degussa-P25 under sunlight illumination.

In Chapter 4, a one pot gel combustion synthetic strategy has been developed for the first time towards the rapid formation of self-doped black anatase  $\text{TiO}_{2-x}$  (BAT) using titanium butoxide, diethylene glycol (DEG) and water as the only precursors. This swiftly formed nanoplatform was occupied with a high concentration of surface defect sites, especially  $\text{Ti}^{3+}$  and oxygen vacancy sites in excess. These defect-enriched features enabled 33% more photocatalytic activity for BAT than Degussa-P25 under solar illumination.

In Chapter 5, dopant free, solar active ZnO photocatalysts with oxygen vacancy richness were achieved by a solution processing strategy followed by calcination at various temperatures 300, 500, 700, 800 and 900 °C. All the ZnO nanocrystals possessed defective structures with copious surface oxygen vacancies directed towards notable visible light absorption around  $\lambda = 480$  nm (band gap = 3.05 - 3.09 eV). Methylene blue (MB) dye was used as model system in all photocatalytic experiments, where the ZnO calcined at 500 °C, having maximum surface oxygen vacancy has shown a two-fold photoactivity than the commercially available photocatalyst Degussa- P25 under solar illumination.

In Chapter 6, a facile and rapid synthesis of randomly distributed mesoporous anatase  $\text{TiO}_2$  nanoparticles for DSSC application using microwave method has been introduced. Nanocrystalline anatase  $\text{TiO}_2$  were achieved at low microwave power intensity (300 and 600 W) for

5 min irradiation. These anatase TiO<sub>2</sub> nanoparticles possessed high surface area up to 210 m<sup>2</sup>g<sup>-1</sup>. These anatase TiO<sub>2</sub> nanoparticles were successfully employed as the working electrode for DSSC and a systematic investigation of the performance of DSSC constructed with standard N719 dye with conventional iodide/triiodide (I<sup>-</sup>/I<sub>3</sub><sup>-</sup>) has demonstrated an efficiency of 6.6% under 100% sunlight.

In Chapter 7, nanoribbon ZnO with 25 nm average particle size has been synthesized by a facile sol-gel synthesis. This material has been successfully applied as photoanode material in DSSCs. A systematic investigation of the performance of DSSCs with film thickness and dyeing time had also been carried out. Among the five different film thickness 4, 8, 12, 16 and 20 μm prepared, best result was obtained for the film thickness of 16 μm for 2 hrs dyeing showed an efficiency of 2.2% with a J<sub>sc</sub> of 4.7 mA cm<sup>-2</sup> and a very high fill factor of >73%.

## **8. 2. Future Outlook**

### **8. 2. 1. Black TiO<sub>2</sub> as new generation electron transporters in Dye Sensitized Solar Cells (DSSCs) and Perovskite Solar Cells (PSCs)**

The world has no longer rely fully on non-renewable resources for power generation. Also the present energy production and distribution system faces a number of physical threats. Therefore a reliable, clean, abundant and affordable energy source can eliminate the current difficulties by implementing a long wavelength (infrared) absorbing material such as black TiO<sub>2</sub>, in DSSCs and PSCs. In addition, these new generation solar cells require little maintenance and are highly cost effective in their operation. Till date the efficiency has been

reached around 23% for both DSSC and PSC.<sup>1</sup> Therefore this technology can make an important contribution in energy technology for many reasons. It has numerous environmental benefits and as a domestic source of electricity, it contributes to the world's energy security. The photovoltaic industry estimates a growth rate of 25% in the near future according to the United States Energy Efficiency and Renewable Energy (EERE) agency.<sup>2</sup> EERE also predicts a huge market for this type of technology by 2020.<sup>2</sup> With these technological innovations to develop low cost and highly efficient solar cells, these technologies can become a major source of energy which could contribute significantly to industrial growth worldwide.

We have synthesized black TiO<sub>2</sub> by a sol-solvothermal strategy which is not a part of this thesis. This IR absorbing black TiO<sub>2</sub> nanoparticles has been implemented as photoanode in dye sensitized solar cell (DSSC) and that has been compared with the DSSC, where the photoanode was the commercially available P25. The cell efficiency ( $\eta$ ) of black TiO<sub>2</sub> has found 3.45%, whereas the P25 based DSSC has shown an efficiency of 1.93%. Distinctly, the efficiency of the IR absorbing black anatase TiO<sub>2</sub> was 79% more to that of P25-TiO<sub>2</sub>. Since we have found such a promising result using black TiO<sub>2</sub> in DSSC, I hope that black TiO<sub>2</sub> has the potential to be the new generation electron transport material both in dye sensitized and perovskite solar cells.

### 8. 2. 2. Black TiO<sub>2</sub> in Li ion Batteries

In addition to these experiments, mesoporous spherical black TiO<sub>2</sub> has been synthesized and implemented also in Li ion batteries. A specific capacity of 150 mAhg<sup>-1</sup> has been achieved and the efficiency was unchanged up to 20 cycles.

#### References

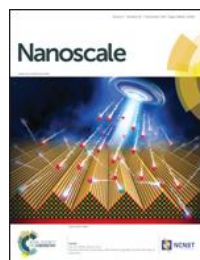
1. a) S. Shalini, R. Balasundaraprabhu, T. S. Kumar, N. Prabavathy, S. Senthilarasu and S. Prasanna, *Int. J. Energy Res.*, 2016, **40**, 1303; b) L. Calió, S. Kazim, M. Grätzel and S. Ahmad, *Angew. Chem. Int. Ed.*, 2016, **55**, 14522.
2. [www.eere.energy.gov](http://www.eere.energy.gov)

# Publications by the Author

## *Journal Articles*



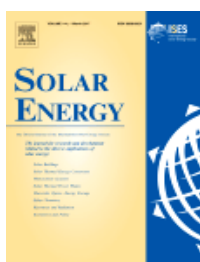
S. G. Ullattil and P. Periyat, A ‘One Pot’ Gel Combustion Strategy towards  $\text{Ti}^{3+}$  Self-Doped ‘Black’ Anatase  $\text{TiO}_{2-x}$  Solar Photocatalyst, *J. Mater. Chem. A*, 2016, 4, 5854 (**Impact Factor: 8.262**).



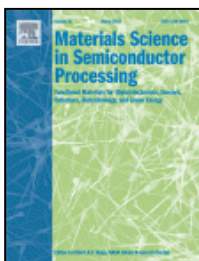
S. G. Ullattil and P. Periyat, Green Microwave Switching from Oxygen Rich Yellow Anatase to Oxygen Vacancy Rich Black Anatase  $\text{TiO}_2$  Solar Photocatalyst Using Mn(II) as Anatase Phase Purifier, *Nanoscale*, 2015, 7, 19184 (**Impact Factor: 7.76**).



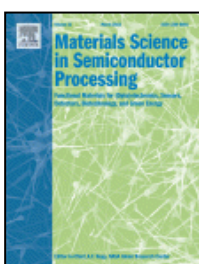
S. G. Ullattil, P. Periyat, B. Naufal and M. A. Lazar, Self-doped ZnO Microrods - High Temperature Stable Oxygen Deficient Platforms for Solar Photocatalysis, *Ind. Eng. Chem. Res.*, 2016, 55, 6413 (**Impact Factor: 2.567**).



S. G. Ullattil and P. Periyat, Microwave-Power Induced Green Synthesis of Randomly Oriented Mesoporous Anatase  $\text{TiO}_2$  Nanoparticles for Efficient Dye Sensitized Solar Cells, *Sol. Energy*, 2017, 147, 99 (**Impact Factor: 3.685**).

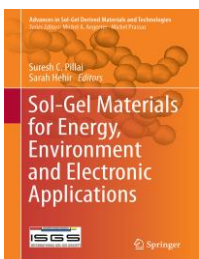


P. Periyat and **S. G. Ullattil**, Sol-Gel Derived Nanocrystalline ZnO Photoanode Film for Dye Sensitized Solar Cells, *Mater. Sci. Semicond. Process.*, 2015, *31*, 139 (**Impact Factor: 2.264**).

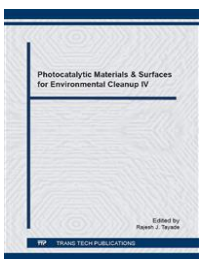


P. Periyat, P. A. Saeed and **S. G. Ullattil**, Anatase Titania Nanorods by Pseudo-Inorganic Templating, *Mater. Sci. Semicond. Process.*, 2015, *31*, 658 (**Impact Factor: 2.264**).

### ***Book Chapters***



**S. G. Ullattil** and P. Periyat, Sol-Gel Synthesis of Titanium Dioxide, *Sol-Gel Materials for Energy, Environment and Electronic Applications*, Chapter 9, 271 (ISBN: 978-3-319-50142-0).



P. Periyat, B. Naufal and **S. G. Ullattil**, A Review on High Temperature Stable Anatase TiO<sub>2</sub> Photocatalysts, *Photocatalytic Materials & Surfaces for Environmental Cleanup IV*, *Mater. Res. Forum*, 2016, 855, 78 (ISBN: 978-3-03785-349-8).

*Book Chapter (Accepted)*



**S. G. Ullattil**, S. B. Narendranath and P. Periyat, Black TiO<sub>2</sub>: A New Generation Photocatalyst, *Visible Light Active Photocatalysis: Nanostructured Catalyst Design, Mechanisms and Applications*, 2017, Chapter 5 (ISBN: 978-3-527-34293-8).

*Conference Proceedings*

1. **S. G. Ullattil** and P. Periyat, An Ecofriendly Synthesis of High Temperature Thermally Stable Wurtzite ZnO Photocatalysts (International Conference on Emerging Functional Materials (ICEFM-2014) at PSGR Krishnammal College for Women, Coimbatore, Tamil Nadu, India).
2. **S. G. Ullattil** and P. Periyat, Ti<sup>3+</sup> Enriched Defective Black Anatase Titania- a Sol-hydrothermal Strategy toward Sunlight Harvesting Nanocrystals, 28<sup>th</sup> Kerala Science Congress-2015, Kerala, India
3. **S. G. Ullattil** and P. Periyat, High Phase Purity of Anatase TiO<sub>2</sub> by Manganese Doping through a Rapid Microwave Assisted Strategy, National Seminar on New Materials in Chemistry (NMCHEM-2014) organized by University of Calicut in collaboration with University Grants Commission (UGC-India).
4. **S. G. Ullattil** and P. Periyat, Dye Sensitized Solar Cell Fabrication using Nanocrystalline ZnO Photoanode, National Seminar on Advanced Materials in Chemistry (AMCHEM-2014) organized by

University of Calicut, in collaboration with University Grants Commission (UGC-India).

***Journal Articles (Communicated)***

1. **S. G. Ullattil**, T. V. Aiswarya, S. Narayanan, K. Jithesh, K. V. Baiju and P. Periyat, A Sol-solvothermal Processed ‘Black TiO<sub>2</sub>’ as Photoanode Material in Dye Sensitized Solar Cells, *Sol. Energy*.
2. **S. G. Ullattil** and P. Periyat, Synthesis, Properties and Applications of Black TiO<sub>2</sub> Nanomaterials, *Prog. Mater. Sci.*

***Journal Articles (Under Preparation)***

1. **S. G. Ullattil** and P. Periyat, Mn(II) Assisted Pathway towards Black ZnO with Unrivalled Absorption.
2. **S. G. Ullattil** and P. Periyat, A Facile Route to Black CeO<sub>2</sub>.
3. **S. G. Ullattil** and P. Periyat, Heavily Loaded AgNO<sub>3</sub> as “Structural Sharpener”: Shuttling electron density for higher wavelength absorbing ZnO.
4. **S. G. Ullattil** and P. Periyat, A One Pot, Solvent Driven TiO<sub>2</sub> Nanocrystals: Optimizing the Sunlight Harvesting Photoactive Platforms at the Anatase-Rutile Interface.